UNIVERSITÀ DEGLI STUDI DELLA CALABRIA

Facoltà di Scienze MM. FF. NN.

Dottorato di Ricerca in Fisica

XXI Ciclo

Settore scientifico-disciplinare: FIS/05

Tesi di Dottorato

Complex Phenomena in Astrophysical Plasmas

Candidata:

Silvia Perri

Supervisore:
Prof. Vincenzo Carbone

Coordinatore:
Prof. Giovanni Falcone

2005—2008

A mio fratello e ad Emilio

"Et quondam docui, cunctarum exordia rerum
qualia sint et quam variis distantia formis
sponte sua volitent aeterno percita motu
quove modo possint res ex his quaeque creari,
hasce secundum res animi natura videtur
atque animae claranda meis iam versibus esse
et metus ille foras praeceps Acheruntis agendus,
funditus humanam qui vitam turbat ab imo
omnia suffundens mortis nigore neque ullam
esse voluptatem liquidam puramque relinquit.[...]
Hunc igitur terrorem animi tenebrasque necessest
non radii solis neque lucida tela diei
discutiant, sed naturae species ratioque."

**Tito Lucrezio Caro, *De rerum natura*, III: come liberarsi dalla
paura della morte**

Contents

CONTENTS

Chapter 1

Introduction

Complex systems are characterized by a continuously evolving dynamics, whose final state is unpredictable. The degree of complexity depends on the number of elements (parameters) involved, which are often connected via non-linear interactions. The more the number of relationships among the elements, the more complex the system is. Thus, complexity is strongly dependent on the number of parameters necessary for the description of a system; this implies that complexity is not an intrinsic property of a system but is related to its description and depends on the model used. However, simplified models are often adopted. Examples of complex systems are: astrophysical systems, geophysical systems (as for example earthquakes and the dynamics of the atmosphere), economy systems, social systems (communities of interacting people), ecosystems.

In this thesis some aspects of complex phenomena in astrophysical contexts are investigated. In particular, we focus on problems related to the particle acceleration and transport and to the characterization of plasma turbulence in the interplanetary space, both from a theoretical point of view and from data analysis. These phenomena are closely related, indeed, energetic particles, traveling through the interplanetary medium, interact continuously with the plasma present which is in a turbulent state.

The Earth's atmosphere is continuously struck by particles having energies in the range 10^6–10^{22} eV [1]. The energetic flux of these particles, the cosmic rays, is described by a power law, i.e., $dN/dE \sim E^{-\gamma}$, where the index $\gamma \in [2.5, 3.0]$ depends on the energy range. From 10^6 up to 10^{14} eV cosmic rays have solar and Galactic origin, indeed, particles of energies around 1 GeV are accelerated at violent solar events, as flares and coronal mass ejec-
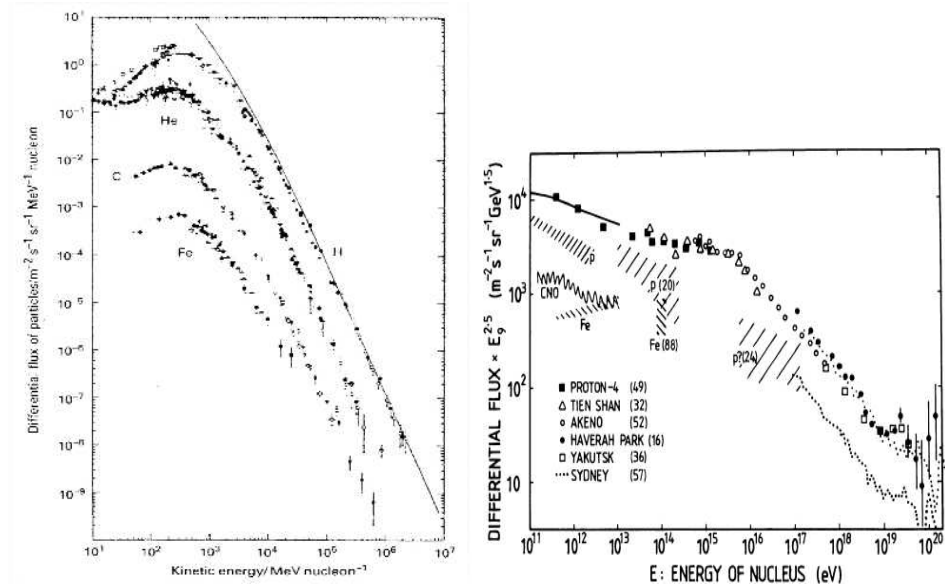
Figure 1.1: Differential energy fluxes of low energy cosmic rays (on the left) and of the high energy cosmic rays (on the right). The latter is normalized to $E_9^{-2.5}$, where E_9 is the energy in units of 10^9 eV. Adapted from Ref.s [1, 2].

tions (CMEs). Above roughly 10^{15} eV the spectrum steepens [2] and the contribution to this energy range comes from cosmic rays having extragalactic origin (for example from particles accelerated at supernova remnants). In Fig. 1.1 the differential fluxes of low energy particles (left panel) and high energy particles (right panel) are displayed. Around 10^{15} eV a knee in the flux can be recognized; owing to a poor statistics (just one particle every 100 years hits one km square of the Earth's surface), the differential flux at very high energies (around 10^{20}) is affected by a large error. As well as cosmic rays, energetic particles are routinely observed in the planetary magnetospheres and close to interplanetary shocks. However, how particles are accelerated in the various physical contexts is a topic poorly understood. Another puzzling topic is the propagation of energetic particles in the interplanetary plasma. Indeed, particles spread out in space interacting with magnetic and electric turbulence present in the medium. Understanding how particles are accelerated and propagate through the heliosphere is relevant in space weather forecasts for assessing arrivals of energetic particle fluxes on

the geospace environment, avoiding damages to spacecraft, astronauts, and electronic systems. One of the aim of this work is to investigate the acceleration processes and the transport properties of charged particles either via theoretical models and with data analysis. Therefore, the first part of this thesis is devoted to investigate these two crucial aspects from a theoretical point of view. We start with a numerical study of transport regimes both in position and velocity spaces, by integrating the equations of motion of charged particles interacting with stochastic electromagnetic fields. We also use the above numerical simulations in order to model protons acceleration processes in the distant Earth's magnetotail. Afterwards, in the framework of stochastic acceleration, we propose another numerical study which reproduces a one dimensional modified Fermi-Ulam model. This has been used for characterizing the formation of particles beams frequently observed in some regions of the Earth's magnetosphere. The results shown seem to be in good agreement with observations. In the second part of this thesis, a diagnostic tool for understanding the transport of energetic particles in the solar wind, based on propagator formalism, has been applied to the analysis of temporal profiles of energetic particles coming from interplanetary shocks.

As said before, cosmic rays propagate in the interplanetary space interacting with the solar wind, a continuous magnetized flow of charged particles (plasma) coming from the Sun and expanding into the whole heliosphere. Thanks to spacecraft *in situ* observations, it has been possible to realize that solar wind is in a state of fully developed turbulence [3]. The turbulent character of the solar wind can be recognized in the high amplitude fluctuations of macroscopic quantities, such as solar wind velocity, magnetic field, density, and temperature. In Fig. 1.2 the temporal evolutions of speed, density, temperature and magnetic field of a fast solar wind stream ($V \sim 700$ km/s) measured by Helios 2, are displayed [4]. Turbulent flows are extremely sensitive to triggering disturbances, indeed, the details of the temporal behavior are very different by changing initial conditions just of a very small quantity, even if the global stochastic character remains roughly unchanged. In other words, average values are not sensitive to small initial fluctuations. Therefore, a probabilistic approach is appropriate in turbulence dynamics.

Turbulence in the solar wind has been studied in analogy with the turbulence in ordinary fluids [5]; indeed, by looking at the power spectra of magnetic and velocity field fluctuations at intermediate scales [3], that is in the range 10^{-3}–10^{-1} Hz, the well know, universal, Kolmogorov law $f^{-5/3}$ is recovered [6], as in non-magnetized fluids. This means that, because turbu-
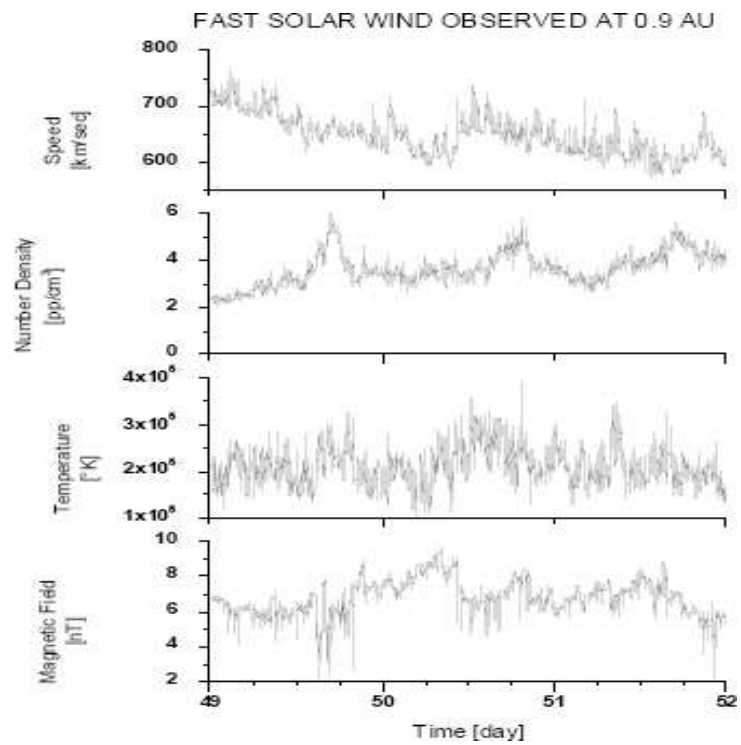
Figure 1.2: From top to bottom: temporal evolution of velocity, density, temperature and magnetic field of a fast solar wind stream detected at 0.9 AU by the Helios 2 spacecraft. Adapted by Ref. [4].

lence involves the formation of several structures (eddies) at all scales, the energy of the flow contained at the largest scales cascades toward smaller and smaller scales as a power law with a characteristic scale index. In ordinary fluids the energy transfer goes on until structures are dissipated by effects of fluid viscosity (*dissipation range*). This small-scale part of the spectrum is described by an exponential function [5]. While in non-magnetized fluids it is clear that energy dissipation takes place at small-scales, a much more puzzling situation is observed in the solar wind. The solar wind turbulent spectrum follows a Kolmogorov law in the intermediate frequency range, named *inertial range*, but above the ion-cyclotron frequency, $f_{ci} = eB/(2\pi m_i)$ with B the magnetic field and m_i the mass of ions, which is a characteristic scale in magnetized plasmas, the spectrum becomes steeper, forming a power law f^{-s}, with $s \in [2, 4]$ [7]. An open question is whether this high frequency range can be associated to a dissipation process, as in ordinary fluids, or to a high frequency mechanism of energy transfer. On the other hand, in the solar wind effects of dissipation via collisions are negligible, because the particle mean free path is roughly equal to the Sun-Earth distance; further, at variance with non-magnetized fluids, the high frequency range is a power law and the fourth-order moment (flatness) of the distributions of magnetic field fluctuations increases toward smaller scales (*intermittency*), leading to a strong non-Gaussianity in the high frequency range. The presence of a high level of intermittency, which is a property of the low frequency range, might be an indication that a high frequency turbulent cascade is going on. Problems related to the knowledge of physical processes involved at small-scales are also due to the fact that high resolution data from spacecraft have been available just recently. In this work, we also try to understand small-scales properties of turbulence by starting from a basic statistical analysis. In the last part of this thesis, we study the character of anisotropy, induced by the presence of a mean interplanetary magnetic field which selects a preferential direction, not only in the solar wind, but also in other two regions of the heliospheric environment, the Earth's foreshock and the Earth's magnetosheath. These are regions forming at 1 AU when the solar wind flow encounters the Earth's magnetosphere (see Chapter 4 for further details). Datasets used allow to perform analysis at frequencies much higher than the ion-cyclotron frequency, which is considered as a reference scale in this work. We highlight that above the ion-cyclotron frequency, the trace of the one-point cross correlation matrix, $S_{i,j} = \langle B_i B_j \rangle - \langle B_i \rangle \langle B_j \rangle$ (involving the magnetic field components), which is related to the magnetic field power spectrum, can-

not be defined unambiguously. Indeed, the eigenvalues of the matrix, giving the degree of anisotropy present in the medium, exhibit a broad power law distributions at those frequencies in all three regions. In addition, while in the low frequency range magnetic field fluctuations are much more concentrated in a plane perpendicular to the mean magnetic field direction, above the ion-cyclotron frequency the situation drastically changes, indeed, fluctuations become less transverse to the large-scale magnetic field. This could be an indication of a change in the nature of magnetic field fluctuations, which pass from being transversely propagating Alfvèn waves to compressive ones. This change should be taken into account when studying high frequency turbulence, either in space and in laboratory plasmas.

Chapter 2

Numerical models for stochastic acceleration

2.1 Acceleration of particles and transport

The problem of particle acceleration is one of the most challenging problems both in astrophysics and in laboratory plasmas. In 1949 E. Fermi [8] proposed a simple acceleration model for relativistic cosmic rays, in order to explain the power-law energy spectrum observed. In this context, particles can be accelerated through stochastic encounters with magnetized clouds present in the interstellar medium, having either a probability of gaining energy (head-on collisions) and a probability of loosing energy (tail-on collisions), depending on the relative sign between particle and cloud velocities. The variation of particle energy at each collision depends on the square of cloud's velocity (second-order Fermi acceleration), $\Delta E/E \simeq (V/c)^2$, being V the speed of the cloud and c the speed of light [9]. However, this mechanism cannot explain values of energy greater than those observed at frequency above 10^{15} eV (above the "knee" of the spectrum). In order to reproduce the high-energy part of the spectrum, an acceleration mechanism, involving the interaction between particles and shock waves, was considered. Depending on their energies (and consequently on their Larmor radii), particles can be reflected from the shock front, owing to an increase in the magnetic field strength, returning in the non-shocked upstream region. If another change in the magnetic field is encountered in the upstream region, particles can return to the shock front and here be accelerated again. In this process the
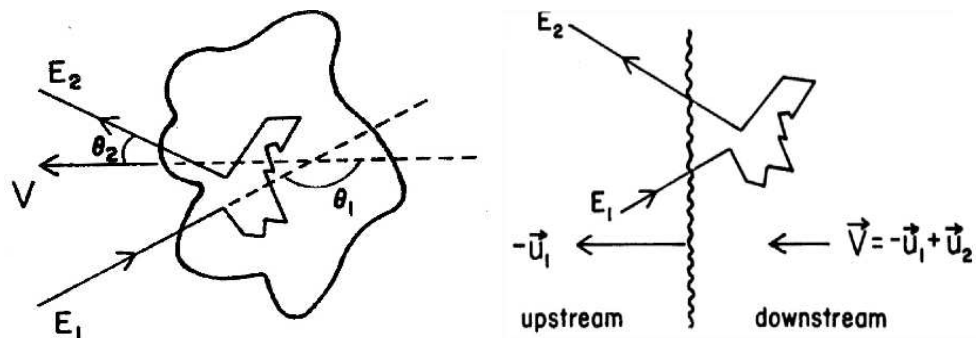
Figure 2.1: Cartoons of the second order Fermi acceleration (on the left) and of the first order Fermi acceleration (on the right). Adapted from *Geisser, 1990.*

variation of particle energy at each reflection is related to the velocity of the shock front, i.e., $\Delta E/E \simeq V/c$ (first-order Fermi acceleration) [9]. A cartoon of these two acceleration mechanisms is displayed in Fig. 2.1.

In the last century, this mechanism has been extensively applied in various astrophysical contexts: shocks from supernova explosions can account for the acceleration of galactic cosmic rays [10], solar flares, coronal mass ejection driven shocks (CMEs) and corotating interaction region shocks (CIRs) can be considered a source of energetic particles. In 1982, Lee and Fisk [11] modified the first-order Fermi acceleration mechanism by considering that magnetic irregularities present in the plasma close to the shock can scatter energetic particles back and forth through the shock front, allowing them to reach high energy values. Magnetic irregularities can be generated or amplified by the shock, or produced by some kind of instability due to the presence of accelerated particles themselves [12]. In this framework the motion of particles is a random walk in space and the number of shock encounters can be very large. This theoretical model, called diffusive shock acceleration (DSA), is largely used in cosmic rays acceleration at extragalactic, galactic and interplanetary shock waves. In order to reproduce different observational features, up to now several mechanisms for particle acceleration have been proposed, ranging from magnetic reconnection [13, 14] and turbulent dissipation [7, 15] to surfing acceleration [16, 17] for solar energetic particles and cosmic rays [18].

Fluxes of energetic particles reach continuously the Earth, then under-

standing transport of particles in the interplanetary space is fundamental
for space weather forecasts. Indeed, energetic particles can be used as a
proxy for the arrival of strong solar disturbances on the geospace environ-
ment. The problem of particle transport has a crucial role also in controlled
fusion plasmas, because the knowledge of the transport scaling is important
in the design of fusion reactors [19]. The propagation of charged particles
in plasmas is strongly influenced by the presence of electric and magnetic
turbulence, which causes pitch angle scattering and perpendicular transport
[20, 21]. The standard scenario of normal transport (Brownian-like motion)
in position space has been considered for long time: from a dynamical point
of view, normal diffusion is an uncorrelated, Markovian (without memory)
process. On the other hand, from a probabilistic point of view this process
can be described by the probability $P(x,t)$ of finding a walker at position
x at time t. $x = \sum_i x_i$ and $t = \sum_i t_i$ are the sum over the random dis-
placements x_i performed at times t_i. Displacements are uncorrelated and
after a large number of jumps (i.e., for long times) $P(x,t)$ tends to a Gaus-
sian distribution with finite second order moment. This is a consequence of
the Central Limit Theorem, which assures Gaussian distribution and, conse-
quently, a mean square displacement growing linearly in time, $\langle x^2(t) \rangle \simeq t$, in
the limit of a large number of independent jumps [22]. The Gaussian distribu-
tion, $P(x,t)$, is solution for the diffusive equation $\partial/\partial t P(x,t) = D\nabla^2 P(x,t)$,
where D is the diffusion coefficient having dimension $[L^2/T]$. However, recent
fluid and plasma experiments [23, 24], and numerical simulations [25, 26, 27]
have highlighted the presence of transport regimes both slower (subdiffusion)
and faster (superdiffusion) than the normal diffusion. These regimes, called
anomalous, imply the breaking of the Central Limit Theorem, indeed, they
are characterized by a non-Gaussian distribution for the probability of jump
lengths and by the presence of long-range correlations [28, 29]. Subdiffusion
is associated to trapping events described by a waiting-time distribution $\psi(\tau)$
between jumps, which are not separated by regular time intervals as in the
normal diffusive regime; the probability density function for waiting times is
a power-law [19], $\psi(\tau) \simeq \tau^{-(\beta+1)}$, indicating that a particle can spend a long
time in a trap before performing a jump. In such a regime the mean square
displacement grows less than linearly in time, A superdiffusive regime arises
when the diffusion coefficient diverges; this can due either to a divergence of
the velocity variance (*Lévy flights*, or to the presence of strong correlations
decaying as a power-law in time (*Lévy walks*) [30]. In this case we have a
multi-step memory process and the mean square displacement is faster than

linearly in time. In anomalous diffusion regimes the probability $P(x,t)$ follows a generalized diffusion equation [31, 32], $\partial^\alpha / \partial t^\alpha P(x,t) = D_\alpha \nabla^2 P(x,t)$, where $\partial^\alpha / \partial t^\alpha$ represents the Riemann-Liouville fractional derivative and D_α is the fractional diffusion coefficient with dimension $[L^2/T^\alpha]$.

The Fermi acceleration model is an example of diffusion also in the velocity space (non-stationary process). The interesting point is to investigate the relationship between dynamics in position and in velocity spaces [33, 34, 35, 36]. This relation is strongly dependent on the correlations introduced in the models, indeed, different models can be characterized by different scaling properties in position and in velocity spaces.

In this Chapter two theoretical models have been developed in order to investigate the dynamics of non-relativistic test particles interacting with magnetized clouds in 1D and 2D geometries. Some results are compared with observations of accelerated particles coming from various physical contexts and also a theoretical study on particle diffusion has been performed.

2.2 Dynamics of test particles in stochastic electromagnetic fields

In this study the diffusive dynamics of non-relativistic test particles, subjected to a stochastic electromagnetic field, is investigated. The motion of each particle is described by the usual equations of motion, that are

$$\frac{d\boldsymbol{r}}{dt} = \boldsymbol{v}\,, \tag{2.1}$$

$$\frac{d\boldsymbol{v}}{dt} = \frac{q}{mc}\left[\boldsymbol{E}(\boldsymbol{r},t) + \boldsymbol{v} \times \boldsymbol{B}(\boldsymbol{r},t)\right]\,. \tag{2.2}$$

A simple synthetic model for the electromagnetic fluctuations can be obtained by using a vector potential $\boldsymbol{A}$ lying on the (x,y)-plane, namely $\boldsymbol{A} = (A_x(\boldsymbol{r},t), A_y(\boldsymbol{r},t), 0)$. In the gauge where the scalar potential is zero, the electric field is given by $\boldsymbol{E} = (E_x, E_y, 0) = -\partial \boldsymbol{A}/\partial t$, while the magnetic field lies in the direction perpendicular to the (x,y) plane, namely $\boldsymbol{B} = (0, 0, B) = \nabla \times \boldsymbol{A}$. With these assumptions the particle dynamics becomes bidimensional because the z-component of the Lorentz force is zero. Electromagnetic fluctuations are computed via a superposition of electric and magnetic fields generated by random positioned magnetized "clouds" moving in time according to prescribed laws in the (x,y)-plane. At variance

with the model proposed by Fermi [8], here charged particles do not undergo collisions with the clouds, but a Lorentz force, due to the presence of the electromagnetic fields, continuously acts on test particles. The basic simulation box is a square of size $L \times L$ containing N clouds and repeated in space in order to allow a long time diffusive analysis (see below). Therefore the vector potential is given by

$$A_x = A_y = A_0 \sum_{n=1}^{N} \left[\psi_n(\xi) + \sum_{m} \psi(\tilde{\xi}_m) \right] , \qquad (2.3)$$

where $\psi = e^{-\xi_n}$, $\xi_n = |\boldsymbol{r} - \boldsymbol{r}_n(t)|/R$, $\boldsymbol{r}_n(t) = (x_n(t), y_n(t))$ are the coordinates of the n-th cloud, R represents the typical spatial extension of the potential produced by a single cloud, and $\tilde{\xi}_m = |\boldsymbol{r} - \tilde{\boldsymbol{r}}_m(t)|/R$, being $\tilde{\boldsymbol{r}}_m$ the coordinates of the clouds in the replicated neighbour boxes of the basic cell. According to the hypothesis that the other cells are duplicates of the basic cell, we have that $\tilde{\boldsymbol{r}}_m = \boldsymbol{r}_n + (iL, jL)$, with i and j integer numbers and at least one of them is non-zero. Moreover, in order to simplify the sum in Eq. (2.3), R and N have been chosen in such a way that R is smaller than the distance between nearby clouds, therefore in the summation $\sum_n$ of Eq. (2.3) it is sufficient to consider only the eight nearest boxes to the basic cell, that is, $(i, j) = (\pm 1, 0), (0, \pm 1), (\pm 1, \pm 1), (\mp 1, \pm 1)$. Since we are interested in investigating the diffusive properties of the model and not to reproduce detailed properties of cosmic rays, at variance with the model by Fermi [8], where clouds are allowed to move with a given bulk speed, here the motion of the clouds is sinusoidal along both x and y. That is, the coordinates of the n-th cloud $x_n(t)$ and $y_n(t)$ are given by

$$\begin{aligned} x_n(t) &= x_{n0} + a_n \cos[\omega_n t + \alpha_n] \\ y_n(t) &= y_{n0} + b_n \sin[\omega_n t + \beta_n] , \end{aligned} \qquad (2.4)$$

where x_{n0} and y_{n0} are the initial random coordinates of the n-th cloud, a_n and b_n are the amplitudes of the oscillations of the n-th cloud along x and y respectively, ω_n is the oscillation frequency, and α_n and β_n are the initial oscillation phases, randomly chosen within the interval $[0, 2\pi]$. For the sake of simplicity, we used the same values of motion amplitudes and frequencies for all clouds, namely $a_n = b_n = a$ and $\omega_n = \omega$.

The motion equations have been adimensionalized by using the following normalization factors: $B_0 = A_0/L$ for magnetic fields, $\omega_0 = (qB_0)/m$ for

frequencies, $t_0 = 2\pi/\omega_0$ for times, $v_0 = L\omega_0$ for velocities and $E_0 = A_0\omega_0$ for electric fields respectively. Finally, Eq. (2.2) can be rewritten as

$$\frac{d\boldsymbol{v}}{dt} = \boldsymbol{E}(\boldsymbol{r},t) + \boldsymbol{v} \times \boldsymbol{B}(\boldsymbol{r},t) ,\qquad(2.5)$$

where

$$B(\boldsymbol{r},t) = \sum_n \frac{1}{R}\frac{\partial\psi}{\partial\xi_n}\left\{\frac{[x - x_n(t)] - [y - y_n(t)]}{|\boldsymbol{r} - \boldsymbol{r}_n(t)|}\right\} + N.T. ,\qquad(2.6)$$

$$E_i(\boldsymbol{r},t) = \sum_n \frac{1}{R}\frac{\partial\psi}{\partial\xi_n}\left\{\frac{[x - x_n(t)]\dot{x}_n(t) + [y - y_n(t)]\dot{y}_n(t)}{|\boldsymbol{r} - \boldsymbol{r}_n(t)|}\right\}\boldsymbol{e}_i + N.T. .\quad(2.7)$$

$\boldsymbol{e}_i$ is the unit vector along the i-th direction on the plane, and N.T. stands for the similar terms given by the clouds in the nearest cells. In Fig. 2.2 a configuration of the synthetic fluctuations in the basic cell is displayed.

In the stationary case ($\omega = 0$) the model becomes an electromagnetic reformulation of the Lorentz model [37], which describes the motion of electrons (treated as material points) in metals via kinetic equations, with the sole difference that here the potential is smooth. When $\omega \neq 0$ the model can be considered Lorentz-like, owing to a time dependence of the cloud positions.

2.2.1   Analysis of diffusion

Test particles simulations are performed by solving the equations of motion via a 4th order Runge-Kutta scheme. $n_{part} = 6 \times 10^3$ particles are injected at random positions within the basic cell with velocities extracted from a 2D Maxwellian distribution, i.e., $P(v_x, v_y) \propto \exp[-(v_x^2 + v_y^2)/2v_{th}^2]$, being $v_{th} = 3 \times 10^{-2}$ the thermal velocity. The results shown below come from numerical simulations in which the parameters of the system are fixed to $N = 50$, $a = 10^{-3}$ and $R = 7 \times 10^{-2}$; the statistical analysis is performed firstly by varying the oscillation frequency of the clouds motion, in particular three different values are used, namely $\omega = 10^{-2}$, $\omega = 1$ and $\omega = 10$. In Fig. 2.3 two examples of particle trajectories, for $\omega = 10^{-2}$ (left panel) and $\omega = 10$ (right panel) respectively, are displayed. At a glance it is possible to notice that walks performed by particles in the two cases are completely different, indeed, when the oscillation frequency assumes a small value, a gyration motion is distinguishable in the trajectory and the particle spreading
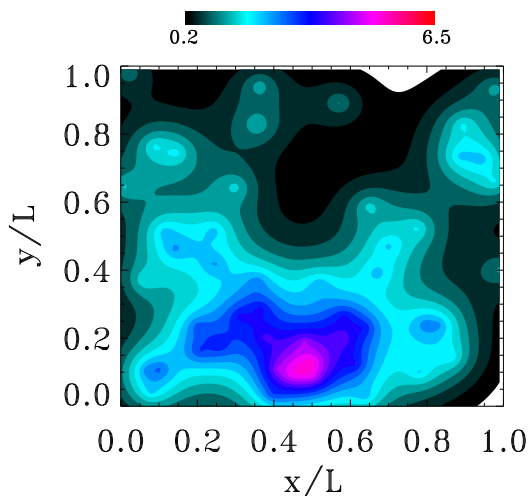
Figure 2.2: Contour levels of the module of the vector potential,$|\boldsymbol{A}|$, in the basic cell of length $L = 1$. $N = 50$ random positioned clouds oscillate at frequency $\omega = 1$ with amplitude $a = 0.001$.

is reduced; on the other hand, by increasing ω, the gyration is lost and particle tends to "visit" a higher number of cells in space [36].

In order to study the diffusive properties of the system in both position and velocity spaces, the mean square position and velocity displacements are computed as functions of time, that is, $\langle[\boldsymbol{r}(t) - \boldsymbol{r}_0]^2\rangle$ and $\langle[\boldsymbol{v}(t) - \boldsymbol{v}_0]^2\rangle$, where brackets represent averages over the particle population. In the case of normal diffusion particles make a Brownian-like motion, with a mean square position displacement growing linearly in time, $\langle[\boldsymbol{r}(t) - \boldsymbol{r}_0]^2\rangle \sim t$. On the other hand, if a power law dependence of the mean square position displacement on time is found for long times

$$\langle[\boldsymbol{r}(t) - \boldsymbol{r}_0]^2\rangle \sim t^{2\nu_x} , \qquad (2.8)$$

with $\nu_x \neq 1/2$, the diffusion is anomalous. The cases $\nu_x > 1/2$ and $\nu_x < 1/2$ are called superdiffusion and subdiffusion respectively. Diffusion in the velocity space can be studied by conjecturing a scaling for the mean square velocity displacements in analogy with Eq. (2.8), that is,

$$\langle[\boldsymbol{v}(t) - \boldsymbol{v}_0]^2\rangle \sim t^{2\nu_v} . \qquad (2.9)$$
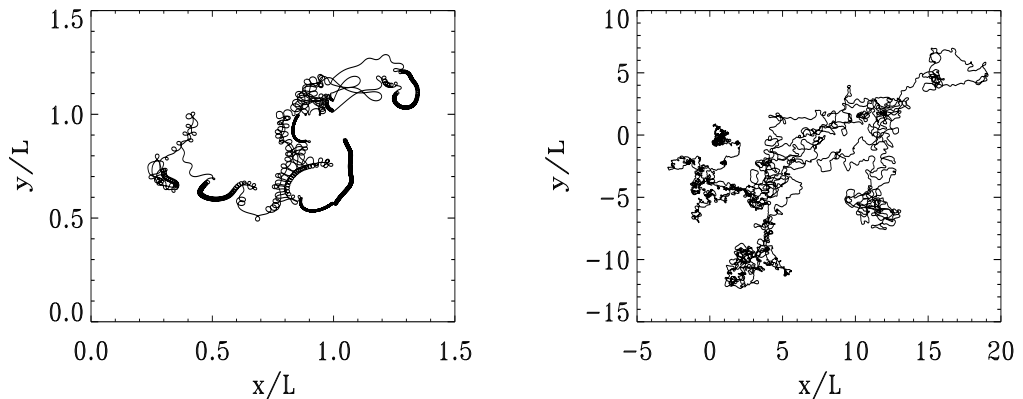
Figure 2.3: Examples of particle trajectories for $\omega = 10^{-2}$ (left panel) and $\omega = 10$ (right panel).

Table 2.1: Power law exponents ν_x and ν_v obtained from best fits of position and velocity mean square displacements, respectively.

	$\omega = 0.01$	$\omega = 1$	$\omega = 10$
ν_x	0.49	0.89	1.19
ν_v	4.7×10^{-4}	0.42	0.39

The mean square displacements of position and velocity are shown in Fig. 2.4 for the three values of ω used and for $t = 10^4$ Larmor times [36]. Power-law best fits are also displayed as solid lines. The values of the exponents ν_x and ν_v, calculated from the fit, are reported in Table 2.1. For $\omega = 10^{-2}$ the diffusion is nearly normal, indeed $\nu_x \simeq 0.5$ and the velocity mean square displacement remains constant after an initial transient. When the oscillation frequency is increased, i.e., for $\omega = 1$ and for $\omega = 10$, the system passes from a standard diffusive regime to a superdiffusive regime, characterized by the presence of long jumps. In the velocity space a power-law temporal profile for the mean square displacement is observed. As a consequence of the time correlations, the relationship between the scaling exponents ν_x and ν_v is not
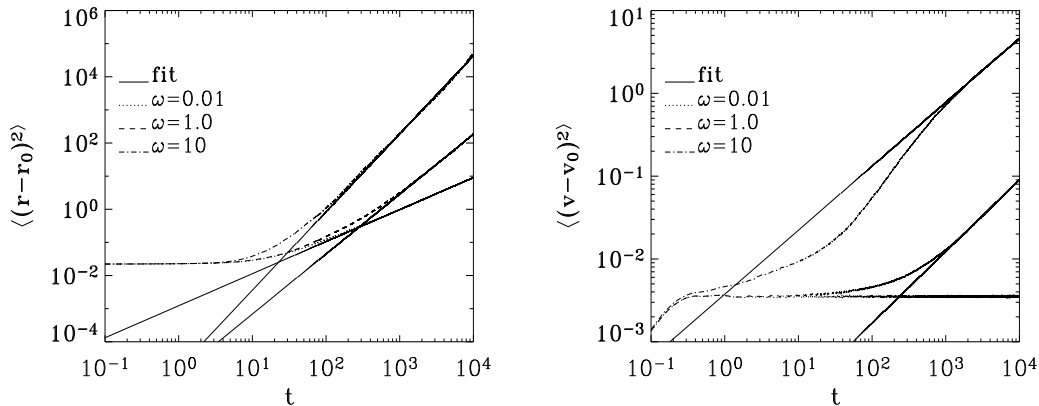
Figure 2.4: Position mean square displacement (left panel) and velocity mean square displacement (right panel) for $\omega = 10^{-2}$ (dotted lines), $\omega = 1$ (dashed lines), and $\omega = 10$ (dashed-dotted lines) in log-log scale. Solid lines represent power-law best fits.

simple [33, 35]. Indeed, a straightforward calculation shows that

$$\langle [\boldsymbol{r}(t) - \boldsymbol{r}_0]^2 \rangle \simeq 2 \int_0^t \int_0^{t-t'} \langle |\boldsymbol{v}(t')|^2 \rangle C(t', \tau) dt' d\tau, \qquad (2.10)$$

where $C(t', \tau) = \langle \boldsymbol{v}(t')\boldsymbol{v}(t'+\tau) \rangle / \langle |\boldsymbol{v}(t')|^2 \rangle$. In the case of a standard diffusive regime, where acceleration processes are absent, $\langle |\boldsymbol{v}(t')|^2 \rangle$ is constant, $C(t', \tau)$ is independent of t', and $\langle [\boldsymbol{r}(t) - \boldsymbol{r}_0]^2 \rangle$ is just proportional to t, by integrating over t', and to the diffusion coefficient, that is, $D \propto \int_0^{t-t'} \langle \boldsymbol{v}(0)\boldsymbol{v}(\tau) \rangle d\tau$. On the other hand, in non-stationary cases, the presence of $C(t', \tau)$ makes the scaling exponents ν_x and ν_v not related in a simple way. Indeed, the integration over t' in Eq. (2.10) depends on the velocity correlations of the system, i.e., on $C(t', \tau)$. In such a case, only the upper bound $\nu_x \leq \nu_v + 1$ can be derived [33]. When the electric field is strong, that is, when very strong correlations of velocities are present, the equality $\nu_x = \nu_v + 1$ (the maximum allowed difference between the scaling exponents) seems to occur [33, 35]. This indicates that a precise relationship between ν_x and ν_v is strongly dependent on the correlations introduced in the model, therefore, different models imply different scaling properties.

A parametric study of the model by fixing the oscillation frequency and by varying the typical extension of the clouds R is also performed [38]. An
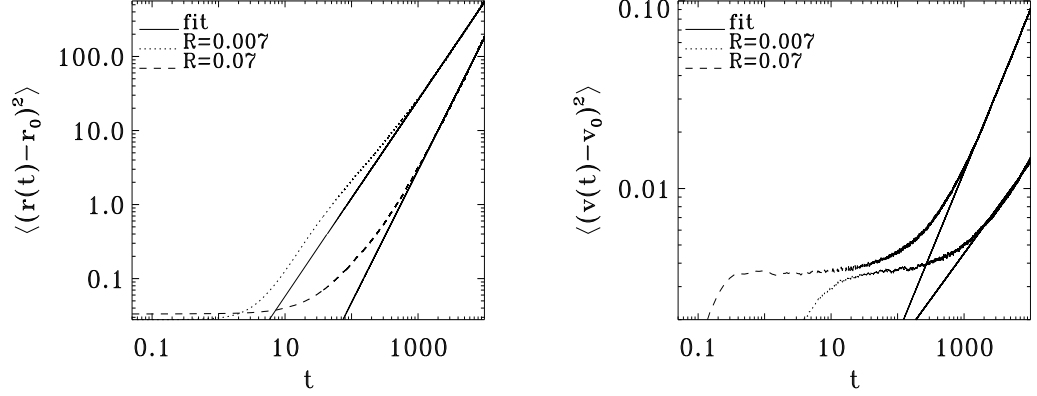
Figure 2.5: Position mean square displacement (left panel) and velocity mean square displacement (right panel) for $R = 7 \times 10^{-3}$ (dotted lines), and $R = 7 \times 10^{-2}$ (dashed lines) in log-log scale. Solid lines represent power-law best fits. The value of the oscillation frequency is fixed to $\omega = 1$.

example is displayed in Fig. 2.5 where the same plots as those in Fig. 2.4 are shown but for two different values of R, namely $R = 7 \times 10^{-3}$ and $R = 7 \times 10^{-2}$, and for $\omega = 1$. Best power-law fits highlight that a variation in the values of the scaling exponents ν_x and ν_v is noticeable but no variations in the properties of diffusion give rise. Indeed, from the scaling exponent values reported in Table 2.2, it can be observed that the system persists in the superdiffusive regime in all two cases, indicating a weak sensitive of the model to variations of R.

Table 2.2: Power law exponents ν_x and ν_v obtained from best fits of position and velocity mean square displacements when the typical size of the clouds is changed.

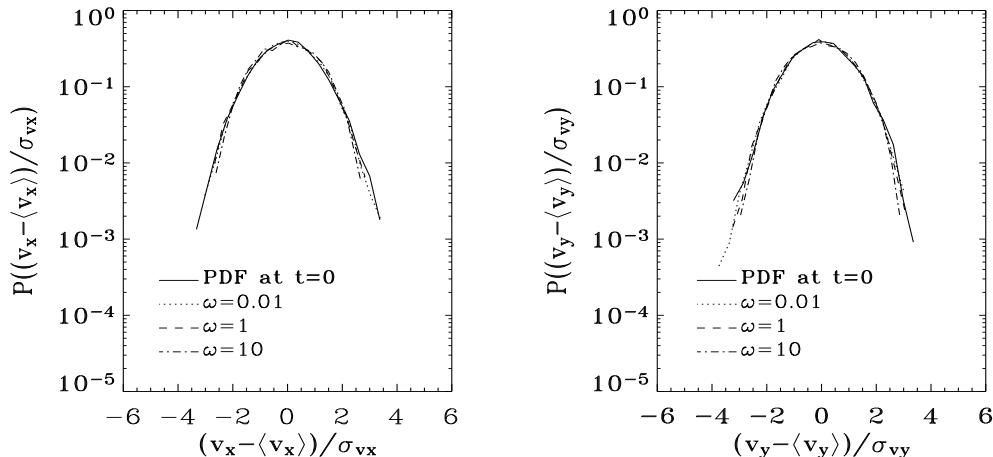|	$R = 7 \times 10^{-3}$	$R = 7 \times 10^{-2}$
ν_x	0.67	0.89
ν_v	0.25	0.44

Figure 2.6: PDFs of the standardized velocity components at $\omega = 10^{-2}$ (dotted lines), $\omega = 1$ (dashed lines), and $\omega = 10$ (dashed-dotted lines), collected at the end of the numerical simulations in log-lin scale. The PDFs at $t = 0$ are displayed as solid lines for comparison.

2.2.2 Analysis of Probability Density Functions

The probability density functions (PDFs) of the two velocity components in the (x, y)-plane at different ω, collected at the end of the numerical simulations, are shown in Fig. 2.6 together with the PDFs of the initial velocities (at $t = 0$), which are Gaussian. In order to make a comparison among PDFs, the distributions of the standardized variables, $(v_i - \langle v_i \rangle)/\sigma_{v_i}$, are computed (these variables have zero mean and unitary standard deviation). The shape of the PDFs displayed in Fig. 2.6 does not change significantly with respect to the initial Gaussian distribution. However, the standard deviations of v_x and v_y increase as the oscillation frequency increases (see Table 2.3), that is the velocity distributions become broader in the presence of superdiffusion in the position space.

The strong energization is clearly visible by looking at the PDFs of the particle energies. Thus, in Fig. 2.7 the PDFs of the energy at different ω are plotted. By increasing the oscillation frequency of the clouds, particles can gain a large amount of energy owing to the strong interaction with the electromagnetic fields; when ω is below the Larmor frequency the efficiency

Table 2.3: Standard deviations of the two velocity components collected at
the end of the numerical simulations for $\omega = 0.01$, $\omega = 1$, and $\omega = 10$. As a
comparison the standard deviations of the initial velocities are shown in the
first two rows.

		Standard deviation
Initial	v_{x0}	0.03
	v_{y0}	0.03
$\omega = 0.01$	v_x	0.03
	v_y	0.03
$\omega = 1$	v_x	0.21
	v_y	0.21
$\omega = 10$	v_x	1.49
	v_y	1.49

of the Fermi-like mechanism is rather low, indeed no significant deviations
from the initial particle distribution (solid line in Fig. 2.7) are noticeable.
As it has been discussed for velocity distributions, the shape of the PDFs
of energies remains Maxwellian in all three case, i.e., $P(E) \sim K \exp(-\lambda E)$,
where K and λ are constants. Then, in this model the anomalous diffusion
regime is associated to an energization of the bulk of the particle population
and not to the existence of high energy tails in the velocity distributions.

2.2.3 Application to the Earth's Magnetosphere

Using the numerical model described in Sec. 2.2, a test particle simulation
has been performed in order to reproduce the interaction between electromag-
netic fluctuations and charged particles in the distant Earth's magnetotail.
In the magnetospheric environment, a variety of accelerated particle popu-
lations is observed. Many spacecraft have detected energetic particles and
even beams in the geomagnetic tail, with energies in the range of tens of keV
and sometimes up to 100-200 keV [39, 40]. In the near-Earth neutral sheet
($-20\ R_E < X < -10\ R_E$) AMPTE IRM reported observations of several
types of particle distributions functions [41], ranging from isotropic ones to
ring and beam types. Energetic particles are observed as beamlets at the
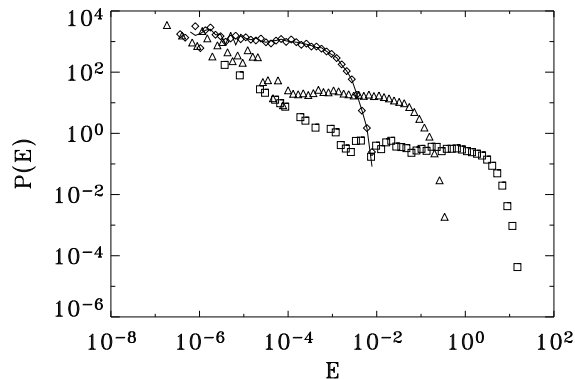lobeward edge of the plasma sheet boundary layer (PSBL) [42, 43]. The

Figure 2.7: PDFs of the energies of particles collected at $t = 10^4$ Larmor times for $\omega = 10^{-2}$ (diamonds), $\omega = 1$ (triangles), and $\omega = 10$ (squares) in log-log scale. The solid line represents the initial Maxwellian distribution.

common idea is that these particles are accelerated in the magnetospheric current sheet, which is a plane separating regions of oppositely directed magnetic field, and extends in the antisolar direction up to more than 200 Earth's radii (see Fig. 2.8). However, the acceleration mechanisms are poorly understood. The quasi-stationary dawn-dusk electric field E_y present in the magnetotail can be a source of acceleration for ions performing Speiser-like orbits [44, 45, 42, 43], but realistic values of the large scale electric field ($E_y \simeq 0.1$–0.3 mV/m) lead to maximum potential drops of the order of 30 keV (corresponding to type I beams), while particles exceeding 150 keV (type II beams) are sometimes observed [46, 47]. Besides energy values, these two types of beams exhibit other different characteristics; indeed, type I beams ion velocity distribution functions are highly collimated in energy (see left panel of Fig. 2.9), they are observed during quiet periods in the PSBL, and the beam duration is of the order of 20 minutes; type II beams ion velocity distribution functions are wide in velocities parallel to the PSBL magnetic field, as it is shown in the right panel of Fig. 2.9, they are detected both in quiet and disturbed periods, and their observed duration is of few minutes [47]. In Fig. 2.10 ion beams energy distributions along the y direction in
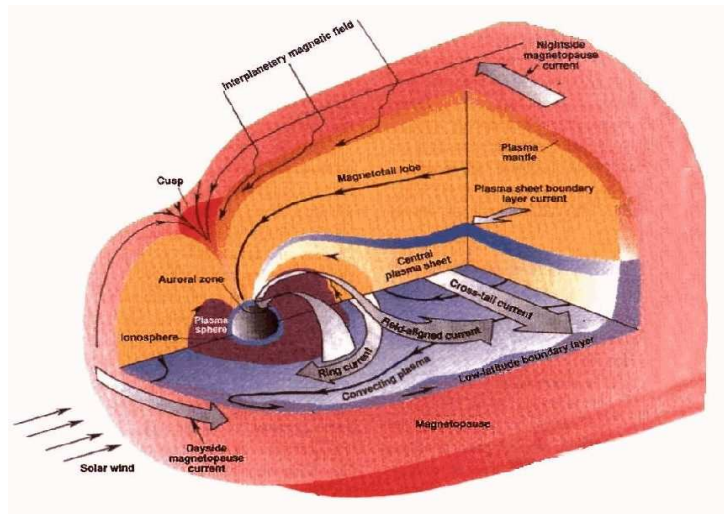
Figure 2.8: Cartoon of the magnetospheric environment.

the GSM reference frame[1] are shown [47], both for type I and for type II beams. If the acceleration mechanism at work in the current sheet is only due to the presence of the dawn-dusk electric field, its value should be of the order of 1 mV/m in order to explain ion energies around 150-200 keV, but this is not consistent with its realistic value. By analyzing the "geography" of the observed ion beams, Ref. [47] has recently shown that, beside E_y, another acceleration mechanism is required for type II beams. Since they are regularly observed, the acceleration mechanism has to be of a quasi-steady nature. One such mechanism can be the evolution of electromagnetic fluctuations in the magnetotail [48]. The high variability of local and boundary conditions in the magnetotail quasi-neutral sheet and the inhomogeneity of the current sheet structure allow for the description of magnetic fluctuations in terms of vortices and of localized moving clouds of plasma and magnetic field [49, 50, 51].

In this work the Fermi-like acceleration, described in Sec. 2.2, due to the presence of moving magnetic structures, which mimic the magnetic fluctu-

---

[1]The Geocentric Solar Magnetospheric (GSM) coordinate system has the X-axis along the Earth-Sun line, the Y-axis is perpendicular to the Earth's magnetic dipole, so that the X-Z plane contains the dipole axis. The positive Z-axis is chosen to be in the same sense of the northern magnetic pole.
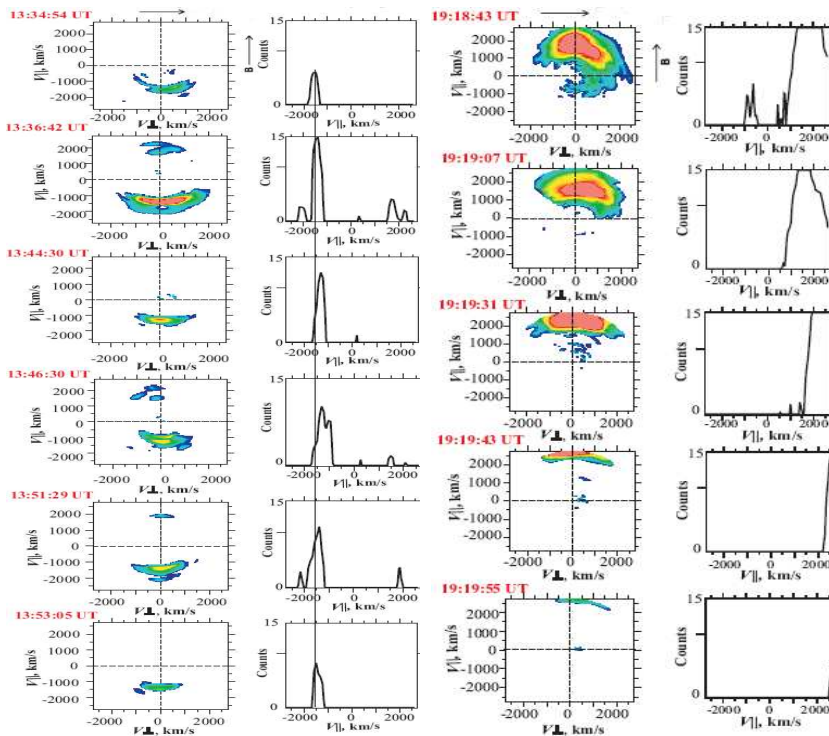
Figure 2.9: Ion velocity distribution functions observed by Geotail on 12 December 1994 during the PSBL crossing at 13:34-13:54 UT (left panel), and at 19:18-19:20 UT (right panel). Adapted from Ref. [47].

ations observed by spacecraft in the distant magnetotail, is proposed as an additional energization mechanism. Ions are assumed to move in the neutral sheet along Speiser orbits, while the motion perpendicular to the plane is neglected. We adopt a 2D model in order to compare the contribution to the acceleration process of the stochastic mechanism and that coming from the dawn-dusk electric field. Both these mechanisms are at work inside the current sheet. By varying the features of electromagnetic fluctuations, we show that the combined effect of E_y and of the moving clouds can explain a range of energetic ion observations, including the typical energies and the typical acceleration times.
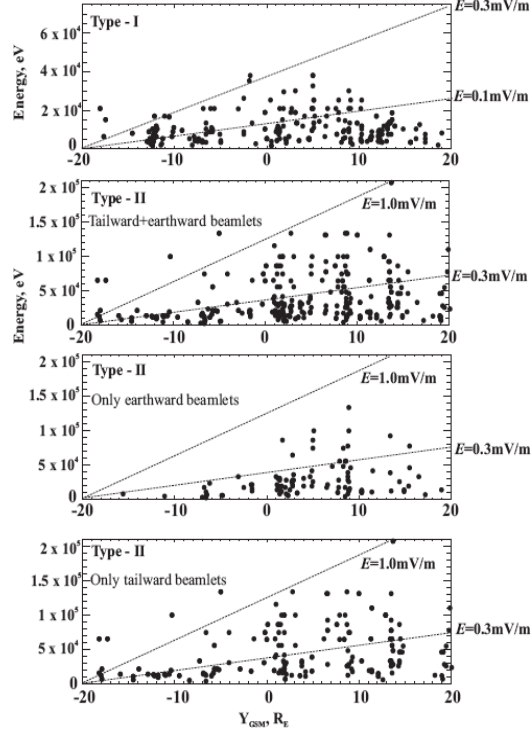
Figure 2.10: Ion beam energy distribution along the y direction in the GSM reference frame. Both type I and type II beams are shown. Dashed lines indicate the limit in ion energy gain if only the direct dawn-dusk electric field acceleration is considered. Adapted from Ref. [47].

The model

In this case, the fields equations, $\mathbf{B} = \nabla \times \mathbf{A}$ and $\mathbf{E} = -\nabla\phi + \partial\mathbf{A}/\partial t$, are solved in the gauge where $-\nabla\phi = E_y\mathbf{e}_y$, being $E_y = $ const. The vector potential is given by Eq. (2.3) but without the term relevant to the replicated neighbour boxes, i.e.,

$$A_x = A_y = A_0 \sum_n \psi(\xi_n), \tag{2.11}$$

where $\psi(\xi_n) = e^{-\xi_n}$ and $\xi_n = |\mathbf{r} - \mathbf{r}_n(t)|/l_{cl}$, with $|\mathbf{r} - \mathbf{r}_n(t)|$ the difference between particle and cloud positions and l_{cl} the typical size of the clouds. The simulation box has a size L corresponding to the width of the magnetotail current sheet and particles are positioned in it with initial energies of the

order of 100 eV. This is a characteristic value for protons coming from the
magnetospheric mantle and reaching the magnetotail. The usual equations
of motion for test particles (see Eq. (2.5)) are integrated until a particle
leaves the simulation box; at this point another one is injected in order to
keep the total number of particles constant. Assuming a typical size for the
simulation box of $L = 10^5$ km and a mean magnetic field $B_0 = 2$ nT, in
agreement with the observations in the distant Earth's neutral sheet [52],
a characteristic proton Larmor frequency $\omega_0 = 0.2 \text{sec}^{-1}$, a normalization
velocity $v_0 = \omega_0 L = 2 \times 10^4$ km/sec and a normalization electric field $E_0 =
B_0 \omega_0 L = 40$ mV/m are obtained. The typical proton gyroperiod is nearly 30
sec. The electromagnetic field equations are:

$$B_z(\boldsymbol{r}, t) = \delta B_z = -\frac{A_0}{l_{cl}} \sum_n \frac{\partial \psi}{\partial \xi_n} \frac{[(x - x_n(t)) - (y - y_n(t))]}{|\boldsymbol{r} - \boldsymbol{r}_n(t)|} \quad (2.12)$$

$$\boldsymbol{E}(\boldsymbol{r}, t) = (\delta E_x, E_y + \delta E_y, 0)$$

where $\delta E_x = \delta E_y = \delta E$ and

$$\delta E = -\frac{A_0}{l_{cl}} \sum_n \frac{\partial \psi}{\partial \xi_n} \frac{[(x - x_n(t))\dot{x}_n(t) + (y - y_n(t))\dot{y}_n(t)]}{|\boldsymbol{r} - \boldsymbol{r}_n(t)|} . \quad (2.13)$$

The equations of motion are integrated for an ensemble of 5000 test parti-
cles having initial random positions and velocities extracted from a 2D Gaus-
sian distribution with $v_{th} = 120$ km/s (considering a proton temperature of
$T_p \simeq 10^6$ K).

Regarding to the system parameters, $N = 100$ clouds are put in the sim-
ulation box. These magnetized clouds mimic the electromagnetic perturba-
tions present in the neutral sheet, then it is reasonable to associate a charac-
teristic velocity corresponding to the Alfvèn wave velocity, i.e., $V_A \simeq 500$
km/sec. In the present simulations we have been varying just one pa-
rameter, that is the cloud size. Three cases are reported here, i.e., $l_{cl} =
0.016L, 0.032L, 0.08L$ corresponding to oscillation frequencies $\omega = V_A/l_{cl}$.
These frequencies fall in the range of those observed by Geotail in the dis-
tant magnetotail [52]. For simplicity, the amplitude a of the oscillation has
the same value as l_{cl}. Finally, the typical value of the dawn-dusk electric
field has been fixed to $E_y = 0.2$ mV/m, in the range of the observed values
[52, 47], while the order of magnitude of the fluctuating electric field is 1
mV/m.

2.2. DYNAMICS OF TEST PARTICLES IN STOCHASTIC ELECTROMAGNETIC FIELDS
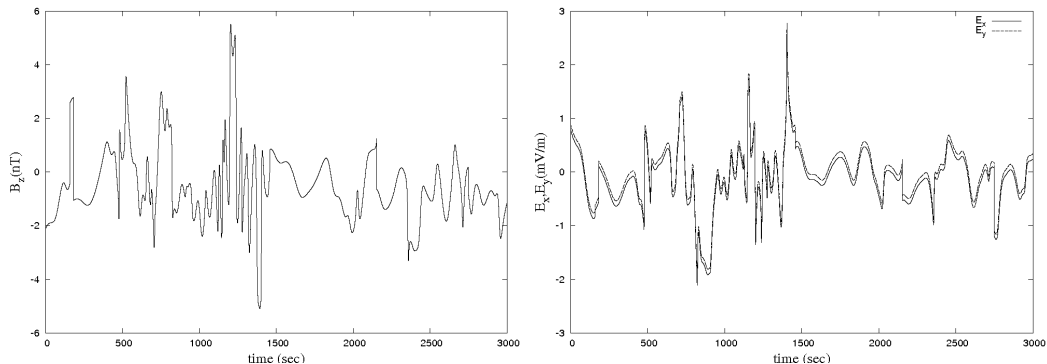

Figure 2.11: Time evolution of the model magnetic field (on the left) and of the electric field components (on the right) at a fixed position in the simulation box.

Numerical results

Fig. 2.11 shows the time behavior of the magnetic field B_z and of the electric field components E_x, E_y obtained from the numerical model for 100 Larmor times at a fixed position, in this case the cloud dimension is $R = l_{cl}/L = 0.08$. Magnetic field evolution displayed in Fig. 2.11 compares rather well with typical structures and irregular oscillations of the normal component of the magnetic field observed, for instance, by Geotail in the distant tail (see Fig. 1 in Ref. [52]).

Several simulations are performed by varying the parameter R, in order to control the competition of the two acceleration mechanisms, the electric field acceleration and the Fermi-like acceleration. In Fig. 2.12 the contour level of magnetic fluctuations B_z (left panel) and five trajectories of charged particles in the simulation box (right panel) are displayed, being the cloud extension fixed to $R = 0.016$. It can be noticed that the influence of the Fermi-like mechanism is weak with respect to the acceleration due to the presence of the constant component of the electric field along the y direction, indeed, particles are mainly accelerated along y, and exit from the simulation box along the direction of E_y. Their trajectories are very smooth and do not exhibit any gyration motion. A different situation is visible in Fig. 2.13 showing the results of a simulation in which clouds have a size $R = 0.08$: here the particle-cloud interaction is increased and the Fermi-like mechanism becomes highly competitive with the steady electric field acceleration. Parti-
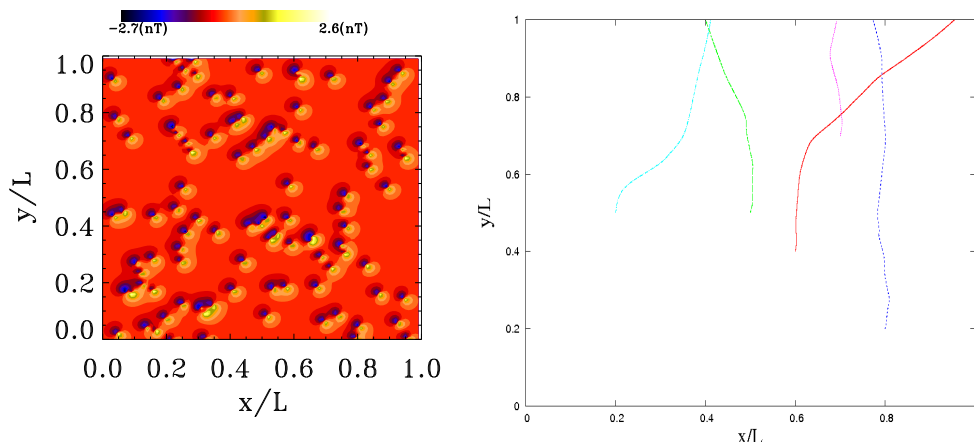
Figure 2.12: Contour level of B_z (left panel) and five trajectories of different charged particles in the basic cell (right panel) coming from a simulation in which $R = 0.016$.

cles remain in the simulation box for a longer time without rapidly escaping along the y direction.

Fig. 2.14 displays the velocity distribution functions in log-lin axes along the y direction at three different times and at the starting time (dotted line), for three different values of the cloud size (R increases from the top to the bottom). In the top panel where $R = 0.016$, it can be seen that particles gain in few minutes a bulk velocity along positive y direction due to the presence of the constant electric field. After that, different transient stages are observed and the system reaches a stationary state after 10-15 minutes. This time corresponds to the typical lifetime of protons into the simulation box. In this state, the shape of the distribution function does not change anymore. When the clouds are small, particles interact weakly with the electromagnetic fluctuations, so that the steady electric field plays the main role in the particle dynamics.

In the middle panel (i.e., $R = 0.032$), it can be seen that the distribution is broader, because the stronger interaction with the electromagnetic clouds provides a randomization of the velocities, and the evolution of the PDF is faster with respect to the case displayed in the top panel.

Finally, in the bottom panel, corresponding to $R = 0.08$, the situation drastically changes. Now the main acceleration source for particles comes from their interaction with the clouds and the steady electric field has a

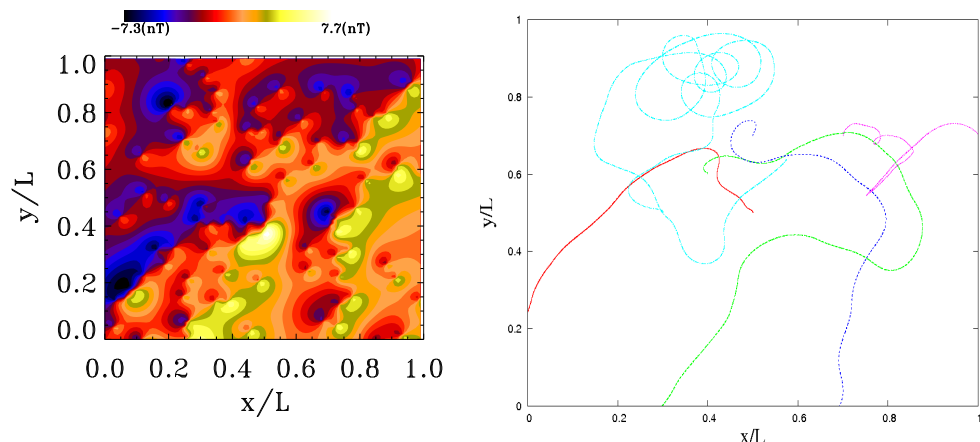## 2.2. DYNAMICS OF TEST PARTICLES IN STOCHASTIC ELECTROMAGNETIC FIELDS

Figure 2.13: Same as Fig. 2.12 but for $R = 0.08$.

minor importance for the particle dynamics. Indeed, the bulk velocity is decreased with respect to the previous cases; on the contrary, the PDFs of v_y are very wide and particles in the tails gain velocities of the order of 2000 km/s in very few minutes. We notice that an acceleration time of roughly 10 minutes is comparable to the time a proton needs to cross the magnetotail under a free acceleration by E_y, so that the Fermi acceleration mechanism can be considered very fast. On the other hand, the shape of the velocity distribution remains close to a Gaussian, that is, no power law tails are developed, in agreement of what has been observed in Sec. 2.2.2. This is shown in the inset of the bottom panel of Fig. 2.14, where the PDFs of the standardized variables, $(v_y - \langle v_y \rangle)/\sigma_{v_y}$ ($\langle v_y \rangle$ is the ensemble average of v_y and σ_{v_y} the standard deviation), are displayed in log-lin scale for the same times plotted in the bottom main panel.

In Figure 2.15, we compare the steady state energy distribution function for the three sets of parameters, along with the initial Gaussian energy distribution. We can notice that the energy gain increases with the size of the clouds, which means that the interaction with them is stronger. In particular, for $R = 0.032$ and $R = 0.08$, the energy acquired by particles is substantially larger than the potential drop of 20 keV in the simulation box, due to E_y and represented by the vertical dashed line in Figure 2.15. Increasing the cloud interaction, the energy grows up to 100 keV. This allows to explain the observations of 100 keV ions coming from the distant magnetotail [47].

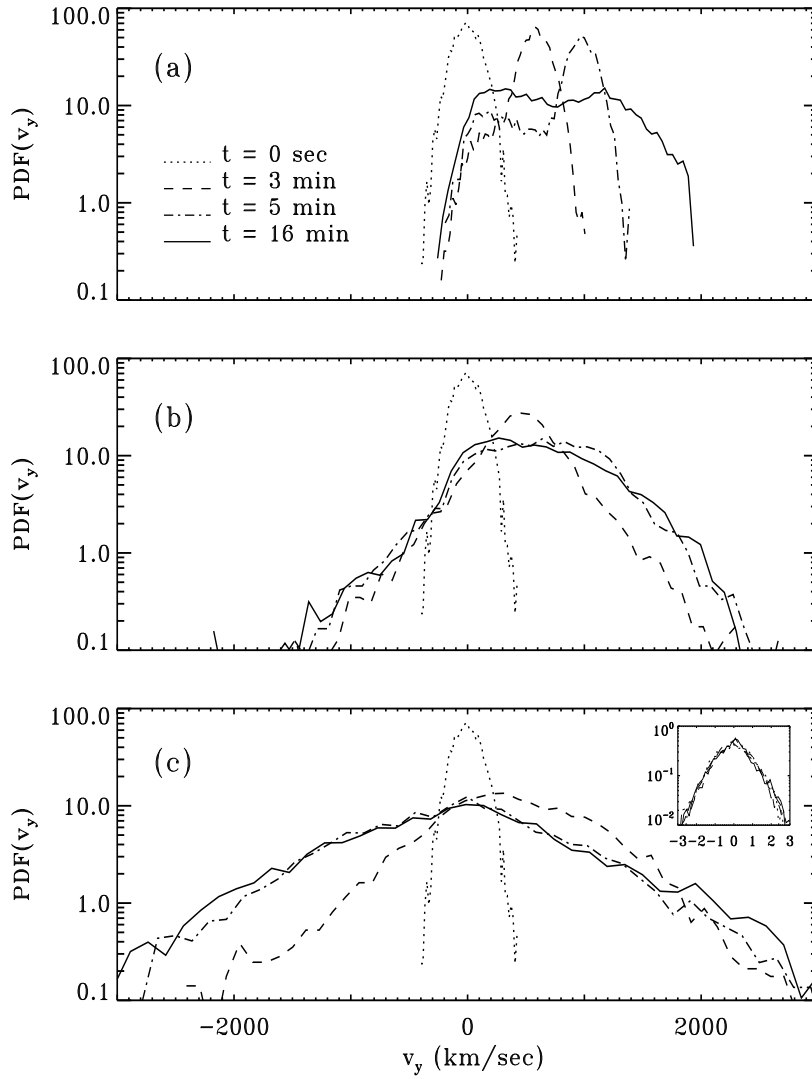From this study, a competition between stochastic and direct acceleration

Figure 2.14: Evolution of the ion distribution function for $E_y = 0.2$ mV/m and for $R = 0.016$ (top panel), $R = 0.032$ (middle panel), and $R = 0.08$ (bottom panel) in log-lin scale.
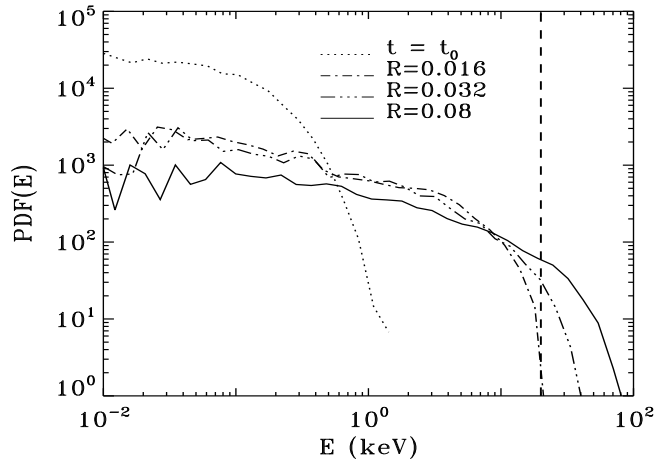
Figure 2.15: Energy distribution functions for the various simulations. The vertical dashed line at 20 keV corresponds to the potential drop across the simulation box due to E_y. The dotted line represents the energy distribution at injection, while the dashed-dotted, the dashed-dotted-dotted, and the solid lines represent the steady state energy distribution functions for $R = 0.016, 0.032, 0.08$.

mechanisms gives rise: in the first case analyzed, with $R = 0.016$ (see top panel of Fig. 2.14), the interaction between particles and cloud electromagnetic fields is weak, then the cross-tail electric field is the main mechanism for particle acceleration. When the cloud dimension increases, the interaction becomes stronger, so that the Fermi-like mechanism becomes competitive, and could even mask the steady effect of the constant electric field (see bottom panel of Fig. 2.14), leading to a randomization of the velocities and to an increase in the energy gained by particles. Assuming realistic values of the parameters, this mechanism allows to reach the required energies in the short times the ions spend in the magneotail performing Speiser orbits, so that it appears to be very competitive. This work is an attempt to explain some observations in the magnetospheric environment by using a 2D model of stochastic, Fermi-like acceleration. It could be also applied to other astrophysical contexts, as the acceleration of particles at the solar wind termination shock.

2.3 Particle acceleration in a Fermi-Ulam-like model

The model proposed by Fermi [8] for the acceleration of cosmic rays, discussed in Sec. 2.1, became rapidly popular and it was referred as a paradigm for further studies in a wide range of different physical systems [53, 54, 55, 56]. For example, within a dynamical systems framework, a very simple model for studying the acceleration of particles is the so called Fermi–Ulam model (FUM) [57, 58, 59, 60, 61, 62]. It describes the bouncing of a ball between a sinusoidally oscillating wall and a fixed one. This system can be written as a two-dimensional map, whose coordinates are the velocity of the ball after a collision with the wall and the phase of the moving wall [63]. A simplified version of the FUM has been proposed in order to reduce computational time [58, 64]. In this system the displacement of the wall is ignored and only the momentum exchanged between the ball and the wall is retained. However, this model underestimates the acceleration, and further modifications have been done by taking into account the effect of the wall displacement [61]. When both the original and the modified FUMs have been run for an ensemble of particles with a well defined distribution function, an energization of the whole distribution function has been observed. This means that distribution functions of particles collected at different times can be properly rescaled to the initial one. The energization of the bulk of particles can be observed also in numerical simulations of particles in turbulent [65] and stochastic fields [36], as it has been largely discussed in Sec. 2.2.

However, observations in astrophysics and in space plasmas often highlight the presence of collimated beams of accelerated particles. For example, solar flares are characterized by the presence of particle beams [66, 67] which form a different population with respect to the core, and the already mentioned field-aligned ion beams detected in the PSBL (see Sec. 2.2.3). Even if beams of accelerated particles have never been observed in the framework of stochastic acceleration mechanisms (but just an energization of the particle bulk population), it has been conjectured [42] that the formation of beamlets could be due to the interaction between particles and moving magnetic structures, with the aid of some underlying selection mechanism. The aim of this work is to show that beamlets could be produced also within a Fermi-like mechanism.

2.3. PARTICLE ACCELERATION IN A FERMI-ULAM-LIKE MODEL

2.3.1 The 1D model

The present model is a version of the FUM [57] in which non-relativistic charged particles of mass m move between magnetic clouds of mass $M \gg m$, along the x direction (each quantity depends only on this direction). The boundaries of magnetic clouds, that correspond to the moving wall in the FUM, are initially placed at positions $s_k X_0$. The index k stands for left (L) and right (R) respectively, and $s_k = \pm 1$ indicates the sign according to the fact that the boundary of the L cloud is placed initially at position $-X_0$, while the boundary of R cloud is placed at X_0. The regions of space $x \leq -X_0$ and $x \geq X_0$ correspond, respectively, to the L and R cloud. Each boundary moves independently following a given oscillating functional shape described by

$$X_k(t) = s_k X_0 + A_k \sin(\omega_k t + \alpha_k) \tag{2.14}$$

around the positions X_0 (ω_k represents the frequency of the oscillating motion, A_k the amplitude of the motion and α_k the random phase chosen in the range $[0, 2\pi]$). The distance $\ell(t)$ between the clouds is assumed to be greater than zero for all times t. A particle between the clouds moves following the Newtonian laws of motion for a point body: if $V = dX/dt$ and u represent respectively the velocities of a cloud and of the charge before a collision, after that the particle velocity becomes $-u + 2V$. Then the difference of energy before and after a collision $\Delta E = 2m(V^2 - \sigma|u||V|)$ depends on the relative (random) sign $\sigma = uV/|u||V|$ between the speed of the charge and that of the cloud during the collision. Head-on collisions ($\sigma = -1$) increase the energy of the particle by a factor ΔE, while tail-on collisions ($\sigma = 1$) lead to a decrease in energy.

According to the original idea by Fermi [8], clouds are viewed as regions of space where the magnetic field is concentrated and particle are allowed to penetrate [36]. The dynamics of the model is characterized by the integration of the equations of motion with a variable time step. However, since the dynamics depends on encounters between particles and clouds, a discrete variable n counting successive collisions has been introduced; a collision is defined through the time t_n at which $|X_k(t_n) - x_p(t_n)| < \epsilon$, where x_p is the particle position, and $\epsilon \ll 1$. Then, u_n and $\phi_n = \omega_k t_n mod(2\pi)$ represents the particle speed and the phase of the oscillating cloud after the n-th collision, respectively. Since clouds represent regions of space where the magnetic field is concentrated, a particle does not actually collide with a rigid wall, but when it arrives at the cloud position at time t_n with speed u_{n-1}, it can penetrate
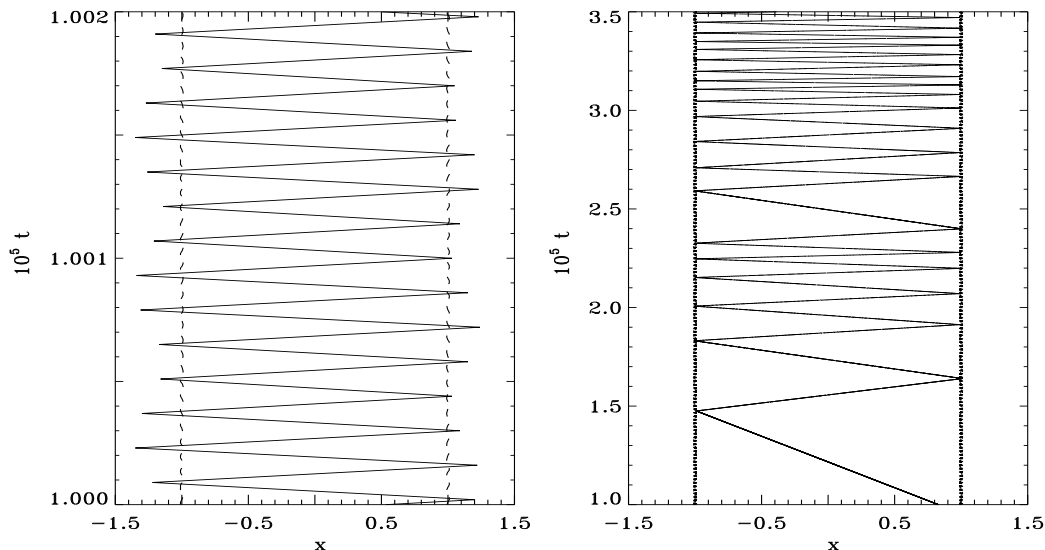
Figure 2.16: The space-time behavior of two test particles moving between the clouds (full lines) is showed for two values of b_0, namely $b_0 = 2 \times 10^{-5}$ (left panel) and $b_0 = 2 \times 10^{-7}$ (right panel). The oscillating positions of the clouds, being amplitudes of the motion very low compared to the distance between them, are viewed as a couple of vertical dotted lines at $x = \pm 1$.

the cloud before being reflected with speed u_n by the action of the Lorenz force. We assume that the particle penetration depth is $r_n = B_n u_{n-1}$, where B_n is a random parameter which depends on the magnetic field intensity within each cloud. As far as the value of u_n is concerned, inside the cloud particle can radiate energy at the Larmor rate proportional to its squared acceleration [55]

$$\frac{dQ}{dt} \sim -\gamma(u_n^* - u_{n-1})^2, \tag{2.15}$$

here $u_n^* = -u_{n-1} + 2V_n$ is the velocity of the particle without considering the energy losses via radiation emission. Then, the particle velocity after the n-th collision is given by [55]

$$u_n = \text{sign}\{u_n^*\} \left[|u_n^*| - \mu(\gamma)|u_n^* - u_{n-1}|\right], \tag{2.16}$$

where μ is a dimensionless free parameter that depends on the amplitude of the radiation loss, that is γ. The corresponding energy is E_n, and the radiated energy is $Q_n = E_n^* - E_n$.

2.3.2 Statistical analysis and results

Eq.s (2.14) have been normalized by using as normalization parameters X_0 for lengths and $1/\omega_L$ for times,

$$X_L(t) = -1 + A_L \sin(t + \alpha_L)$$
$$X_R(t) = 1 + A_R \sin(\Omega t + \alpha_R),$$

where $\Omega = \omega_R/\omega_L$ is a parameter of the system. Particle velocities are normalized to the thermal speed u_{th}, therefore, the other parameters are $b_n = [B_n u_{th}/(X_0 \omega_R)]\Omega$, which is uniformly distributed in the range $b_n \in [0, b_0]$, and $\mu = [2\gamma/(m\omega_R)]\Omega$.

The investigation on the dynamics of the model is performed by varying the parameters Ω, b_0, and μ. The other quantities remain unchanged, that is $A_L = A_R = 0.01$, the initial particle speed is randomly chosen in the interval $[-1, 1]$ and the particle is injected at a random position between the two clouds. In Fig.s 2.16 the trajectories of a test particle between the clouds for two values of b_0, namely $b_0 = 2 \times 10^{-7}$ and $b_0 = 2 \times 10^{-5}$, indicating the different penetration inside the clouds, are displayed. In this case $\mu = 0$, that is the particle does not radiate energy.

In order to investigate how the value of the penetration inside a cloud influences the particle motion, the temporal variation of the particle energy is studied by varying the parameter b_0. In Fig.s 2.17 the time evolution of the energy of a particle for three different values of b_0 is displayed. In the upper panel the energy is burst-like, meaning that the particle can completely lose its energy, becoming quasi-stable for a finite period. In this case b_0 is very small and the system tends to be similar to a standard FUM; by increasing the value of the particle penetration, a different behavior occurs, that is the cooperative effect of the two oscillating clouds can confine the energy of the particle by breaking the usual Fermi mechanism. The energy is acquired by the system (owing to head-on collisions), but after an initial transient, it remains almost constant around a given value and is never completely lost in successive encounters with clouds.

This difference can be also highlighted by looking at the phase space (u_n^2, ϕ_n), where each point represents a single collision. In Fig.s 2.18 the
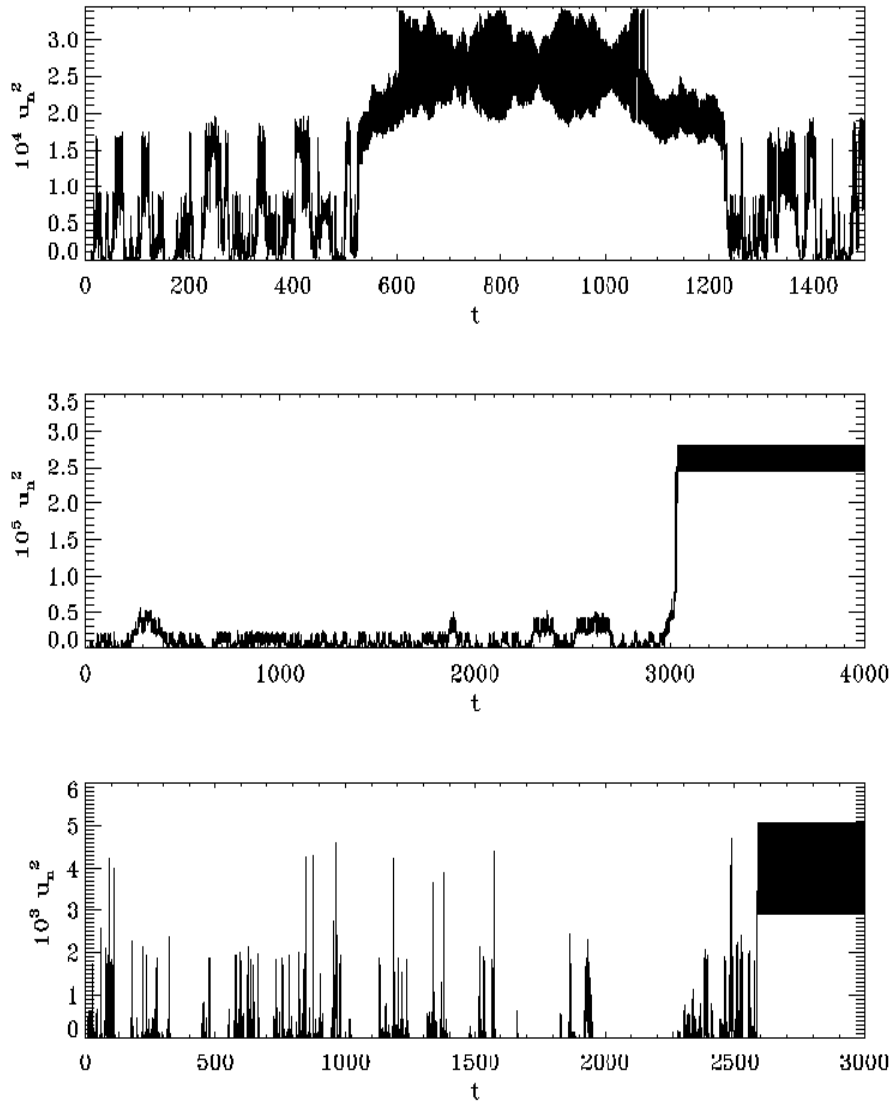
Figure 2.17: Velocity square gained by a test particle as a function of time for a system with $\Omega = 1$. From top to bottom the penetration depth increases, namely $b_0 = 2 \times 10^{-7}$, $b_0 = 2 \times 10^{-6}$, and $b_0 = 2 \times 10^{-5}$.
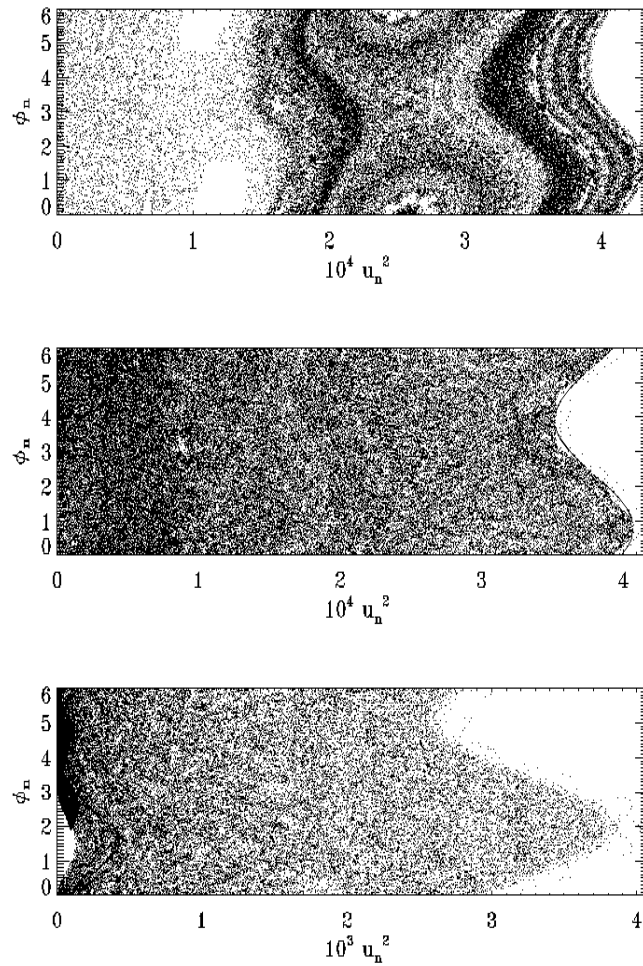
Figure 2.18: Phase space (u_n^2, ϕ_n) of a test particle for a system with one fixed and an oscillating cloud ($\Omega = 0$), with $b_0 = 2 \times 10^{-7}$ (upper panel), $b_0 = 2 \times 10^{-6}$ (middle panel) and $b_0 = 2 \times 10^{-5}$ (lower panel). The value of μ is set to 0.
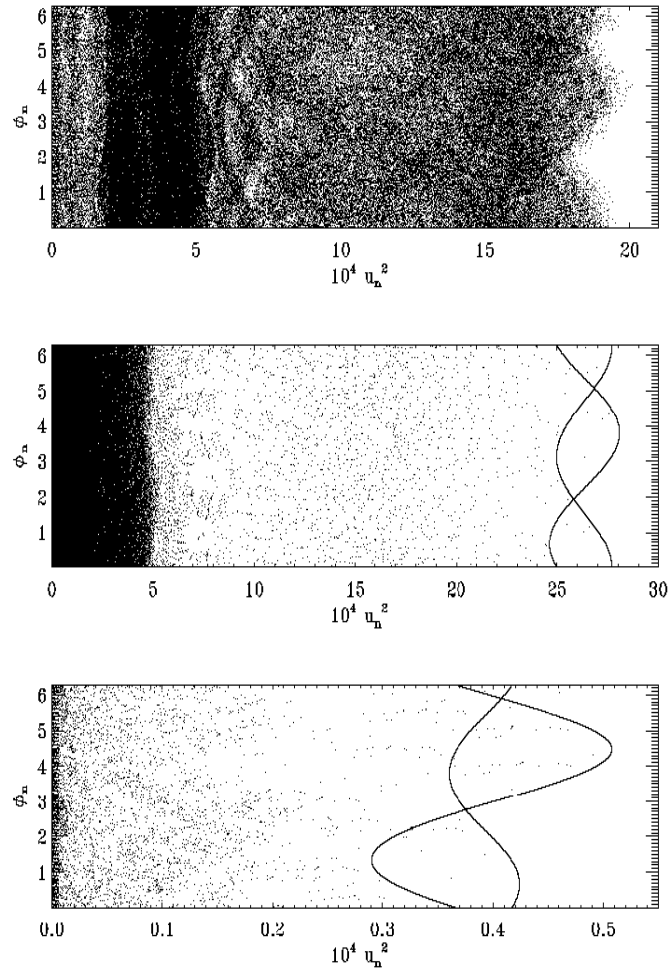
Figure 2.19: The same of Fig.s 2.18 but for $\Omega = 1$.

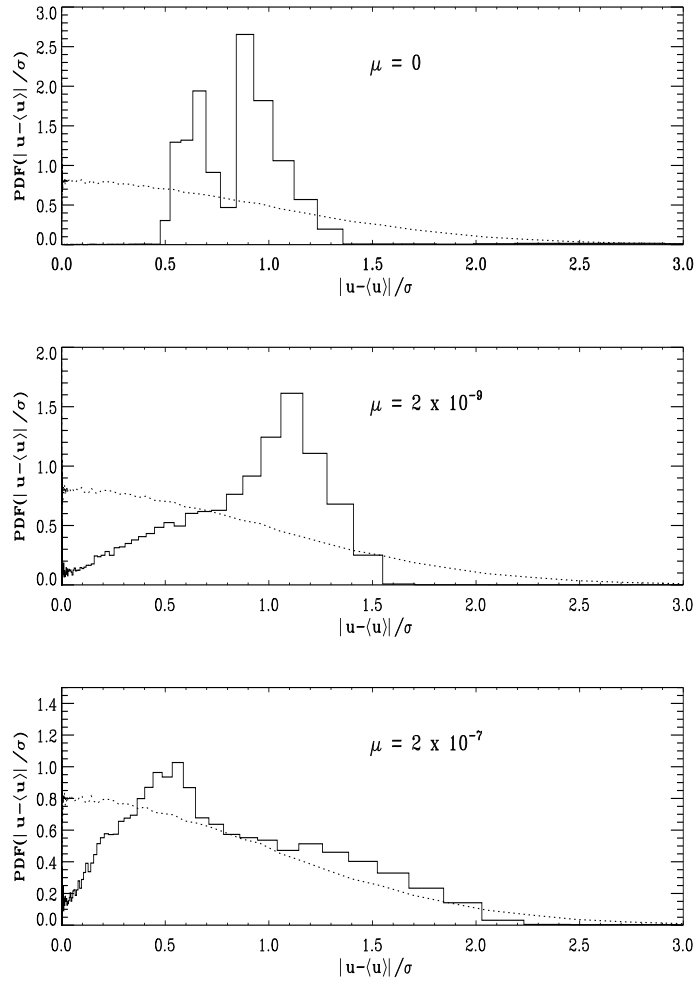Figure 2.20: PDFs of the absolute value of standardized velocity fluctuations of an ensemble of 10^6 particles for $\mu = 0$ (upper panel), $\mu = 2 \times 10^{-9}$ (middle panel) and $\mu = 2 \times 10^{-7}$ (lower panel). Dotted line refers to the initial maxwellian distribution, solid line corresponds to the distribution of particles at time $t_{max} = 5 \times 10^5$. The oscillation frequencies ratio is $\Omega = 1$.

phase space for a system with an oscillating cloud and a fixed one is displayed, by varying b_0 from top to bottom. When it assumes a value close to zero, the phase space is characterized by the presence of KAM islands as in the case of the classical FUM [58]. KAM islands are region of the phase space representing regular (non chaotic) trajectories, along which the system is integrable [2]. These curves are destroyed when b_0 increases, owing to a growth in the stochasticity of the system. When both clouds oscillate (see Fig.s 2.19), particle is "captured" by the clouds through a kind of resonance effect. It continues to oscillate between clouds but the Fermi mechanism is, in some sense, broken: energy is neither gained nor lost anymore, both tail-on and head-on collisions work in a cooperative way.

The confinement of energy of a test particle depends also on the value of μ, that is on the fact that it can lose energy not only through tail-on collisions but also through radiative emission. Of course the lower the value of μ the more test particles are captured through the resonance effect. When the parameter b_0 is nearly zero, the resonance effect is spread over a wide region in the phase space (see upper panel of Fig.s 2.19).

Since now, the dynamics of a single test particles has been investigated. It is reasonable to extend the analysis to an ensemble of test particles put into the system of oscillating clouds. We could expect that the effect of the energy confinement on each particle breaks the usual random acceleration mechanism leading to a modification of the initial distribution function. By following the motion of an ensemble of 10^6 particles for a time $t_{max} = 5 \times 10^5$, after which it is assumed that the whole ensemble of particles leaves the region between the clouds, a statistical analysis is computed. Particles are injected at random positions into the system with initial velocities extracted from a 1D Maxwellian distribution normalized to the unitary thermal velocity, that is

$$P(u) = \frac{1}{\sqrt{2\pi}} \exp[-u^2/2].$$
(2.17)

In particular, we are looking for possible modifications of the PDF of particle velocities at time t_{max}, with respect to the initial distribution. In Fig.s

---

[2]The survival of these structures under a non-integrable perturbations is a question widely studied in literature [68, 59]. Indeed, Kolmogorov conjectured that KAM tori survive when an analytic and M times continuously differentiable perturbation is applied. However, in several dynamical systems with no differentiable perturbations tori still survive. Sometimes Hamiltonian systems exhibit a coexistence of chaotic regions and exactly integrable islands (local integrability) [68].
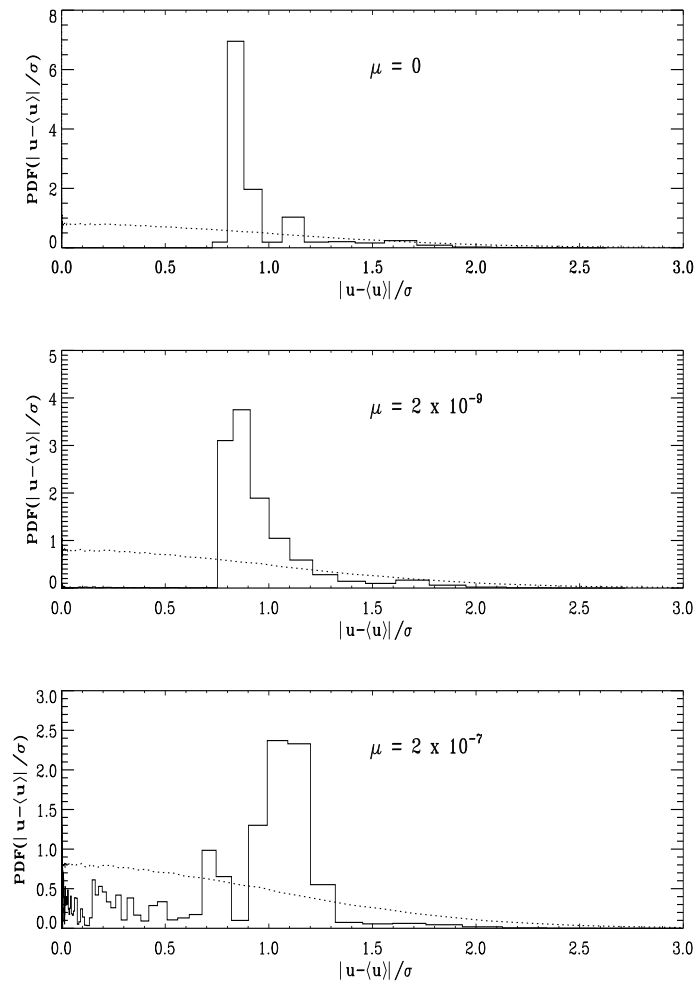
Figure 2.21: The same as Fig. 2.20 but for $\Omega = \sqrt{2}$.

Figure 2.22: PDFs of the absolute value of standardized velocities of an ensemble of 10^6 particles for $\mu = 0$ and $\Omega = 1$. Dotted line represents the initial maxwellian distribution, solid lines correspond to the distributions of particles at time $t_{max} = 5 \times 10^5$ for the cases $b_0 = 2 \times 10^{-5}$ (upper panel), $b_0 = 2 \times 10^{-6}$ (middle panel), and $b_0 = 2 \times 10^{-7}$ (lower panel).

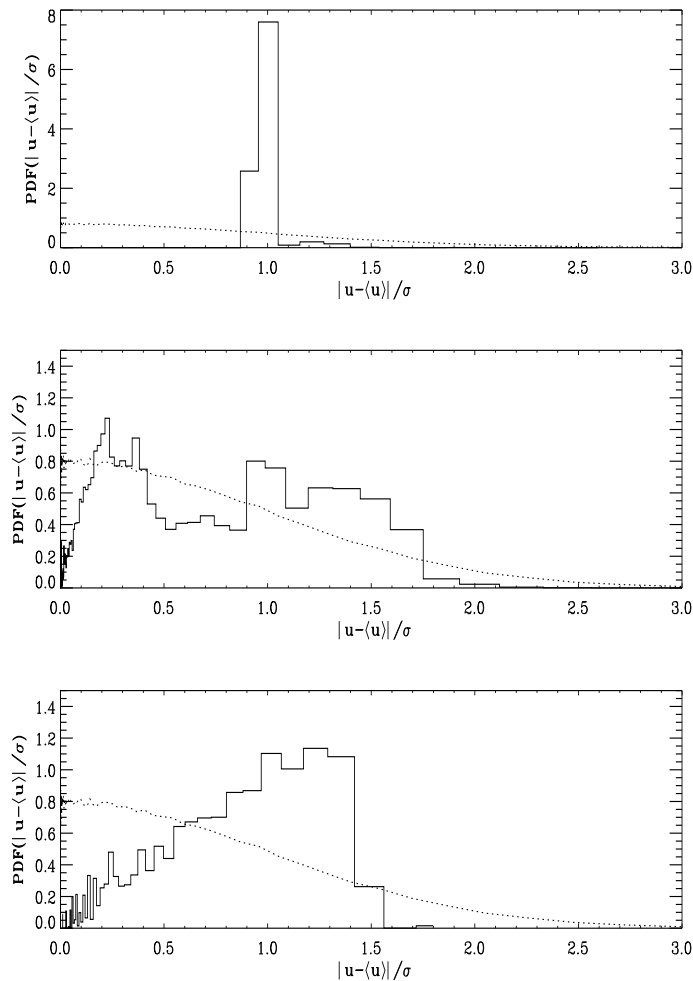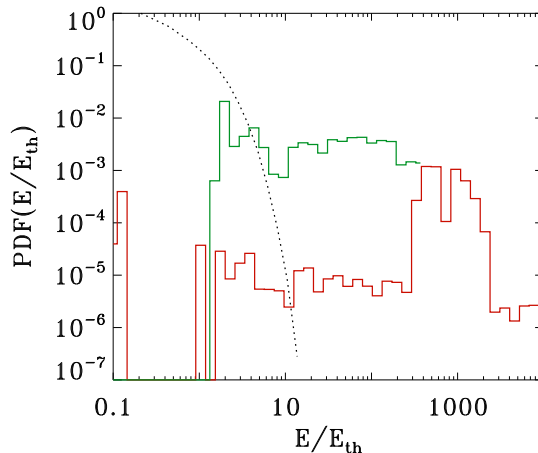Figure 2.23: Probability density functions of particle energies normalized to the thermal energy. Dotted line refers to the initial Maxwellian distribution, the red line is for a system realization with $b_0 = 2 \times 10^{-5}$, while the green line refers to $b_0 = 2 \times 10^{-6}$.

2.20 PDFs of the absolute value of the standardized velocity fluctuations $(u - \langle u \rangle)/\sigma$, collected at time t_{max}, compared to the initial one, for three values of the parameter μ and for $\Omega = 1$ are shown. The main feature of PDFs is the clear formation of a beam, at variance with the usual Fermi-like mechanism for which a maxwellian distribution with a larger thermal velocity would be expected at the final time; after a time t_{max}, all particles gain more or less the same energy thus generating a quasi mono-energetic beam. This is more visible for lower values of μ, namely when μ increases the beam broadens and the ensemble of particles tends to become maxwellian. A beamlet is clearly formed even in the case of non rational ratio between oscillation frequencies, i.e., $\Omega = \sqrt{2}$, as it can be seen in Fig.s 2.21, and, at variance with the case $\Omega = 1$, it survives even for larger values of μ (cfr. lower panel of Fig.s 2.20 and 2.21).

The generation of beamlets of energetic particles observed in Fig.s 2.20 and 2.21 is also evident by varying the parameter b_0, i.e., the distance covered by particle inside a cloud. Indeed, in Fig.s 2.22 PDFs of the standardized velocities at t_{max}, for three values of b_0, and for $\mu = 0$ are displayed. The

formation of one or more beamlets is clearly visible in all cases, especially
when particles can penetrate a longer distance inside the clouds, that is when
b_0 is large, owing to the capture of particles by the system of two oscillating
clouds (resonance effect).

The results shown in this Section underline that the stochastic accelera-
tion, without any external electric field, should be a good physical mechanism
to increase the velocity of one or more beams of particles to about 10-100
times their initial thermal speed (depending on the free parameters). This is
clear when looking at the PDFs of energies acquired by particles at a given
time: in Fig. 2.23 the PDFs of particle energies normalized to the thermal
energy are shown for two values of the b_0 parameter. Beamlets formation at
energy 10-1000 times the initial thermal energy is evident [69]. This result is
in good agreement with the observations of ion beamlets inside the Earth's
magnetotail, indeed these structures have velocities of about 600-2000 km/s,
that is about 3-10 times the thermal speed of the ambient particles, which is
typically of the order of $u_{th} \simeq 200$ km/s [46, 42]. Just for making a compar-
ison with some physical conditions in space plasmas, the oscillating clouds
present in this model can be associated to oscillations of magnetic structures
driven by typical instability mechanisms [70], as for example the thermal
instability [71] or the tearing instability [72, 73].

Chapter 3

Transport of particles through the heliosphere

3.1 The Diffusive Shock Acceleration theory

Solar flares, CMEs, interplanetary shocks, and planetary magnetospheres are sources of energetic particles observed both in space and at ground level. The propagation of such particles in the interplanetary medium is one of the most challenging subjects in space physics, indeed, understanding how particles spread out in space is important for assessing the propagation of particles coming from the Sun and approaching the Earth's atmosphere (especially for space weather forecasts), for cosmic rays acceleration and transport, and even for evaluating the influence of extragalactic cosmic rays on the fossil diversity on Earth [74]. Transport of particles is influenced by various phenomena, as, for example, the solar activity, the level of turbulence in the heliosphere, which causes pitch angle scattering and perpendicular transport of magnetic field lines [20, 75, 21, 27, 76], the energy of particles themselves, and the presence of discontinuities. As it has been discussed briefly in the Introduction of Chapter 2, normal diffusion has long been considered, also in connection with the diffusive shock acceleration (DSA) theory [10, 12, 11, 77, 78], because of the agreement with many observational features, as the cosmic rays power law spectra [79]. DSA was developed in order to explain the origin of Galactic cosmic rays [10, 12] but, subsequently, it was extended to other astrophysical systems, as the Earth's bow shock [80], corotating interaction region shocks [81], and the solar wind termination shock (TS) [82]. Further,

by using satellite observations, it has been possible to investigate the dynamics of energetic particles coming from the Sun owing to the high recurrence of solar energetic particle (SEP) events. Studies based on data revealed that SEP events can be divided in two classes: "impulsive" and "gradual" events. The former are associated to magnetic reconnection processes during solar flares, the latter to a diffusive shock acceleration mechanism at an evolving interplanetary shock driven by a CME [78].

DSA theory considers a shock front propagating in a plasma medium permeated by magnetic irregularities which scatter energetic particles present. If energetic particles have a gyroradius much larger than the shock thickness (usually considered of the order of the ion skin depth, $\lambda_i = c/\omega_{pi}$, being c the speed of light and ω_{pi} the plasma frequency), the acceleration mechanism is not influenced by the internal shock structure and a continuous passage of particles between regions upstream and downstream of the shock front is possible. This condition is usually well satisfied by ions, while for electrons very high injection velocities are required. In Ref.s [10, 12, 11] it has been hypothesized that there exists a source of wave turbulence, with characteristic wave velocity smaller than the particle velocities, in the vicinity of the shock region, able to scatter energetic particles in pitch angle, leading to an isotropization of the particle distribution function. Thus, close to the shock front, where the level of turbulence is very high, particles can be repeatedly scattered from upstream to downstream and vice-versa and, then, accelerated by a first-order Fermi process. Since the streaming velocity of particles escaping upstream, after being accelerated at the shock front, is greater than the Alfvèn speed with respect to the background plasma, energetic particles themselves are capable to excite Alfvèn waves upstream of the shock and to be scattered by this self-generating wave turbulence [12]. The motion of particles going back and forth through the shock front is described in terms of the standard diffusion equation for the distribution function f [11], which in the one-dimensional case (as for example for an infinite planar shock) is given by [83]

$$\frac{\partial f}{\partial t} - \frac{\partial}{\partial x}(D(x)\frac{\partial f}{\partial x}) + V\frac{\partial f}{\partial x} - \frac{1}{3}\frac{\partial}{\partial x}(Vp)\frac{\partial f}{\partial p} = Q(x,t,p), \qquad (3.1)$$

where the right-hand side indicates a source term, V is the background plasma bulk velocity along the x direction, $D(x)$ is the spatial diffusion coefficient, and the last term in Eq. (3.1) describes the work performed by the background plasma on accelerating particles [11]. By assuming that the

shock front is placed at $x = 0$, the upstream region is that at $x < 0$ having a plasma bulk velocity V', while the downstream region is at $x > 0$ with V''. If particles are injected at $x = -\infty$ as a monoenergetic population of momentum p_0 and by imposing stationarity and continuity at $x = 0$, the solutions of Eq. (3.1) upstream and downstream of the shock are respectively [11]:

$$f(x, p) \simeq \frac{3}{p_0} r \left(\frac{p}{p_0}\right)^{-3r} \exp[V'x/D(p)], \qquad x < 0 \qquad (3.2)$$

$$f(x, p) = \frac{3}{p_0} r \left(\frac{p}{p_0}\right)^{-3r}, \qquad x > 0 \qquad (3.3)$$

where $r = V'/(V' - V'')$ is the compression ratio of the shock. Then, by assuming a normal diffusive transport for particles accelerated at a shock front, the distribution function at a given energy in the region upstream is a simple exponential decay. Note that here the assumption of a homogeneous plasma upstream and downstream has been taken into account, indeed, the diffusion coefficient depends only on the particle momentum [11]. However, a large number of *in situ* data shows that such profiles are not always observed [84], but there is a variety of different behaviors [85]. In addition, recent observations of SEP events highlight transport properties varying from diffusive to scatter-free (ballistic) regimes [86, 87, 88], and the proton parallel mean free path ranging from $\simeq 0.1$ AU [89] to more than 1 AU [90, 87]. In a recent paper, Ref. [78] emphasizes that transport can be diffusive in a layer around the shock, and nearly scatter-free farther away from the shock. Clearly, a more quantitative description of such a scatter-free regime is needed.

Recent numerical simulations of particle propagation in presence of magnetic turbulence have highlighted that subdiffusive regimes for particle perpendicular transport [26, 27] and superdiffusive regimes for particle parallel transport [27, 76] are possible, depending on the turbulence level, the turbulence anisotropy, and the ratio of the Larmor radius over the turbulence correlation length. Anomalous transport regimes, characterized by a mean square displacement growing as $\langle x^2(t) \rangle \propto t^{2\nu}$, both slower ($\nu < 1/2$) and faster ($\nu > 1/2$) with respect to Gaussian diffusion ($\nu = 1/2$), have been found in a large variety of systems [91, 92, 29, 93, 36]. The faster regime (superdiffusion) is also characterized by Lèvy random walks which have a Lèvy (power law) distribution for the probability of the jump lengths with diverging second-order moment (see Section 2.2.1). Thus, in order to interpret the observations, it is important to understand whether, under appropriate conditions, anomalous transport is possible for energetic particles propagating

through the heliosphere. In this work, by studying the temporal profiles of
particles accelerated at interplanetary shock waves and at the termination
shock (TS) of the solar wind, evidences of superdiffusive transport both for
electrons [94, 95] and for ions are shown.

3.2   Propagator formalism

A spacecraft in the solar wind measures particles accelerated at various times
and positions, and the actual time profile reflects the propagation properties
from the source to the observer, as well as the source evolution. The propa-
gation of particles, accelerated by interplanetary shock waves and at the TS,
away from the shock is considered. As said above, particles undergo Fermi
acceleration by means of repeated crossings of the shock, thanks to diffusive
motion in the regions upstream and downstream of the shock [12, 10, 11].
However, in this analysis we are not concerned with the acceleration mecha-
nism, but with propagation away from the shock front.

The assumption of a large planar shock can be considered reasonable for
interplanetary shocks, which may be due either to fast CMEs or to corotating
interaction region shocks (CIRs), thanks to their large size (compared to the
relevant transport scales). CIR shocks form in some regions of the interplan-
etary space where the fast solar wind ($V_{\rm sh} \simeq 800$ km/sec), coming from solar
coronal holes, encounters the slow wind ($V_{\rm sh} \simeq 400$ km/sec), coming from
solar equatorial regions (see Fig. 3.1), giving rise to two collisionless shocks
moving in opposite directions (the reverse one sunward, and the forward one
anti-sunward) and including a compression region between them (see Fig.
3.2). In particular, CIR shocks form a spiral on the equatorial plane with
a radius of curvature comparable to the heliocentric distance. The scale of
these shocks is very large (several AU) and in a first approximation they can
be assumed to be planar.

The solar wind TS is the region of space at nearly 75-95 AU where the
supersonic and superalfvènic solar wind slows down to subsonic speed, due
to the interaction with the local interstellar medium (LISM) (see Fig. 3.3).
This causes a compression region characterized also by an enhanced level of
energetic particles, indeed TS is considered a source of accelerated particles.
Firstly Voyager 1 at the end of 2004 and later Voyager 2 in 2007 crossed the
TS, by allowing us to have precious information on this far and unknown re-
gion of the interplanetary space. Also in this case the shock can be viewed as
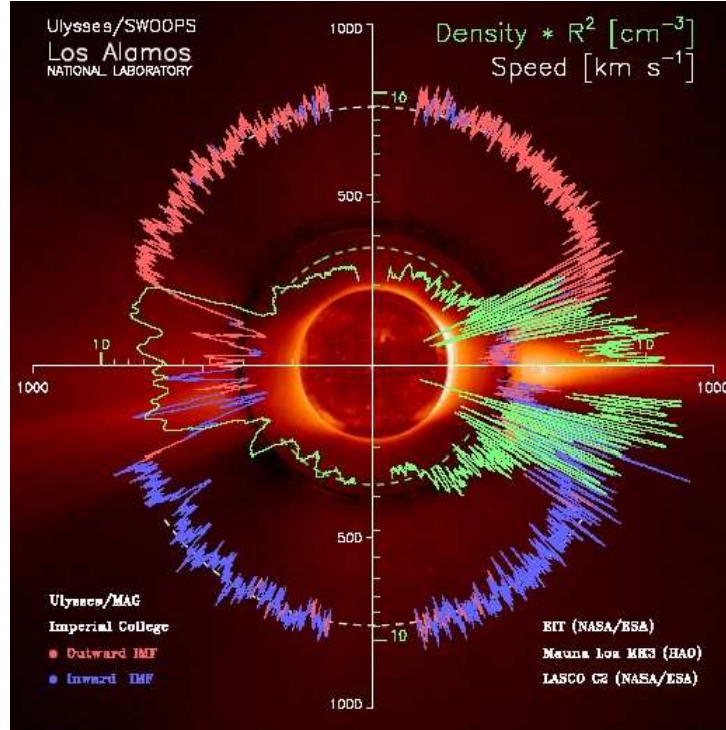
Figure 3.1: Solar wind density and solar wind speed from the SWOOPS plasma instrument (PI D. McComas) and magnetic field data plot from the MAG instrument (PI A. Balogh) on board Ulysses.

a planar structure. Accordingly, we consider a steady state, one dimensional shock model for both the physical systems under analysis.

In general a way of treating particle transport properties is the probabilistic formalism which uses propagators. A propagator, defined as $P(\mathbf{r}, t)$, is the probability of finding a particle in $(\mathbf{r}, t)$ if injected at the origin of a coordinate system. In other words, the propagator is the solution of the transport equation when the initial distribution is localized both in space and time as a δ-function, $P(0, 0) \simeq \delta(x)\delta(t)$ (see Section 51 of Ref [96]). In a one-dimensional geometry, the energetic particle fluxes measured by a spacecraft at (x, t) can be viewed as the superposition of the energetic particles accelerated at the shock moving according to $x' = V_{\mathrm{sh}}t'$ (in other words, at $t' = 0$ the shock will be at the origin of the coordinate system), with V_{sh}
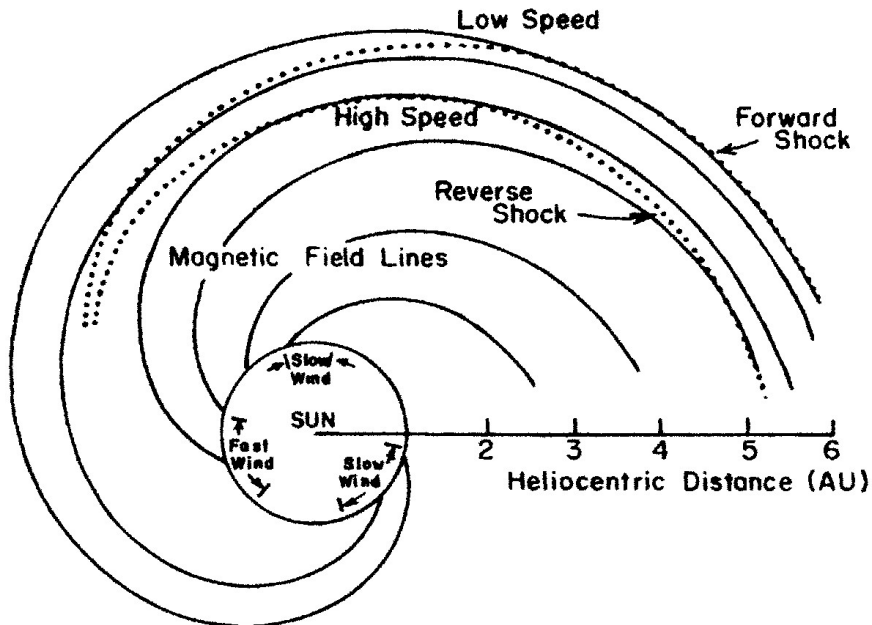
Figure 3.2: Cartoon of a corotating interaction region in a reference frame corotating with the Sun (from *Gosling et al., 1976*).

assumed to be constant. To fix the ideas, the observer is at $x = 0$, upstream of the shock, which is coming from $x = -\infty$; then, $t < 0$ for the relevant time interval. The particle omnidirectional distribution function $f(x, E, t)$ at the observer will be expressed in terms of the distribution function $f_{\mathrm{sh}}(x', E, t')$ of particles accelerated at the shock as

$$f(x, E, t) = \int P(x - x', t - t') f_{\mathrm{sh}}(x', E, t') dx' dt' \tag{3.4}$$

with $f_{\mathrm{sh}}(x', E, t') = \lambda f_0(E) \delta(x' - V_{\mathrm{sh}} t')$, where $f_0(E)$ represents the distribution function of particles of energy E emitted at the shock front and λ is a characteristic length. Here, $P(x - x', t - t')$ is the probability of finding a particle at position x at time t, if it was injected at x' and t'.
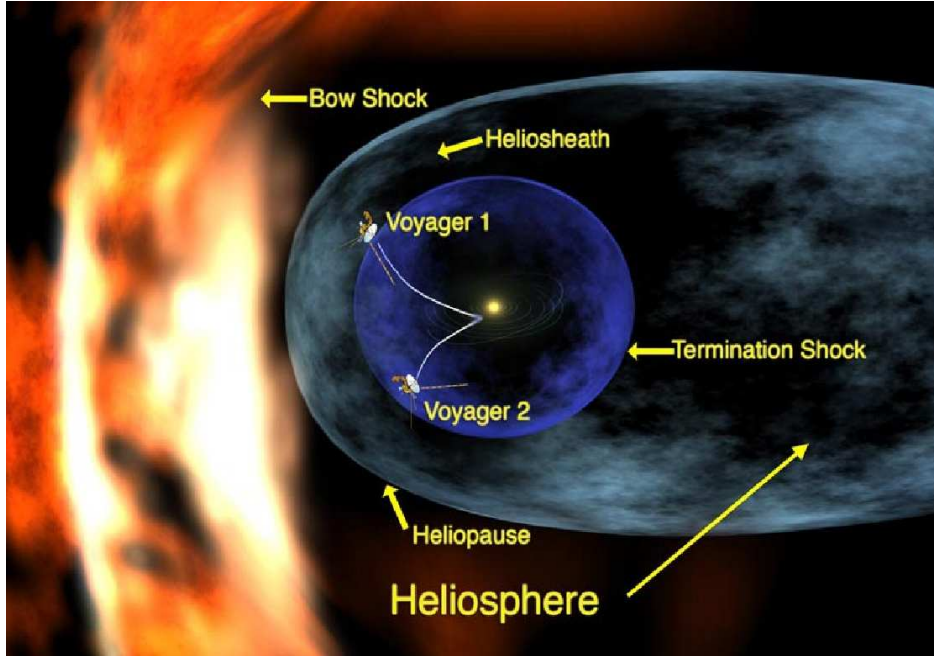
Figure 3.3: Cartoon of the interaction between the solar wind and the local interstellar medium. The positions of both Voyager 1 and Voyager 2 spacecraft are also shown in the period before the Voyager 2 TS crossing.

Normal transport

In the case of normal diffusion, particles accelerated at the shock are spread in space according to the Gaussian propagator [93, 97]

$$P(x - x', t - t') = \frac{C}{\sqrt{4\pi D(t - t')}} \exp\left[-\frac{(x - x')^2}{4D(t - t')}\right], \qquad (3.5)$$

where $x - x'$ is the distance upstream of the shock (the source of energetic particles), $t - t' > 0$, because of causality, C is a constant with dimension $[1/t]$, and D is the Gaussian diffusion coefficient. This form, $P(x - x', t - t')$, emphasizes the space-time translational invariance of the propagator. As considered by Ref.s [98, 78], the diffusion coefficient can be smaller close to the shock because of the enhanced level of turbulence self-consistently generated by particles accelerated via the DSA mechanism. To exploiting

translational invariance, we assume to be at some distance upstream of the
shock, where D is constant and the solar wind is statistically homogeneous.
Using the expression of the propagator in Eq. (3.5), it is possible to write
[99]

$$f(x, E, t) = \int \frac{C}{\sqrt{4\pi D(t - t')}} \exp\left[-\frac{(x - x')^2}{4D(t - t')}\right] f_0(E)\delta(x' - V_{sh}t')dx'dt'.$$

(3.6)

Exploiting the δ function, considering that the observer is at the origin of
the coordinate system $x = 0$ and by introducing the variable $\tau = t - t'$, the
particle distribution function is obtained, that is

$$
\begin{aligned}
f(0, E, t) &= f_0(E)\exp\left(\frac{V_{sh}^2 t}{2D}\right)\int_0^\infty \frac{C}{\sqrt{4\pi D\tau}}\exp\left[-\frac{V_{sh}^2 t^2}{4D\tau}\right]\exp\left[-\frac{V_{sh}^2 \tau}{4D}\right]d\tau \\
&\equiv f_0(E)\exp\left(\frac{V_{sh}^2 t}{2D}\right)I(t).
\end{aligned}
$$

(3.7)

It is easy to show that the integral $I(t)$ is finite, since the integrand goes to
zero for $\tau \to 0$, and decays exponentially for $\tau \to \infty$. Application of the
Laplace transform given by Eq. (2.12) of Ref. [97],

$$\int_0^\infty \frac{1}{\sqrt{\tau}}\exp(-s\tau)\exp(-\frac{\alpha}{4\tau})d\tau = \left(\frac{\pi}{s}\right)^{1/2}\exp\left(-\alpha^{1/2}s^{1/2}\right),$$

(3.8)

taking into account that $t < 0$, gives $I(t) = V_{sh}^{-1}\exp(-V_{sh}^2|t|/2D)$. Then,

$$f(0, E, t) = \frac{f_0(E)}{V_{sh}}\exp\left[-\frac{V_{sh}^2|t|}{D}\right]$$

(3.9)

which coincides with the exponential decay expressed in Eq. (3.2) for the
energetic particle distribution function upstream of the shock [11, 98]. How-
ever, at variance with Eq. (3.2), $V' = V_{sh}$ and $x = V_{sh}t$, indeed, upstream
and downstream regions are here interchanged.

Superdiffusive transport

Conversely, in the case of non Gaussian, superdiffusive propagation, trans-
port can be described in the framework of continuous time random walks. For
Lèvy random walks, a jump probability $\psi(r, t) = A|r|^{-\mu}\delta(t - r/v)$ of making

a jump of length r in a time t can be adopted [28, 92, 100, 30, 93]. The power law behavior of $\psi(r, t)$ reflects the fact that very long jumps of length r have small but non-negligible probability, contrary to the case of Gaussian random walk, that is a different statistics is involved. For $\mu < 3$, the probability $\psi(r, t)$ has diverging second order moment, which corresponds to an infinite value of the mean free path; however, this does not imply an infinitely fast transport because long jumps require long times, as implied by the space-time coupling expressed by $\delta(t - r/v)$. In general, the propagator can be obtained in the Fourier-Laplace space and its explicit inversion is only possible in limiting cases: close to the source, that is for $|x - x'| \ll k_\mu^{1/2}(t - t')^{1/\mu - 1}$, the propagator behaves as

$$P(x - x', t - t') = a_0(t - t')^{1/(1-\mu)} \exp\left[-\frac{(x - x')^2}{k_\mu(t - t')^{2/(\mu - 1)}} \right], \qquad (3.10)$$

where a_0 and μ are constants [100], and k_μ is an anomalous diffusion constant (different from the anomalous diffusion coefficient D_ν introduced below), whose physical dimensions are $[l^2/t^{2/(\mu - 1)}]$; far off the source, for $|x - x'| \gg k_\mu^{1/2}(t - t')^{1/\mu - 1}$ the propagator has a power law behavior described by

$$P(x - x', t - t') = b\frac{t - t'}{(x - x')^\mu}, \qquad (3.11)$$

where b is a constant with dimension $[t^{-2}/l^{1-\mu}]$ and μ a dimensionless constant, however, they may depend on particle velocity and on the relevant transport process [100]; the propagator in Eq. (3.11) goes to zero for $x - x' > v(t - t')$, with v the particle velocity. Similar expressions of the propagator for superdiffusive transport have been obtained in the framework of fractional diffusion models, too [19, 101]. For $2 < \mu < 3$ superdiffusion with $\langle x^2(t) \rangle = 2D_\nu t^{2\nu}$ is obtained for large t, with $\nu = 2 - \mu/2$ [28, 92, 100, 30], while for $3 < \mu < 4$ transport is diffusive, but the propagator has non Gaussian, power law tails as above [100, 19].

Assuming to be at a large distance from the shock, that is in the tails of the probability distribution, it is possible to obtain the energetic particle profile by inserting the non Gaussian propagator given by Eq. (3.11) in Eq. (3.4):

$$f(x, E, t) = f_0(E)\lambda b \int \frac{t - t'}{(x - x')^\mu} \delta(x' - V_{\rm sh}t')dx'dt'. \qquad (3.12)$$

A first integration gives

$$f(x, E, t) = f_0(E)\lambda b \int_{t_0}^{t''} \frac{t - t'}{(x - V_{\text{sh}}t')^{\mu}} dt', \qquad (3.13)$$

where t_0 is the shock start time and t'' is a provisional end time [95]. By defining an integration variable $y = t - t'$, Eq. (3.13) becomes

$$f(x, E, t) = -f_0(E)\lambda b \int_{t-t_0}^{t-t''} \frac{y}{(x - V_{\text{sh}}t + V_{\text{sh}}y)^{\mu}} dy$$

$$= -f_0(E)\lambda b \int_{t-t_0}^{t-t''} \frac{y}{(\alpha + V_{\text{sh}}y)^{\mu}} dy,$$

where $\alpha = x - V_{\text{sh}}t$ in the integral is constant. Introducing $z = \alpha + V_{\text{sh}}y$, we get

$$f(z, E, t) = -f_0(E)\lambda b \int_a^b \frac{\left(\frac{z-\alpha}{V_{\text{sh}}}\right)}{(z^{\mu})} \frac{dz}{V_{\text{sh}}}$$

$$= -\frac{f_0(E)\lambda b}{V_{\text{sh}}^2} \left[\int_a^b z^{1-\mu} dz - \alpha \int_a^b z^{-\mu} dz \right]$$

$$= -\frac{f_0(E)\lambda b}{V_{\text{sh}}^2} \left[\frac{1}{2-\mu} z^{2-\mu} \Big|_a^b - \alpha \frac{1}{1-\mu} z^{1-\mu} \Big|_a^b \right],$$

where, for brevity, we defined $a = \alpha + V_{sh}(t - t'')$ and $b = \alpha + V_{sh}(t - t_0)$. Then,

$$f(z, E, t) = -\frac{f_0(E)\lambda b}{V_{\text{sh}}^2} \left[\frac{1}{2-\mu} (\alpha + V_{\text{sh}}y)^{2-\mu} \Big|_{t-t_0}^{t-t''} - \frac{\alpha}{1-\mu} (\alpha + V_{\text{sh}}y)^{1-\mu} \Big|_{t-t_0}^{t-t''} = $$

$$= -\frac{f_0(E)\lambda b}{V_{\text{sh}}^2} \left[\frac{1}{2-\mu} (x - V_{\text{sh}}t + V_{\text{sh}}t - V_{\text{sh}}t')^{2-\mu} \Big|_{t_0}^{t''} + \right.$$

$$\left. - \frac{(x - V_{\text{sh}}t)}{1-\mu} (x - V_{\text{sh}}t + V_{\text{sh}}t - V_{\text{sh}}t')^{1-\mu} \Big|_{t_0}^{t''} \right]$$

This simplifies to

$$f(z, E, t) = -\frac{f_0(E)\lambda b}{V_{\text{sh}}^2} \left[\frac{1}{2-\mu} \left((x - V_{\text{sh}}t'')^{2-\mu} - (x - V_{\text{sh}}t_0)^{2-\mu} \right) + \right.$$

$$\left. - \left(\frac{x - V_{\text{sh}}t}{1-\mu} \right) \left((x - V_{\text{sh}}t'')^{1-\mu} - (x - V_{\text{sh}}t_0)^{1-\mu} \right) \right].$$

Under the hypothesis of $2 < \mu < 3$ (superdiffusion), if $t_0 = -\infty$, which corresponds to a shock starting very far away, the previous expression becomes

$$f(x,E,t) \simeq -\frac{f_0(E)\lambda b}{V_{\mathrm{sh}}^2}\left[\frac{1}{2-\mu}(x-V_{\mathrm{sh}}t'')^{2-\mu} - \frac{(x-V_{\mathrm{sh}}t)}{1-\mu}(x-V_{\mathrm{sh}}t'')^{1-\mu}\right]$$

since the terms containing t_0 have negative exponents. In as much as the propagator is a power law, $|x - x'| \gg k_\mu |t - t'|^{1/\mu - 1}$ (the shock-observer distance is just $|x - x'|$), both t'' and t' can reach t (the shock reaches the observer only when $t \to 0$). Thus, by setting $t'' = t$ we obtain

$$f(x,E,t) \simeq -\frac{f_0(E)\lambda b}{V_{\mathrm{sh}}^2}\left[\frac{1}{2-\mu}(x-V_{\mathrm{sh}}t)^{2-\mu}+\right.$$

$$\left.-\frac{1}{1-\mu}(x-V_{\mathrm{sh}}t)^{2-\mu}\right] = \frac{f_0(E)\lambda b}{\mu^2 - 3\mu + 2}\frac{(x-V_{\mathrm{sh}}t)^{2-\mu}}{V_{\mathrm{sh}}^2} \qquad (3.14)$$

Finally, considering that the observer is at $x = 0$,

$$f(0,E,t) \simeq \frac{f_0(E)\lambda b}{\mu^2 - 3\mu + 2} V_{\mathrm{sh}}^{-\mu}(-t)^{2-\mu} \propto \frac{1}{(-t)^\gamma} \qquad (3.15)$$

that is, far off the shock the time profile of the accelerated particles is a power law profile with slope $\gamma = \mu - 2$. Accordingly, an energetic particle profile with $0 < \gamma < 1$ implies superdiffusive transport with $\nu = (4-\mu)/2 = (2-\gamma)/2$, while $1 < \gamma < 2$ implies a non Gaussian propagator like that in Eq. (3.11) and a long–tailed distribution for jump lengths, but a diffusive transport with a mean square deviation growing linearly in time. It is clear from Eq. (3.14) that the power law slope does not change if the observer moves in the solar wind at constant speed, that is, $x = V_{\mathrm{sw}}t$.

Ballistic transport

Finally, in the case of a strictly ballistic transport, the propagator can be expressed in terms of δ functions as [97]

$$P(x-x',t-t') = \frac{1}{2}a[\delta(x-x'-v(t-t')) + \delta(x-x'+v(t-t'))], \quad (3.16)$$

where a is a constant with dimension $[1/t]$. The δ functions represent the fact that for scatter-free transport, $x - x' = \pm v(t - t')$, a propagation at constant

velocity away from the source on both sides occurs. By substituting Eq.
(3.16) above in Eq. (3.4), we obtain

$$f(x, E, t) = \frac{1}{2} f_0(E) a\lambda \int_{t_0}^{t''} [\delta(x - x' - v(t - t')) + \delta(x - x' + v(t - t'))] \times$$

$$\times \delta(x' - V_{\text{sh}} t') dx' dt'. \tag{3.17}$$

After straightforward calculations and variable changes, Eq. (3.17) reduces
to

$$f(x, E, t) = \frac{1}{2} f_0(E) a\lambda \left[\frac{1}{v - V_{sh}} \int_{u_0}^{u''} \delta(u) du - \frac{1}{v + V_{sh}} \int_{w_0}^{w''} \delta(w) dw \right] =$$

$$= \frac{1}{2} f_0(E) a\lambda \left(\frac{1}{v - V_{sh}} - \frac{1}{v + V_{sh}} \right) = f_0(E) a\lambda \frac{V_{sh}}{v^2 - V_{sh}^2}, \tag{3.18}$$

being $u = (x - vt) + (v - V_{sh})t'$ and $w = (x + vt) - (v + V_{sh})t'$. Then, the
particle time profile, in a given energy channel, is constant when particle
transport is scatter-free.

However, in the framework of continuous time random walk (CTRW) and
Lévy motions, ballistic transport is also described by the jump probability
$\psi(r, t) = A|r|^{-\mu} \delta(t - r/v)$ for $\mu < 2$. In such a case, for $\mu = 1.5$, the following
propagator is found [100]

$$P(x - x', t - t') \simeq \frac{a}{\pi (v^2(t - t')^2 - (x - x')^2)^{1/2}}. \tag{3.19}$$

This propagator exhibits a δ-like spike for $x - x' = v(t - t')$ and also a tail of
scattered particles for $x - x' < v(t - t')$. As an example of ballistic propaga-
tion, in Ref. [88] the solar impulsive event of 7 August 1999 is reported. The
electron time profiles coming from WIND observations show rapid and sym-
metric rise and decay indicating a free motion, indeed, scattering would tend
to create a slowly decaying tail. In addition, nearly "scatter-free" motion can
also be inferred by comparing the velocity of particles with the time delay
between electron injection in the corona and the onset time at WIND. By
comparing these temporal electron profiles with the propagator for ballistic
transport, it is possible to notice a strict resemblance [102] (see Fig. 3.4). In
the right panel of Fig. 3.4, the propagator is plotted as a function of the scal-
ing variable $\xi = r/vt$; when $\xi = 1$, that is $r = vt$, the propagator diverges,
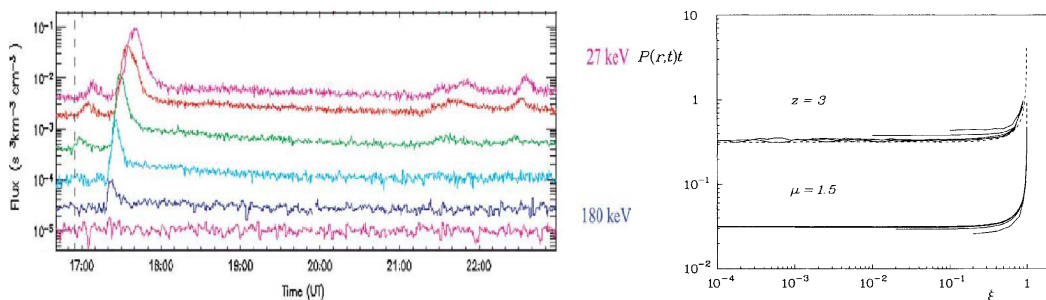
Figure 3.4: *Left panel*–Electron time profiles for the impulsive event of 7 August 1999 observed by WIND at 1 AU. Energies range between 27-300 keV (the blue label refers to the blue line at 180 keV).The vertical dashed line indicates the injection time at the Sun, the peak of the electron distribution is delayed of few minutes, each tick mark corresponding to $\simeq 9$ min (adapted from Ref. [88]). *Right panel*–Propagator for ballistic regime as a function of the dimensionless variable $\xi = r/vt$; note that time is increasing from the right to the left. The dashed line represents the analytical expression in Eq. (3.19), solid lines come from numerical simulations (adapted from Ref. [100]).

corresponding to the spike in the plot. This shape is well compared with the green and light-blue curves in the left panel in Fig. 3.4, then, electron time profiles in this event seem to recover the scatter-free propagator. The presence of a small tail of late particles in the electron time profiles could be probably due to the scattering undergone by some electrons while interacting with the turbulence in the interplanetary medium, although the majority of them moves fast enough to have $\langle r^2(t) \rangle \propto t^2$.

3.3 Data analysis

In order to study the spreading of particles accelerated at shock waves in the interplanetary medium, we have selected those datasets which agree with the hypothesis of a "local" acceleration at the shock, then, no particles coming from SEP events are present. In addition, the investigated shock events happened at large heliocentric distance where the assumption of an infinite planar shock wave can be considered reasonable [94, 95]. Here we present two main dataset analysis, concerning the Ulysses and Voyager 2 s/c. Other

datasets will be investigated in the future.

3.3.1 CIRs detected by the Ulysses spacecraft

Four repeated shock crossings observed by the Ulysses spacecraft in 1992–
1993 are analyzed. The heliocentric distance of Ulysses, after the Jupiter
encounter, was more than 5 AU, so the assumption of planar shock can be
considered a reasonable first approximation. From July 1992, Ulysses moved
into the fast solar wind from a newly developed coronal hole, which gave rise
to a long series of forward-reverse shock pairs associated with CIRs [103] (see
Fig. 3.5). We concentrate on the period from the beginning of 1992 (latitude
13° S) to late 1993 (latitude 41° S), because of the low influence of transient
events like SEPs, due to the decline in solar activity, so that the background
conditions remained relatively unperturbed (see Fig. 3.5). Conversely, the
sun was more active during the previous period, and this caused irregular
variations in the number of background particles which can be accelerated
at the shock. On the other hand, after 1993, no CIR shocks were observed
[103].

   Both electron and proton fluxes obtained from the CDAWeb service of
the National Space Science Data Center (cdaweb.gsfc.nasa.gov) are studied.
Particles are accelerated both at the forward and at the reverse shock of
the CIR, with clear enhancements associated with the shock fronts. The
energetic particle profiles extended several days before (after) the forward
(reverse) shock. We analyze the time profile at some distance from the shock
(close to the shock the propagator is Gaussian-like even for the case of Lèvy
walks, see Eq. (3.10)), looking for those events which exhibit long tails, either
in the proton or in the electron flux.

Electron transport

A first event is shown in Fig. 3.6, where the energetic particle fluxes are
displayed for the CIR shock event of January 19-22, 1993. Ulysses was at a
heliocentric distance of 5.01 AU and at a latitude of 25° S.

   From top to bottom, the panels show one hour averages for the plasma ra-
dial velocity and the plasma temperature from SWOOPS (PI D. McComas),
the proton fluxes measured by LEFS 60 of HI-SCALE (PI L. Lanzerotti) in
the energy channels 546–761 keV, 761–1223 keV, and 1.233–4.974 MeV, and
the electron fluxes measured by LEFS 60/ HI-SCALE in the energy chan-
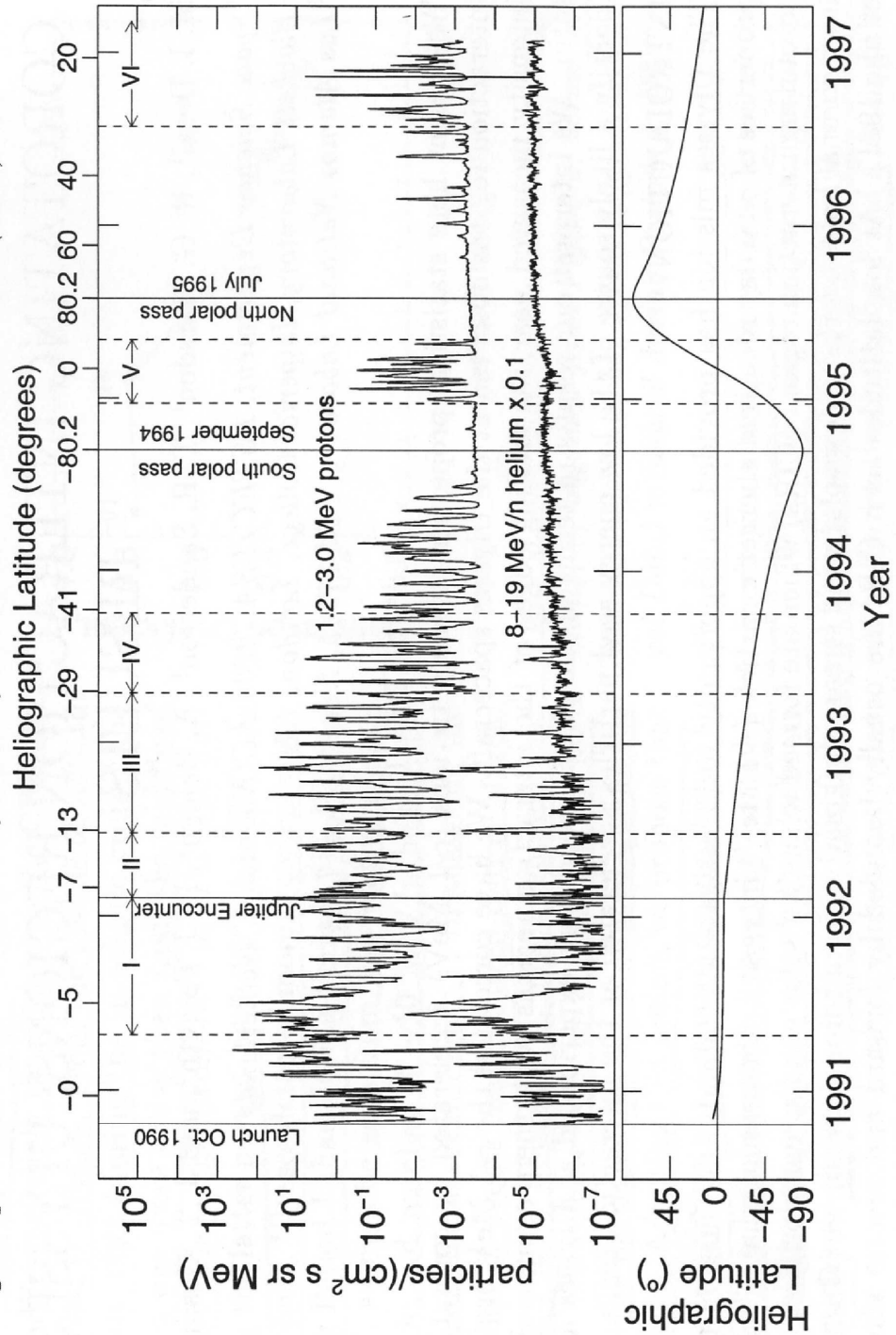
Figure 3.5: Daily averaged fluxes of protons and helium particles detected by the COSPIN/LET instrument on board Ulysses from the launch to 1997 (top panel). The temporal variation of the heliographic latitude of the spacecraft is also shown in the bottom (adapted from Ref. [104]).
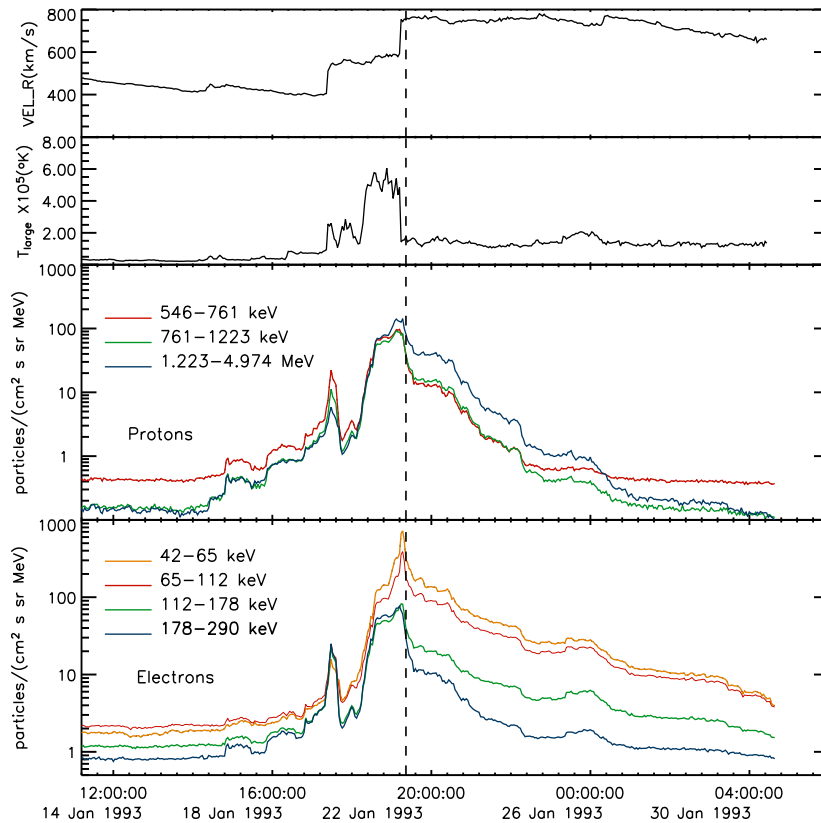
Figure 3.6: Plasma and energetic particle profiles for the Ulysses shock cross-
ing of 1993 January 22. From top to bottom, the panels show 1 hr averages for
the plasma radial velocity and the plasma temperature from SWOOPS (PI
D. McComas); proton fluxes measured by HI-SCALE LEFS 60 (PI L. Lanze-
rotti) in different energy channels; electron fluxes measured by HI-SCALE
LEFS 60 in different energy channels. The vertical dashed line indicates the
shock position. Note that each tick mark corresponds to 10 hr.

nels 42–65 keV, 65–112 keV, 112–178 keV, and 178–290 keV. In the semi-log plots, power law profiles are evidenced by lines which have upward concavity. In this case the particle profile is particularly broad after the reverse shock at 02:57 of January 22 (from about 10:00 of January 22 to 04:00 of January 31, 1993). It is possible to notice that the electron fluxes vary slightly more than one order of magnitude over about 200 hours and that several fluctuations with time scales of 20–30 hr are seen in these time profiles, as well as in the following events. As shown by Ref. [84], these irregularities in the energetic particle profiles are due to the low frequency magnetic turbulence, normally present in the solar wind. This turbulence has a correlation length λ of 3–5×10^6 km at 1 AU, which corresponds to time scales of 3–4 hr [105]. Ref. [106] analyzed the breakpoint frequency of magnetic fluctuations, which corresponds to the inverse of the correlation time, as a function of the heliocentric distance and of the latitude. The reported breakpoint frequencies at 4–5 AU correspond to correlation times in the range of 10–30 hr. Turbulence affects the magnetic connection between the spacecraft and shock, causing temporal changes in the energetic particle profiles with the corresponding time scales, as confirmed by the fact that these variations are seen at the same time in all energy channels, including those of protons. Further, the magnetic fluctuations cause the shock surface to be distorted and corrugated, with a corresponding variability in the acceleration efficiency along the shock surface [84].

To better appreciate the power law scaling, the energetic particle fluxes are plotted in log-log axes, considering the logarithm of the observation time t upstream of the shock minus the time of the shock crossing t_{sh}, i.e., $\log(|t - t_{\mathrm{sh}}|)$. The precise shock time is obtained from the Table of Ref. [103]. Fig. 3.7 displays the electron fluxes upstream of the reverse shock of 1993 January 22, and for the considered energy channels, with the dashed lines representing the corresponding power law fits. For clarity, not all of the fitting lines have been plotted. Considering that the energetic particle flux J is proportional to $f(x, E, t)$, we assume for the fit $J = A \, (\Delta t)^{-\gamma}$, with $\Delta t = |t - t_{\mathrm{sh}}|$. The fitted values of the slopes for each electron energy channel are given in Table 3.1. Values of χ^2_{pl} are also given and compared to those obtained, on the same time interval, by fitting the data with an exponential decay, $J = K \, e^{-\Delta t/\tau}$, expected for normal diffusion. Since the analyzed data are counting, it is possible to estimate an error for the y-axis values via a Poissonian statistics, that is, the error associated to energetic particle fluxes is given by $\sqrt{J}$. It can
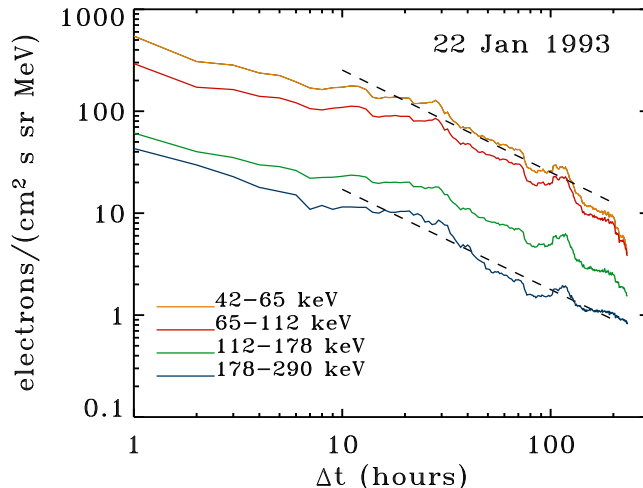
Figure 3.7: Electron fluxes upstream of the reverse shock of 1993 January 22 in log-log scale. Different colors refer to different energy channels. Dashed lines represent the power law best fits (not all shown for readability).

be seen that for the power law fit, χ^2_{pl} is much less than χ^2_{e} for the exponential decay for most energy channels. Note that the power law behavior is obtained over more than one decade in particle flux, and over almost 200 hr in time, so that the variations due to the turbulence do not appreciably influence the fit. For this event, values of $\gamma = 0.81$–0.98 imply $\mu = \gamma + 2 = 2.81$–2.98, that is superdiffusion with $\langle \Delta x^2 \rangle \sim t^{4-\mu} = t^{1.02}$–$t^{1.19}$. Although we cannot exclude the contribution of transport perpendicular to the magnetic field, we consider it smaller than the parallel transport, in agreement with Ref. [98] and with the results of recent numerical simulations [76].

A second event is shown in Fig. 3.8, where the energetic particle fluxes are reported for the CIR of 1993 May 10. Ulysses was at a heliocentric distance of 4.73 AU and a latitude of 30° S. Because of the high southern latitude only the reverse shock at 19:17 of May 10 was observed. The electron fluxes vary by one order of magnitude over about 70 hr. Also in this event, time variations in the profiles on the scale of 10–20 hr are seen, as above. The electron fluxes as a function of the time difference to the shocks are shown in Fig. 3.9 in log-log axes. A fit of the electron time profiles yields a power

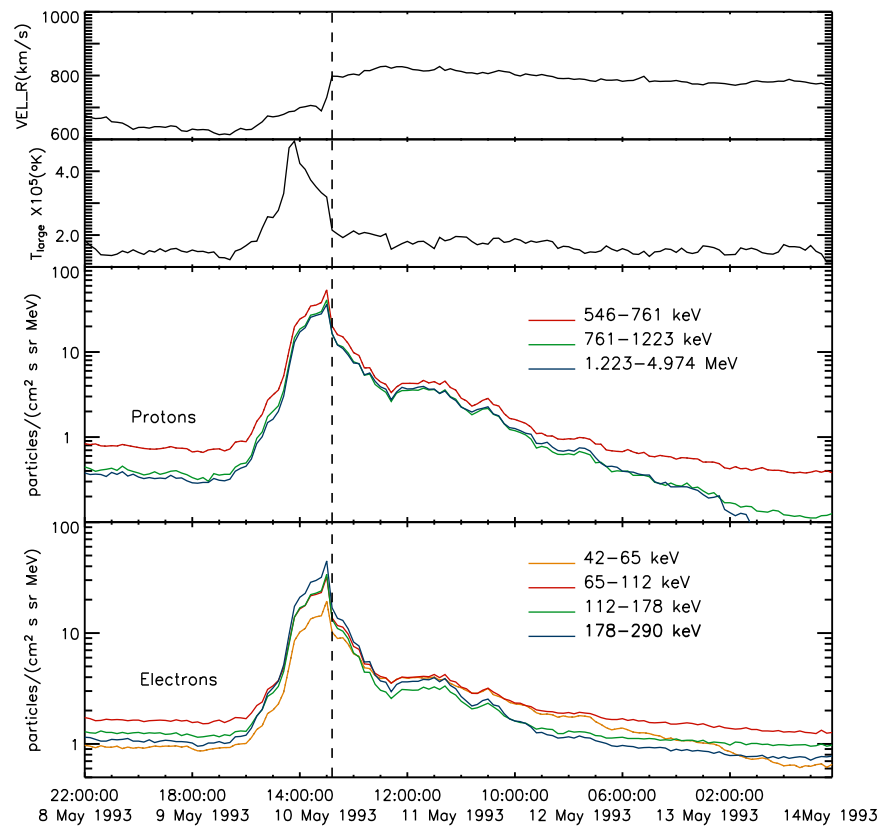Figure 3.8: Same as Fig. 3.6, but for the Ulysses shock crossing of 1993 May 10.
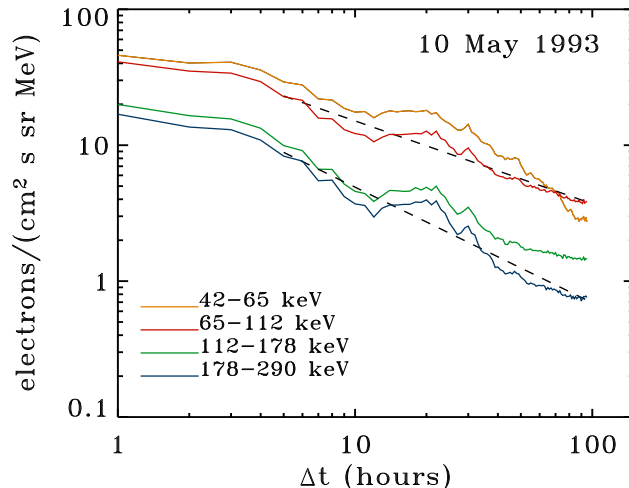
Figure 3.9: Electron fluxes in log-log axes for the Ulysses shock crossing of 1993 May 10. The different energy channels have been displaced by a factor $\sqrt{10}$ for clarity.

law index of $\gamma \simeq 0.62$–0.85 for the 65–112 keV, 112–178 keV and 178–290 keV energy channels (see Table 3.1), which also gives $\mu = 2.62$–2.85, and superdiffusion with $\langle \Delta x^2 \rangle \sim t^{1.15}$–$t^{1.38}$.

A third event is shown in Fig.s 3.10, 3.11, for the shock of 1992 January 10. The considered shock is reverse and the electron profile in the energy channel of 42–65 keV is well described by a power law with index $\gamma \simeq 0.60$ (see Table 3.1), leading to a distinctly superdiffusive behavior, that is $\langle \Delta x^2 \rangle \sim t^{1.4}$. On the other hand, we note that this event should be considered with some caution, because, as shown by Fig. 3.10, variations of the background are possible due to a non negligible level of solar activity at the beginning of 1992, or to other local effects, causing weak spikes in the energetic particle profiles.

The last event considered is shown in Fig.s 3.12 and 3.13, for the shock of 1992 October 11, detected at $\simeq 5$ AU. Power law fits in the tails of the electron temporal profiles give values of the scaling exponent $\gamma \simeq 0.30$–0.56 (see Table 3.1), implying $\mu = 2.30$–2.56, that is superdiffusion with $\langle \Delta x^2 \rangle \sim t^{1.44}$–$t^{1.70}$. This means that in the energy range 112-178 keV (see

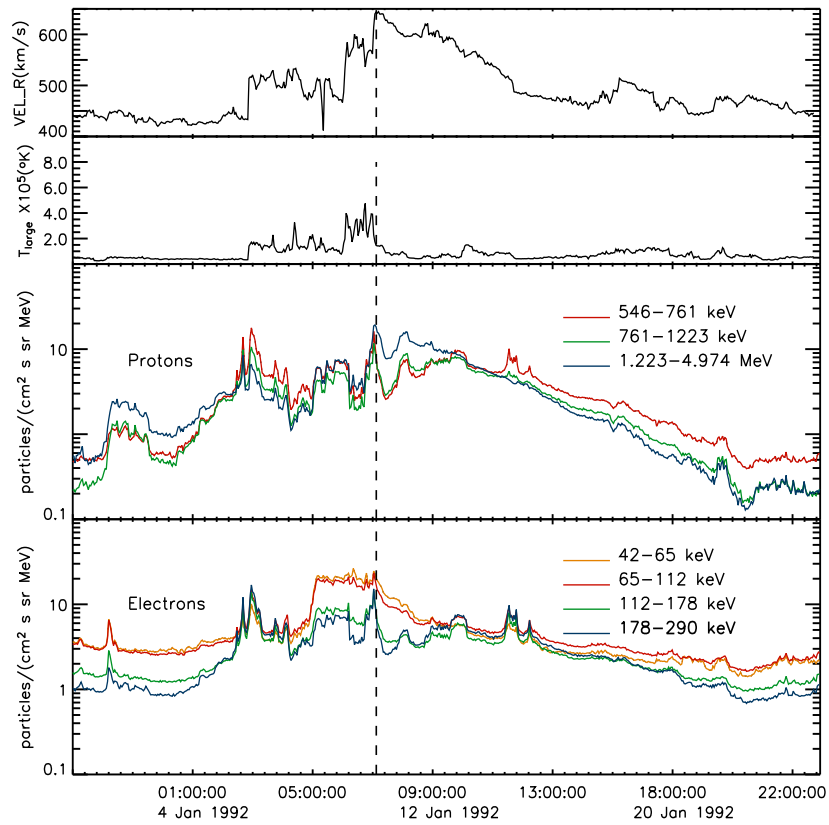Figure 3.10: Same as Fig. 3.6, but for the Ulysses shock crossing of 1992 January 10.
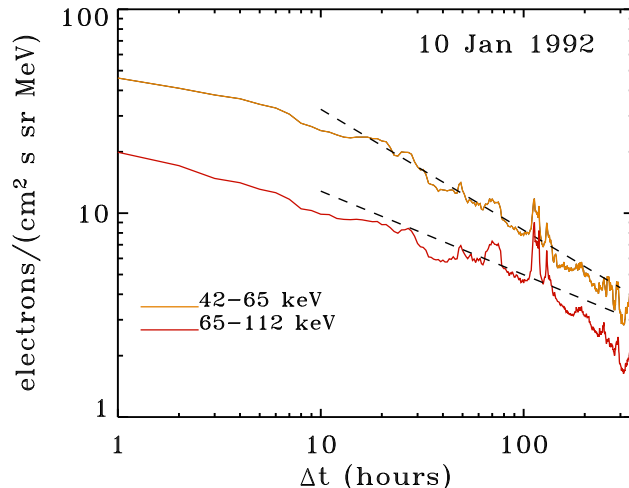
Figure 3.11: Electron fluxes in log-log axes for the Ulysses shock crossing of
1992 January 10. Energies as indicated.

Table 3.1) the transport is quasi-ballistic and particles travel trough the
interplanetary medium at nearly constant velocity. The reduced chi square
computation shows that a power law describes better the tail decaying over
almost 100 hr.

In this analysis some effects such as solar wind convection and adiabatic
deceleration [11, 107] have been neglected. About the former effect, it does
not influence the power law slope of the time profile, but only its duration.
This can be seen from Eq. (3.14) by setting $x = V_{sw}t$, with constant V_{sw},
rather than $x = 0$. Even if the observer moves with respect to the plasma
frame, the time slope does not change, but only the pre-factor. About the
latter effect, it causes a decrease in the intensity of particle fluxes with time,
so that far away from the shock the observed particle profiles are lower than
they would be based on propagation effects only. In Ref. [107] a typical time
for adiabatic deceleration has been estimated, being of $\tau_{AD} \simeq 1$ day at 1
AU. If we extrapolate this to 5 AU, considering that the characteristic time
for the adiabatic deceleration is proportional to the heliocentric distance, we
can expect a $\tau_{AD} \simeq 5$ days. This means that electron fluxes in Fig.s 3.7,
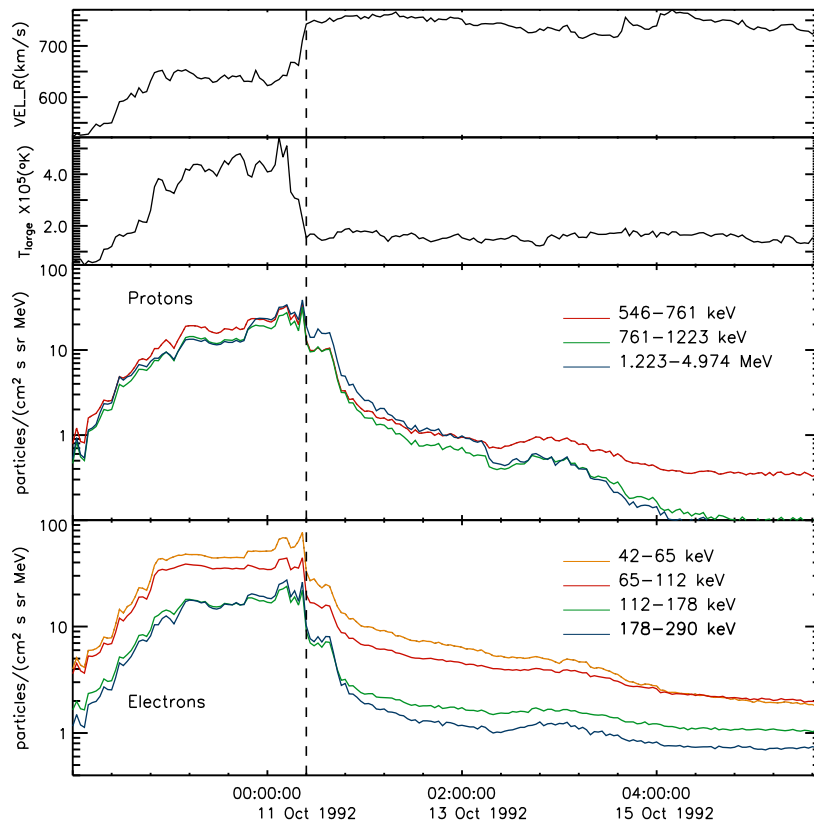3.9, 3.11, 3.13 could be stronger at 100-200 hr from the shock, leading to a

Figure 3.12: Same as Fig. 3.6, but for the Ulysses shock crossing of 1992 October 11.
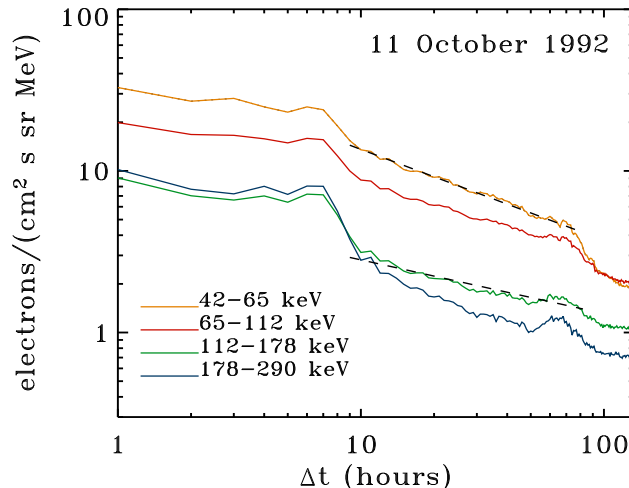
Figure 3.13: Electron fluxes in log-log axes upstream of the reverse shock of 1992 October 11.

smaller slope γ. In other words, a correction of the time profiles, by taking into account the effect of adiabatic deceleration, should lead to superdiffusion with larger values of $\nu = (2 - \gamma)/2$.

Proton transport

The same analysis has been performed for protons accelerated at CIR shocks. Three representative cases are displayed. Fig. 3.14 shows the proton time profiles in log-log axes during the forward shock crossing of 1992 September 12: it can be seen that the profiles become the steeper the longer Δt, so that power laws are not good fits for such cases (look at the results of the analysis reported in Table 3.2).

On the contrary, proton time profiles displayed in Fig. 3.15 exhibit a power law shape over roughly 100 hr in time but with an exponent γ ranging between 1.0–1.3, indicating that proton transport is at the "borderline" between normal diffusion and superdiffusion.

The third event analyzed is that of 1993 January 22, plotted in Fig. 3.16, where proton temporal profiles are better fitted by power laws (see the values of χ^2_{pl} in Table 3.2) even if the values of γ are greater than one. In such a

Table 3.1: Values of the parameters of the fits for the electron time profiles detected by Ulysses

DD/MM/YYYY	E (keV)	γ	2ν	χ^2_{pl}	$\tau(hr)$	χ^2_e
10/01/1992	42-65	0.60 ± 0.03	1.40	0.06	357 ± 19	0.15
	65-112	0.45 ± 0.03	1.55	0.18	455 ± 3	0.10
11/10/1992	42-65	0.56 ± 0.08	1.44	0.80	144 ± 20	3.20
	65-112	0.44 ± 0.09	1.56	0.40	190 ± 40	2.40
	112-178	0.3 ± 0.1	1.70	0.50	270 ± 130	1.40
	178-290	0.4 ± 0.2	1.60	1.00	202 ± 85	2.50
22/01/1993	42-65	1.00 ± 0.01	1.00	1.42	133 ± 2	1.76
	65-112	0.92 ± 0.02	1.08	0.90	152 ± 2	1.21
	112-178	0.81 ± 0.03	1.19	0.17	182 ± 8	0.33
	178-290	0.98 ± 0.05	1.02	0.11	152 ± 8	0.33
10/05/1993	42-65	0.71 ± 0.08	1.29	0.10	83 ± 11	0.03
	65-112	0.62 ± 0.07	1.38	0.03	112 ± 14	0.11
	112-178	0.69 ± 0.08	1.31	0.03	102 ± 14	0.15
	178-290	0.85 ± 0.08	1.15	0.07	77 ± 8	0.18

case proton transport is normal but the statistics of the random walk is in according to Lévy walk models [100].

The obtained time constant τ (see Tables 3.1 and 3.2) can give us a quick estimate of the scattering mean free paths. In the case of normal diffusion, the flux of energetic particles decreases as $J = K \exp[-(V_{\rm sh}/D_x)x]$, where $V_{\rm sh}$ is the upstream shock speed with respect to the solar wind rest frame, and D_x is the diffusion coefficient in the direction perpendicular to the shock. For the forward shock of 1992 September 12, reported in Table 3.2, $x = (V_{\rm sw}+V_{\rm sh})\Delta t$, so that [86]

$$\frac{1}{\tau} = \frac{V_{\rm sh}(V_{\rm sw} + V_{\rm sh})}{D_x}. \tag{3.20}$$

Disregarding transport perpendicular to the magnetic field, which under typical solar conditions is expected to be much smaller than the parallel transport [98, 76], the diffusion coefficient D_x can be expressed in terms of the diffusion coefficient parallel to the magnetic field as $D_x = D_{||} \cos^2 \psi$, being ψ the angle between the magnetic field and the radial direction [98]. Considering the standard relation between the mean free path $\lambda_{||}$ and the diffusion coefficient
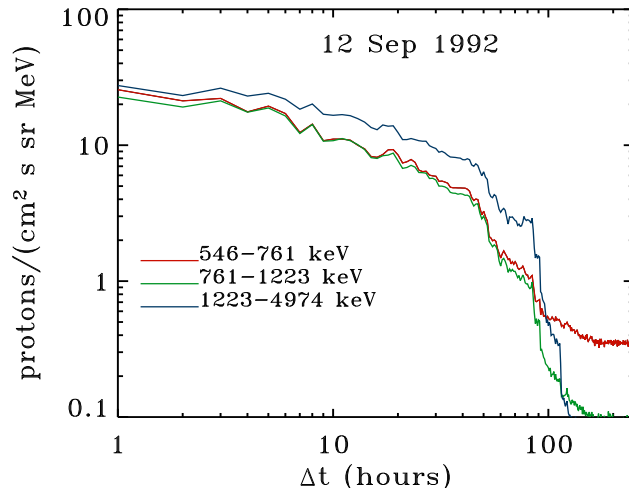
Figure 3.14: Proton fluxes in log-log axes for the Ulysses shock crossing of
1992 September 12. Energies as indicated.

$D_{||}$, $D_{||} = \lambda_{||} v/3$, Eq. (3.20) becomes

$$\lambda_{||} = \frac{3V_{\text{sh}}(V_{\text{sw}} + V_{\text{sh}})\tau}{v \cos^2 \psi} \tag{3.21}$$

Then, considering 1 MeV protons, velocities are $v \simeq 14000$ km/s, and as-
suming a solar wind speed $V_{\text{sw}} \simeq 400$ km/s, a shock speed $V_{\text{sh}} \simeq 200$ km/s,
a typical value of $\psi = 75°$ at 5 AU and, from Table 3.2, $\tau = 77$ hours, a
parallel mean free path $\lambda_{||} \simeq 0.7$ AU is obtained, which is much larger than
the so called Palmer consensus, i.e., $\lambda_{||} \simeq 0.1$ AU [89].

3.3.2 Shocks detected by Voyager 2

The analysis reported above has been also performed on ion temporal pro-
files detected by the Voyager 2 spacecraft after some shock crossing events,
including the TS crossing at the end of August 2007. Data used are hourly
and daily averages of energetic ion fluxes from the Low Energy Charged
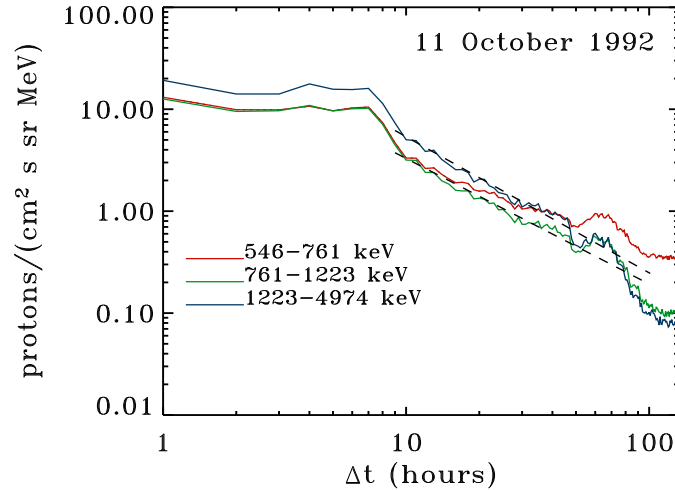Particle (LECP) instrument, which measures ion fluxes with energies > 30

Figure 3.15: Proton fluxes in log-log axes for the Ulysses shock crossing of 1992 October 11. Different colors refer to different energy channels.

keV and electrons fluxes with energies > 20 keV[3]. In particular ion fluxes for the eight energy channels PL01 (0.028–0.043 MeV), PL02 (0.043–0.080 MeV), PL03 (0.080–0.137 MeV), PL04 (0.137–0.215 MeV), PL05 (0.215–0.540 MeV), PL06 (0.540–0.990 MeV), PL07 (0.990–2.140 MeV), and PL08 (2.140–3.500 MeV) from the LECP experiment on board Voyager 2 satellite have been analyzed. The plasma data, that is plasma density, velocity, and temperature, are obtained from the Plasma Science (PLS) instrument.

CIR shock event at 6.7 **AU**

In Fig. 3.17 (bottom panel) temporal profiles are displayed in log-lin scale for the CIR forward shock event detected at 6.7 AU [108], while the upper panels show the proton thermal speed and the magnitude of proton speed versus time. At this heliocentric distance the approximation of the shock to an infinite planar structure can be considered valid. It is easy to notice that ion fluxes in different energy channels exhibit a different temporal behavior especially at some distance from the shock front. By plotting the tails of the

---

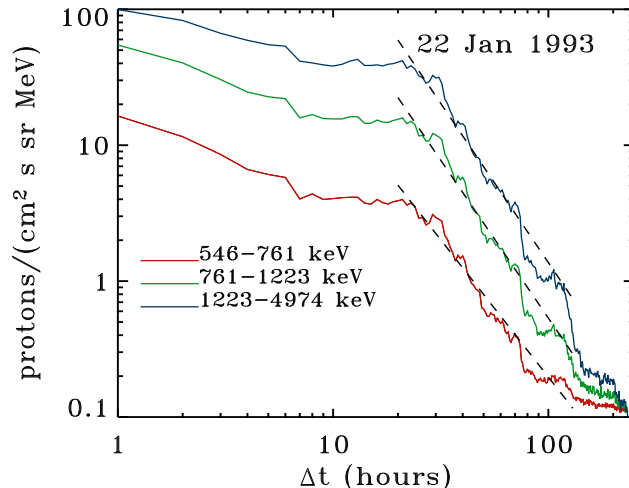[3]see sd-www.jhuapl.edu/VOYAGER/vgr_data_files.html

Figure 3.16: Proton fluxes in log-log axes for the Ulysses shock crossing of 1993 January 22. For clarity, energetic proton profiles have been separated by a multiplicative factor.

distributions in log-log scale (see Fig. 3.18), anomalous transport properties can be highlighted, indeed, profiles are power law in time with a scaling exponent $0 < \gamma < 1$. In this case power law fits have been performed on the energy channels 40-80 keV and 80-140 keV because the 30-40 keV energy channel is highly fluctuating, and this kind of analysis is not suitable. In the previous events that we analyzed[94, 95], a normal diffusive transport for protons and ions in the interplanetary space was found, implying that an exponential decay for the temporal particle profiles is expected [11, 98]. The data are fitted for nearly one decade and values of $\gamma = 0.87$, $\gamma = 0.92$ are found (see Table 3.3), corresponding to a mean square displacement growing faster than linearly in time, $\langle \Delta x^2(t) \rangle \sim t^{1.08} - t^{1.13}$. An estimation of the reduced chi-square both for the power law fit and for the exponential one indicates that a power law decay is definitely better for describing the temporal profiles in the tails (see Table 3.3). The relatively large value of χ^2 is due to the small number of data points and to the large scatter of them. This event shows that superdiffusion is possible for ions, too.
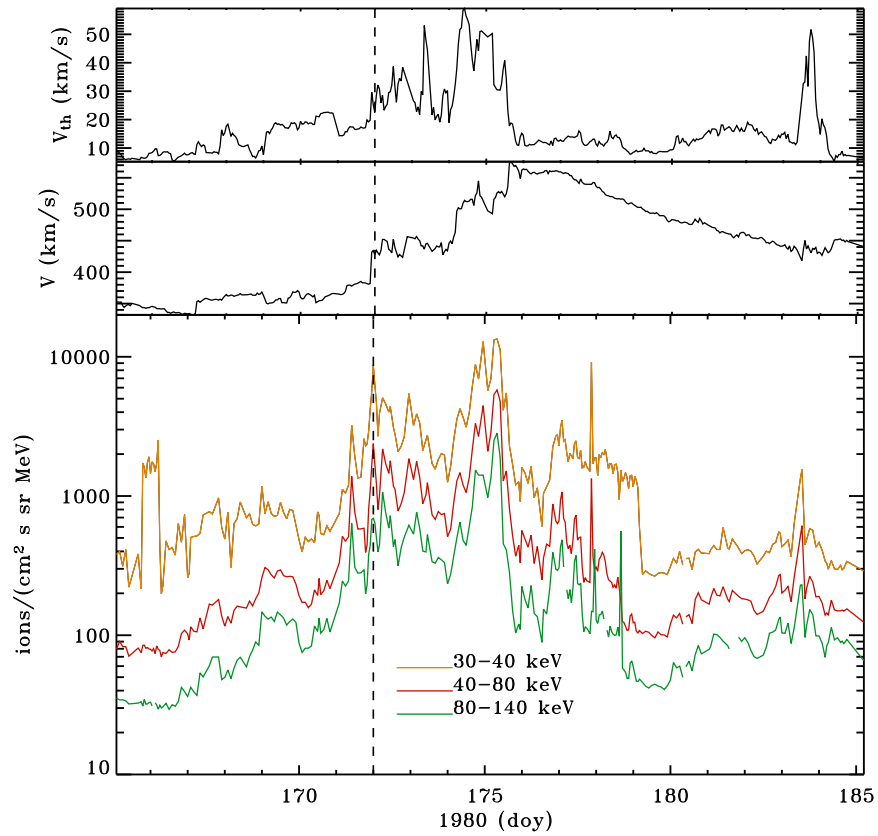
Figure 3.17: CIR shock detected by the Voyager 2 spacecraft at 6.7 AU. From top to bottom, the panels show 1 day averages for the proton thermal speed and the proton speed, measured by PLS (PI H. Bridge), and the ion fluxes measured by LECP (PI S. Krimigis) in the energy channels PL01, PL02 and PL03. The vertical dashed line indicates the position of the forward shock.

Table 3.2: Values of the parameters of the fits for the proton time profiles
detected by Ulysses

DD/MM/YYYY	E (keV)	γ	2ν	χ^2_{pl}	$\tau(hr)$	χ^2_e
12/09/1992	546-761	1.12 ± 0.09	1.0	0.26	67 ± 5	0.04
	761-1223	1.2 ± 0.1	1.0	0.28	63 ± 5	0.05
	1223-4974	0.97 ± 0.07	1.0	0.38	77 ± 5	0.1
11/10/1992	546-761	1.0 ± 0.2	1.0	0.53	57 ± 5	2.2
	761-1223	1.2 ± 0.3	1.0	0.49	44 ± 9	2.3
	1223-4972	1.3 ± 0.2	1.0	0.85	40 ± 6	3.7
22/01/1993	546-761	2.0 ± 0.1	1.0	0.09	57 ± 4	0.22
	761-1223	2.3 ± 0.1	1.0	0.14	47 ± 3	0.16
	1223-4974	2.33 ± 0.08	1.0	0.38	45 ± 2	0.38

The Termination shock crossing

Ion particle profiles have been studied also during a very recent period of
time of two years, from the beginning of 2006 to the end of 2007. In this
temporal interval Voyager 2, after a travel more than 30 years long, crossed
the TS at the boundary of the Solar System (at nearly 100 AU). In this
Section, we analyze data of particle time profiles from Voyager 2 in order to
explore the possibility of a superdiffusive transport for ions accelerated at
the solar wind TS.

The event is displayed in Fig. 3.19: the upper panels show the solar wind
velocity and the thermal speed, which allow to identify the shock event; in
the bottom panel, the PL05, PL06, PL07, and PL08 energy channels have
been plotted. Low energy channels have not been considered because they
are near the background level until 32 days before the TS crossing [109].
However, all energy channels are affected by a high level of background due
to high energy cosmic rays (especially particles with energies greater than
70 MeV) [109]. Indeed, at large distance from the Sun particle densities
are low, while the cosmic ray fluxes are relatively high due to the decreased
screening by the solar wind. Therefore, it has been necessary to perform
the statistical analysis by using background cleaned data. The background
level has been estimated as the lowest value of the signal in each energy
channel for the analyzed period; this procedure gives results in excellent
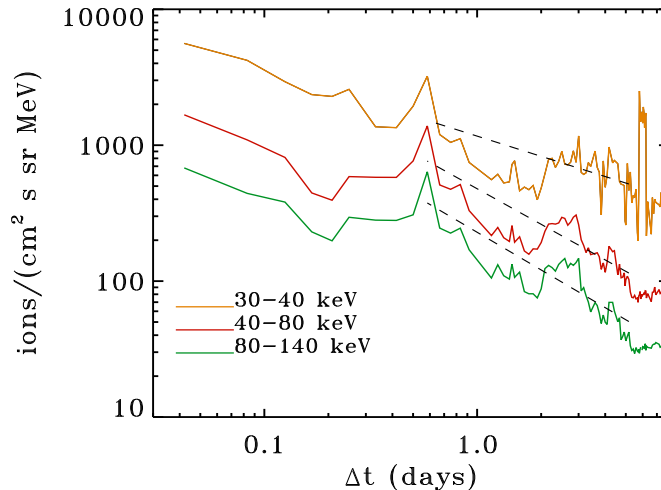agreement with background subtracted particle profiles published in [109],

Figure 3.18: Ion fluxes in log-log axes for the Voyager 2 shock crossing of 1980 June 20. Dashed lines represent the power law best fits.

and are also consistent with the background levels given in Ref. [110] for the Voyager 1 energy channels. In addition, in order to minimize the background contribution to the temporal particle profiles at some days from the shock front, data displayed in Fig. 3.19 have been filtered via a threshold method [111]: only the signal which is roughly equal or greater than 1.7 times the background level is retained, in other words the background correction has to be less than 60% of the signal for considering the data acceptable. This is a very severe filter, that allows to analyze data cleaned with a good level of accuracy.

After the background correction explained above, only PL06, PL07 and PL08 channels retain a number of points in the tails of the temporal profiles suitable for a statistical analysis. The filtered data and the corresponding fitting lines in log-log axes are shown in Fig. 3.20. Thus, by looking at the results of the fits shown in Table 3.3), we can see that for these energy channels, the reduced χ^2 indicates that the power law fits the tails of the ion profiles better than the exponential function, that is the transport for ions in those energy ranges is superdiffusive. The exponent of the power laws lies in the range $\gamma = 0.68$–0.71, leading to a mean square displacement
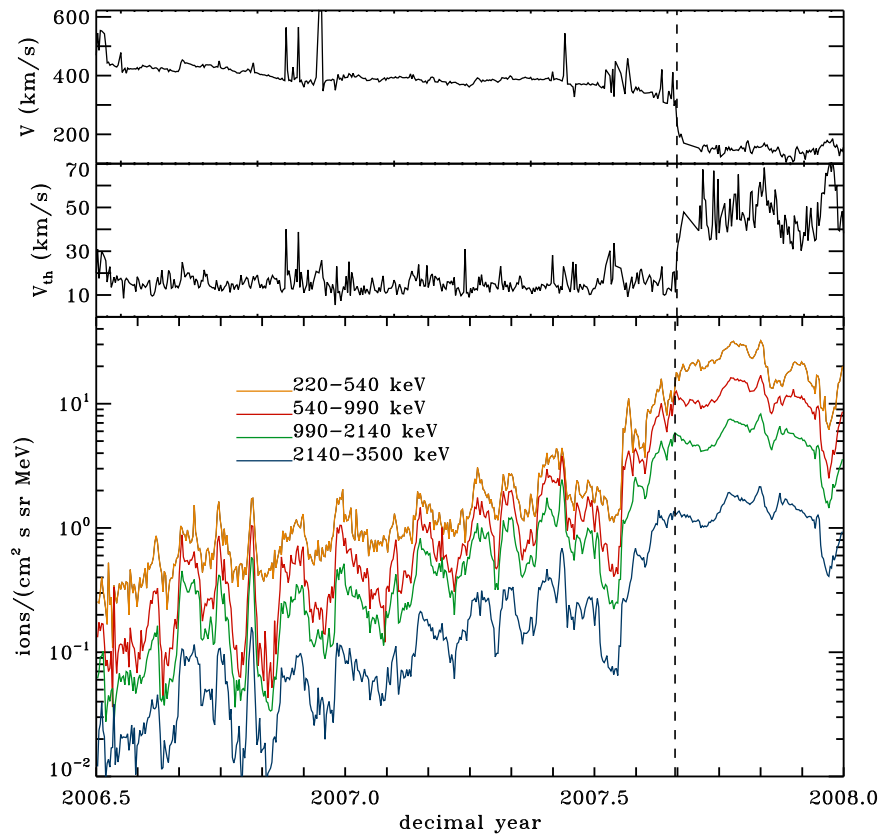
Figure 3.19: TS crossing at 85 AU by the Voyager 2 spacecraft. From top to bottom, the panels show 1 day averages for the proton speed and the proton thermal speed measured by PLS (PI H. Bridge), ion fluxes measured by LECP (PI S. Krimigis) in the energy channels PL05, PL06, PL07, PL08 after background subtraction. The vertical dashed line indicates the position of the shock.

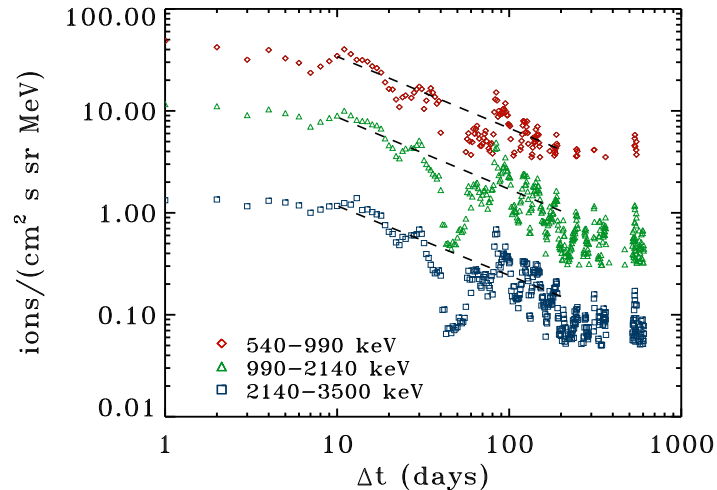$\langle \Delta x^2(t) \rangle \sim t^{1.29}-t^{1.32}$. Power law fits have been performed over a temporal

Figure 3.20: Same as Fig. 3.18 but for the TS event. Only data points for which the background correction is less than 60% of the signal have been plotted. The temporal profiles have been shifted by a factor ~ 3 for clarity.

interval of 200 days, starting from 10 days from the TS front. It is worth noticing that a recent study shown in Ref. [112] highlighted that the TS is expected to move at nearly constant speed in this period of time, then our model, which assumes a shock moving at constant velocity, is appropriated for these datasets.

3.4 Discussion

In agreement with the results of recent numerical simulations [27, 76] the analysis presented in this chapter shows that the propagation of energetic particles in the turbulent environment of the solar wind can be intermediate between diffusive and ballistic (or scatter-free), the latter being often deduced from SEP observations for electron propagation [88]. From the analysis of temporal fluxes of particles accelerated at CIR shocks detected by Ulysses, a difference in the transport regimes between electrons

Table 3.3: Values of the parameters of the fits for the ion time profiles detected by Voyager 2

DD/MM/YYYY	E (keV)	γ	2ν	χ^2_{pl}	χ^2_e
20/06/1980	40-80	0.87 ± 0.01	1.13	33.2	49.4
	80-140	0.92 ± 0.02	1.08	14.8	20.5
30/08/2007 (TS)	540-990	0.70 ± 0.07	1.30	0.22	0.40
	990-2140	0.71 ± 0.08	1.29	0.18	0.25
	2140-3500	0.68 ± 0.15	1.32	0.05	0.07

and protons has been found. One explanation of this evidence can be related to their different Larmor radii and of the consequent different resonant interaction with magnetic turbulence. At 5 AU, assuming a magnetic field $B = 2$ nT, the Larmor radii of the electrons at the analyzed energy channels range from 80 km to 360 km, while those of protons go from 56000 km to 125000 km. Magnetic turbulence in the solar wind exhibits a Kolmogorov-like spectrum, $\delta B^2(k) \simeq k^{-5/3}$, from the correlation length λ down to the dissipation scale λ_{diss}, which is usually assumed to be of the order of the thermal proton gyroradius ρ_{thp}. Considering a proton temperature $T_{\text{p}} = 10^5$ K, one has $\rho_{\text{thp}} \simeq 200$ km. The turbulence power at the wavelengths in resonance with energetic electrons is considerably weaker than that at the wavelengths in resonance with energetic protons. For instance, introducing the resonant wavenumber $k_{\text{e}} = 1/\rho_{\text{e}}$ ($k_{\text{p}} = 1/\rho_{\text{p}}$) for electrons (protons), we have $\delta B^2(k_{\text{e}})/\delta B^2(k_{\text{p}}) \sim (k_{\text{p}}/k_{\text{e}})^{5/3} \sim (\rho_{\text{e}}/\rho_{\text{p}})^{5/3} \sim 10^{-4}$. Although the electron rigidity is much smaller than the ion one, leading to faster pitch angle diffusion, if the electron gyroradius is below ρ_{thp}, i.e., in the dissipation range of magnetic turbulence, a very weak gyroresonant interaction is found (see Ref. [89]). In such a case, the electron propagation is nearly scatter-free and characterized by very long "jumps" in the parallel motion which lead to a superdiffusive behaviour. Ref. [76] have found a parallel superdiffusive transport, in the case of a low turbulence level, even when Larmor radii correspond to the turbulence correlation length. This could be interesting in the interpretation of the results coming from the analysis performed on temporal profiles of particles detected by the Voyager 2 spacecraft, indeed, for the two events under investigation, a superdiffusive transport has been found also for ions in several energy channels. Because of the large heliocentric distances, the level of magnetic turbulence upstream of the shocks

(that is in the unshocked solar wind) is going down, leading to a quasi-free streaming of particles accelerated at the shocks front.

These findings are likely to have a profound impact on the models of cosmic ray acceleration due to diffusive shock acceleration, as well as on the analysis of energetic particle propagation throughout the heliosphere. Indeed, a lot of current research is concerned with acceleration models which depend either on parallel diffusion, or on perpendicular diffusion, or both, e.g. [77, 78]. Here we can see that, superdiffusive transport (parallel to the background magnetic field) has to be taken into account. Since superdiffusion allows a faster escape of particles from the shock region, the efficiency of the DSA could be decreased. Early attempts to take into account non Gaussian transport in cosmic ray shock acceleration have been carried out by Ref. [113] for the subdiffusive case and by Ref. [114] for both anomalous regimes.

The hypothesis of a superdiffusive transport for energetic particles could be intriguing for explaining Voyager 1 and Voyager 2 observations of anomalous cosmic rays (ACRs) during the TS crossings. ACRs represent a population of interstellar neutral atoms ionized and picked up by the solar wind; the standard scenario expects that, once convected by the plasma to the TS, ACRs are here accelerated up to 100–200 MeV by DSA. However, by studying the daily-averaged particle intensity profiles, Ref.s [116] and [117] observed a continuous increase of particle intensities after the TS crossing instead of a "peak" of energetic particles at the shock front. This means that these particles are not accelerated at the TS front. For this reason, several new acceleration models have been proposed (see Ref. [111] and references therein). Assuming a superdiffusive motion, which allows a faster escape of particles from the shock region, the peak of energetic particles around the shock front could be missed. In addition, the spectral index coming from spectra of suprathermal ions detected by Voyager 2 in the heliosheath region is inconsistent with that predicted by the standard DSA theory [109], this could be due to some theoretical assumptions, such as the isotropy of particle distribution functions and the diffusive propagation, which are not supported by spacecraft observations.

Another puzzling subject in space physics is the interpretation of the time profiles of SEPs. Part of the difficulty comes from the fact that the time sequence of acceleration at flares and/or at the associated CME is not well understood [90] and part comes from the fact that transport is not easily studied in a medium where all parameters are changing with the heliocentric distance. Propagation models take into account effects on the transport prop-

erties such as the spatial and temporal variation of the source, the variation of acceleration efficiency along the shock surface, convection and adiabatic deceleration, the variation of the scattering mean free path $\lambda_\parallel$ with radial distance and particle rigidity [107, 86, 115]. Our results show that a further ingredient should be added to propagation models, that is superdiffusion. For example, even in the case of impulsive SEP events the decay phase of the SEPs time profile should be fitted with a modified Gaussian (see Eq. (3.10)), where the thickness of the distribution grows superlinearly with time, while the long time behavior of the propagator decays in time as $t^{1/(1-\mu)}$ with $3 < \mu < 2$, that is *faster* than the standard $t^{-1/2}$ scaling (see Eq. (3.5)). Thus, the possibility of superdiffusive transport represents a new tool for the interpretation of SEPs propagation as well as for the analysis of particles accelerated throughout the heliosphere.

Chapter 4

Turbulence in the heliosphere

4.1 General characteristics of turbulence in the interplanetary space

The interplanetary space is permeated by the solar wind, a continuous supersonic and superalfvènic flow of charged particles having solar origin and streaming away from the sun. From the second half of the last century, space missions allowed a large number of *in situ* observations, providing a rich description of the plasma state and dynamics. Solar wind is a natural laboratory for studying turbulence in collisionless, magnetized plasma because of the presence of strong magnetic fields and of the small collision mean free path, that approximates the Sun-Earth distance. Then, instead of a hydrodynamic approach [6], solar wind turbulence is well described by the magnetohydrodynamic (MHD) theory, even if the presence of a large number of characteristic space and temporal scales does not allow to have a sole theoretical framework enable to explain the different phenomena observed. What is well known is that solar wind presents a power law energy spectrum of magnetic field fluctuations extended over many frequency decades. In Fig. 4.1 power density spectra of magnetic field fluctuations observed by the Helios 2 spacecraft at various heliocentric distances are displayed. At frequencies below 10^{-4} Hz the spectra scale as roughly f^{-1}, this is the "energy injection" range due to the presence of large-scale structures in the solar wind, as stream interaction regions, shocks, and large-amplitude Alfvèn waves [118]. At higher frequencies power law shape changes and the slope becomes $f^{-5/3}$, that is the Kolmogorov spectrum: this range, named "inertial

range", describes the energy transfer from large scales up to the ion cyclotron frequency $f_{ci} = eB_0/m_i$. At frequency of $\simeq 0.1$ Hz there is a break in the power spectrum, beyond which the slope increases with variations ranging from f^{-2} to f^{-5} [119, 120, 121]. It is still unclear the origin of this slope increase in the power spectrum: some authors argue that it could be associated to the dissipation of magnetic energy via particle-wave interactions (kinetic processes) [120, 121, 7, 122], others suggest that another turbulent cascade, as in the inertial range, takes place [123, 124, 125]. Some evidences seem
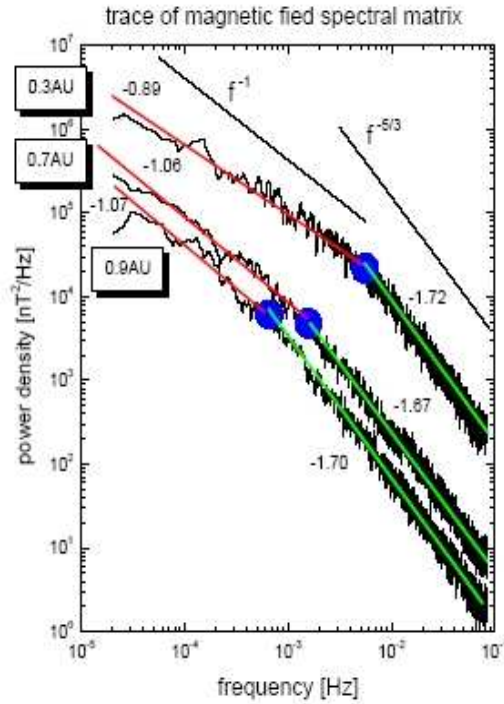

Figure 4.1: Magnetic field density power spectra as seen by the Helios 2 spacecraft at different heliocentric distances. The blue dots indicate the power break separating the energy injection range from the inertial range (adapted from Ref. [4]).

to disregard the hypothesis of a dissipation range, indeed, in the usual fluid turbulence the dissipation range is characterized by an exponential decay [5] and the magnetic fluctuations, after the spectral break, become Gaussian and

the coherent structures smoothed by dissipation. In the solar wind the non Gaussianity of magnetic fluctuations increases with frequency after the break (intermittency), as it happens in the low frequency inertial range [4, 125]; this could be an indication of a small-scale energy cascade.

While the solar wind represents a magnetized plasma freely evolving through the heliosphere, there are some regions of the interplanetary space in which plasma is confined by boundaries due to the presence of large-scale structures whose geometries have high influence on the plasma turbulence state. Examples are the Earth's Magnetosheath (MS) and the Earth's Foreshock (FS), the former is the region behind the bow shock where the solar wind (SW, hereafter) is slowed down and heated, the latter is a region of convected SW plasma, in which incoming particles are reflected and accelerated upstream by the Earth's bow shock. See Fig. 4.2 for a general overview. The MS is strongly influenced by the geometry of the bow shock with respect to the interplanetary magnetic field. Indeed, if the shock normal and the inter-
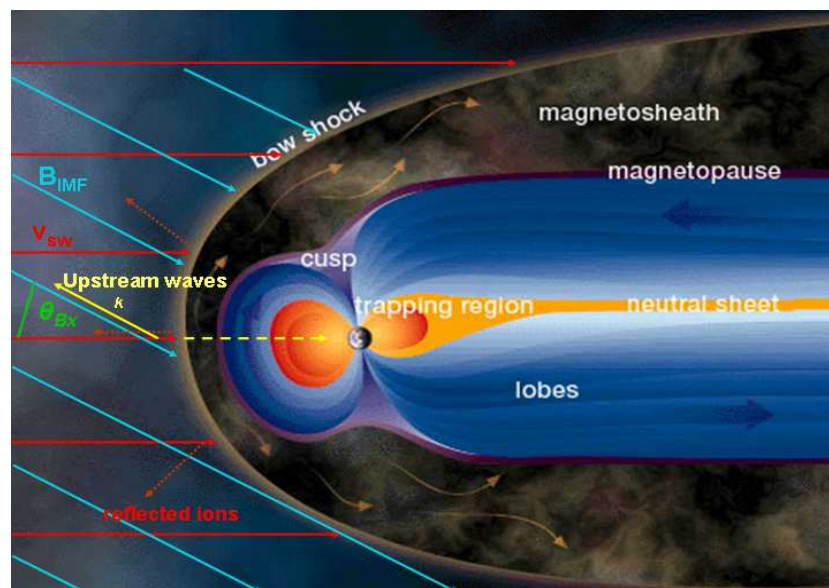

Figure 4.2: Cartoon of the Earth's magnetosphere and of the region of interaction between the solar wind flow and the magnetosphere, i.e., the bow shock region. Also the magnetosheath is displayed and the upstream side of the bow shock, where reflecting particles present give rise to the foreshock formation.

planetary magnetic field form an angle less than 45° (quasi-parallel shock), magnetic fluctuations convected by the SW are amplified ($\delta B/B_0 \simeq 1$, being B_0 the large-scale magnetic field intensity), making the region downstream of the bow shock highly turbulent; if the geometry is quasi-perpendicular (the angle between the shock normal and the interplanetary magnetic field is greater than 45°), the level of amplitude of magnetic fluctuations is much lower ($\delta B/B_0 \simeq 0.1$) [51]. The study of turbulence properties in such different regions is also important for better understanding plasma dynamics in other astrophysical contexts and in laboratory plasmas.

4.2 Turbulence anisotropy and Minimum Variance Analysis

As it is well known, magnetic field, convected by the SW plasma in the interplanetary space, is on average a spiral at very large scales, that is $\simeq 27$ days. However, going toward smaller and smaller scales, interplanetary magnetic field is characterized by fluctuations superimposed to the average large-scale field. From observations we know that these magnetic fluctuations have an extended power law spectrum (see discussion in Sec. 4.1) and their nature depends on the frequency range. For example, low frequency fluctuations (at frequencies lower than the ion-cyclotron frequency) are associated to incompressible large amplitude Alfvèn waves propagating away from the Sun [118], while the high frequencies part of the spectrum is related to more compressive modes [125].

Thanks to spacecraft observations, it was possible to perform statistical analysis on magnetic fluctuations at several scales and in different SW conditions in order to improve the knowledge on magnetic structures present in the interplanetary space. Ref. [118] showed that magnetic turbulence in the SW is anisotropic, that is there is a preferential direction, often associated to the mean magnetic field direction, along with the power of magnetic field fluctuations is small. Therefore, this direction presents a very low amplitude of fluctuations and is called "minimum variance" direction. Ref. [126] introduced the *minimum variance analysis* as a way to better evidence the anisotropy of fluctuations. This simple technique requires the determination of eigenvalues and eigenvectors of the one-point cross correlation matrix, de-

fined as

$$S_{ij} = \langle B_i B_j \rangle - \langle B_i \rangle \langle B_j \rangle \tag{4.1}$$

where i and j denote the components of the magnetic field $\mathbf{B}$ along the axes of a given reference system, and brackets means averages over a given time base. The background magnetic field $\mathbf{B}_0$ is calculated at the largest scale of duration T. By computing averages in Eq. (4.1) over different periods of increasing duration $\Delta t \ll T$, scaling properties of anisotropy can be investigated. Eigenvalues λ_i of the variance matrix, and in particular their ratios, determine statistical properties of anisotropy of magnetic fluctuations. Eigenvectors $\mathbf{b}$ give three unitary vectors forming the minimum variance reference system with one of the axis aligned with the direction along which the field has the smallest fluctuations [126]. This gives information on the spatial distribution of the fluctuations of the magnetic field vector.

In previous works the direction of minimum variance was found nearly aligned to the mean magnetic field. Indeed, Ref. [118], by using Mariner 5 data, found that the maximum variation of magnetic fluctuations is perpendicular to the ecliptic plane, while the minimum variance direction is parallel to the magnetic field; in addition, the values of the eigenvalues of the variance matrix computed are $\lambda_1 : \lambda_2 : \lambda_3 = 5 : 4 : 1$, where λ_1 is the eigenvalue along the maximum variance direction, λ_2 along the medium variance direction, and λ_3 the eigenvalue of minimum variance. Other systematic analysis of the one-point correlation matrix in Eq. (4.1) at frequencies below the ion-cyclotron frequency highlighted that one of the eigenvalues is always much smaller than the others, that is $\lambda_3 << \lambda_2 \leq \lambda_1$, and the minimum variance is roughly aligned to the magnetic field [127, 128, 129] with just a small amplitude spread of $10°$ [3, 4]. This implies that magnetic turbulence is approximately two-dimensional. In the plane perpendicular to the direction of minimum variance, say b_3, turbulence remains weakly anisotropic. Typical global values, frequently reported in literature, are $\lambda_1 : \lambda_2 : \lambda_3 = 10 : 3.5 : 1.2$ [4]. Such kind of observations may be due to the predominance in the analyzed frequency ranges of Alfvènic fluctuations. In Ref. [130] the minimum variance matrix has been expressed as a function of two scalar quantities: the magnetic energy density spectra $I^{[1]}(\boldsymbol{k})$ and $I^{[2]}(\boldsymbol{k})$ of the two allowed polarizations perpendicular to the mean magnetic field $\boldsymbol{B}_0$. The phenomenological expression given in Ref. [130] is

$$I^{[s]}(\boldsymbol{k}) = C^{[s]} \left[(\ell_x^{[s]} k_x)^2 + (\ell_y^{[s]} k_y)^2 + (\ell_z^{[s]} k_z)^2 \right]^{-1-\mu^{[s]}/2}, \tag{4.2}$$

where the index $s = 1, 2$ indicates the two polarizations, k_x, k_y and k_z are the cartesian components of the wave vector $\boldsymbol{k}$, $C^{[s]}$, $\ell_i^{[s]}$ and $\mu^{[s]}$ ($i = x, y, z$) are the free parameters of the model. Under the assumptions of statistical homogeneity and stationarity of the medium, and by considering the turbulent fluctuations, present in the solar wind, "frozen" in the flow (Taylor hypothesis) [4], the parameters in Eq. (4.2) were computed fitting the expressions for the eigenvalues of the variance matrix with the values found by Ref. [129] for the Helios 2 data at several temporal scales. This procedure highlighted that the polarization [1] is more energetic than the [2] one; $\ell_x^{[1]} > \ell_y^{[1]} >> \ell_z^{[1]}$, indicating that in the energy distribution of polarization [1], wave vectors parallel to $\boldsymbol{B}_0$ (z direction) dominate (quasi one-dimensional configuration); $\ell_x^{[2]} >> \ell_y^{[2]}, \ell_z^{[2]}$, indicating that the spectrum $I^{[2]}(\boldsymbol{k})$ is flat (quasi two-dimensional configuration). Therefore, for each temporal scale it has been possible to calculate unambiguously eigenvalues of the variance matrix, as well as the sum $\lambda_1 + \lambda_2 + \lambda_3$, and consequently well defined magnetic field power spectra.

In a more recent work described in Ref. [131], a study of anisotropy was performed by analyzing ACE observations at 1 AU, spanning both the inertial (up to 0.1 Hz) and the dissipation range of the turbulence spectrum (from 0.3 to 0.8 Hz). Data enclose fast, slow streams and magnetic clouds, in order to characterize turbulence in various physical regimes. One of the main results is that magnetic fluctuations are less transverse to the mean field in the high frequency range than in the inertial range in all datasets under analysis, implying that the nature of fluctuations changes above the ion-cyclotron frequency.

In this chapter, via a statistical analysis, it will be shown that, in the high frequency range of the magnetic field power spectrum, a wide power-law distribution of eigenvalues of the variance matrix is found, which implies that it is not possible to obtain characteristic values for λ_i and, consequently, unambiguous information on the power spectrum, as done in the previous works mentioned. Indeed, in this case very high standard deviations are found to be associate to mean values of the eigenvalues.

---

[4]Owing to the superalfvènic speed of the solar wind, fluctuations, having velocities much smaller than the wind speed, can be considered in first approximation "frozen" in the flow, allowing to pass from temporal variations to spatial variations via the relation, $\delta r = V \delta t$, with V the solar wind speed. This is useful when observations from only one satellite are available.

4.3 Characterization of anisotropy via eigenvalues of the variance matrix

In the present work statistical properties of eigenvalues and eigenvectors of the variance matrix are investigated, by using magnetic field time variation measurements by the Cluster spacecraft [5] behind the Earth's quasi parallel bow shock. In particular, three different datasets have been used, namely in the period during which the four spacecraft were orbiting in the SW, in a second period in the FS and in a third in the MS. These regions are characterized by different spatial and temporal characteristic scales and locally by different plasma parameters. As discussed in Sec. 4.1, for a quasi-parallel geometry of the bow shock the magnetic field and plasma fluctuations are intensified in magnitude, so that the MS is one of the most turbulent plasma environments in the near Earth space. The minimum variance analysis gives information about the power spectra of the three components of the magnetic field and is appropriate for characterizing magnetic turbulence in these regions. Indeed, the aim of this work is to study statistical features of eigenvalues and eigenvectors of the variance matrix for investigating anisotropy of magnetic turbulence above and below the ion-cyclotron frequency.

On April 16th, 2003, Cluster crossed the FS, afterwards it was in the SW and subsequently, after the bow shock crossing, entered the turbulent MS. The plasma beta, i.e., the ratio between plasma and magnetic pressure, is close to unity in the FS and in the pure SW (about $\beta \simeq 1.1$ and $\beta \simeq 1.6$, respectively), while it is very high in the MS ($\beta \simeq 15$). The magnetic field data were sampled at a frequency $\Delta f = 22$ Hz ($\Delta t = 0.04$ sec) by the Fluxgate magnetometer (FGM) on board the Cluster spacecraft [132]. This is a high frequency sampling rate compared with the ion-cyclotron frequency, which is close to $\Delta t_{ic} \simeq 10$ sec both in the SW and in the FS, and $\Delta t_{ic} \simeq 5$ sec in the MS. For the purpose of this work, the data were transferred in a reference frame defined by the bow shock model, where the X axis is directed along the bow shock normal, Y is in the plane defined by the SW velocity and the X direction, and Z completes the frame. From the time series the variance

---

[5]The Cluster mission is devoted to study the SW, the Earth's magnetosphere and the bow shock region, allowing to investigate space regions with different turbulence properties. It is formed by 4 identical spacecraft flying in a tetrahedral configuration in order to have a 3D overview. Satellites can resolve small-scale plasma structures both in space and time with an unprecedented accuracy.

matrix at different scales is computed. Thus, for each time series of duration T and for each spacecraft $s = \{1, 2, 3, 4\}$, the variance matrices are computed on running windows of variable length $\Delta t_n = 2^n / \Delta f$ ($n = 0, 1, \ldots, 13$ being the scale index), centered on the time t_l ($l = 1, 2, \ldots, T - \Delta t_n$ being the window index)

$$S_{ij}^{(s)}(\Delta t_n, t_l) = \langle B_i^{(s)}(t) B_j^{(s)}(t) \rangle - \langle B_i^{(s)}(t) \rangle \langle B_j^{(s)}(t) \rangle . \qquad (4.3)$$

Eigenvalues $\lambda_i^{(s)}(\Delta t_n, t_l)$ and eigenvectors $b_i^{(s)}(\Delta t_n, t_l)$ are then obtained, as well as the angle $\theta^{(s)}(\Delta t_n, t_l)$ between the background magnetic field and the local minimum variance direction $b_3^{(s)}(\Delta t_n, t_l)$.

This study is devoted to describe the properties of turbulence as a function of frequency ranges, therefore hereafter the term "large-scale" refers to time variations below the ion-cyclotron frequency, and "small-scale" to time variations above the ion-cyclotron frequency.

In Fig.s 4.3, 4.4 and 4.5 we show, for Cluster-1, the time evolution of the eigenvalues $\lambda_i^{(s)}(\Delta t_n, t_l)$ of the variance matrix for three different scales Δt_n, crossing the ion-cyclotron characteristic scale, and for the three regions under analysis. It is interesting to notice that, while at large-scales eigenvalues have smooth variations, the behavior completely changes below the ion-cyclotron scale (high frequencies). In this frequency region the eigenvalues of the variance matrix are usually low, but large amplitude fluctuations, highly localized in time, appear (intermittent character). This is evident for all spacecraft in each region investigated, so that it represents a typical characteristic of small-scale magnetic turbulence. It is worth noting that the intermittency found at small-scales does not necessarily coincide with the presence of small-scale strong intermittent structures which have been recently reported in literature [125].

In order to better describe the change of the gross statistical properties of the anisotropy with the scale, we now investigate the scaling behavior of the relevant Probability Density Functions (PDF) of the eigenvalues of the variance matrix. Therefore, the whole range of values of $\lambda_i^{(s)}(\Delta t_n, t_l)$ has been divided in discrete bins, and the probability of occurrence $p(\lambda_i^{(s)})$ within the m-th bin has been calculated. In Fig. 4.6 the PDFs of the eigenvalues of the variance matrix calculated at different scales Δt_n in the SW are displayed. At a glance, there is a very weak statistical dependence on the single spacecraft, especially at larger scales; thus, the four spacecraft can be considered as four different ensembles of the same phenomenon in a given region, at least as far
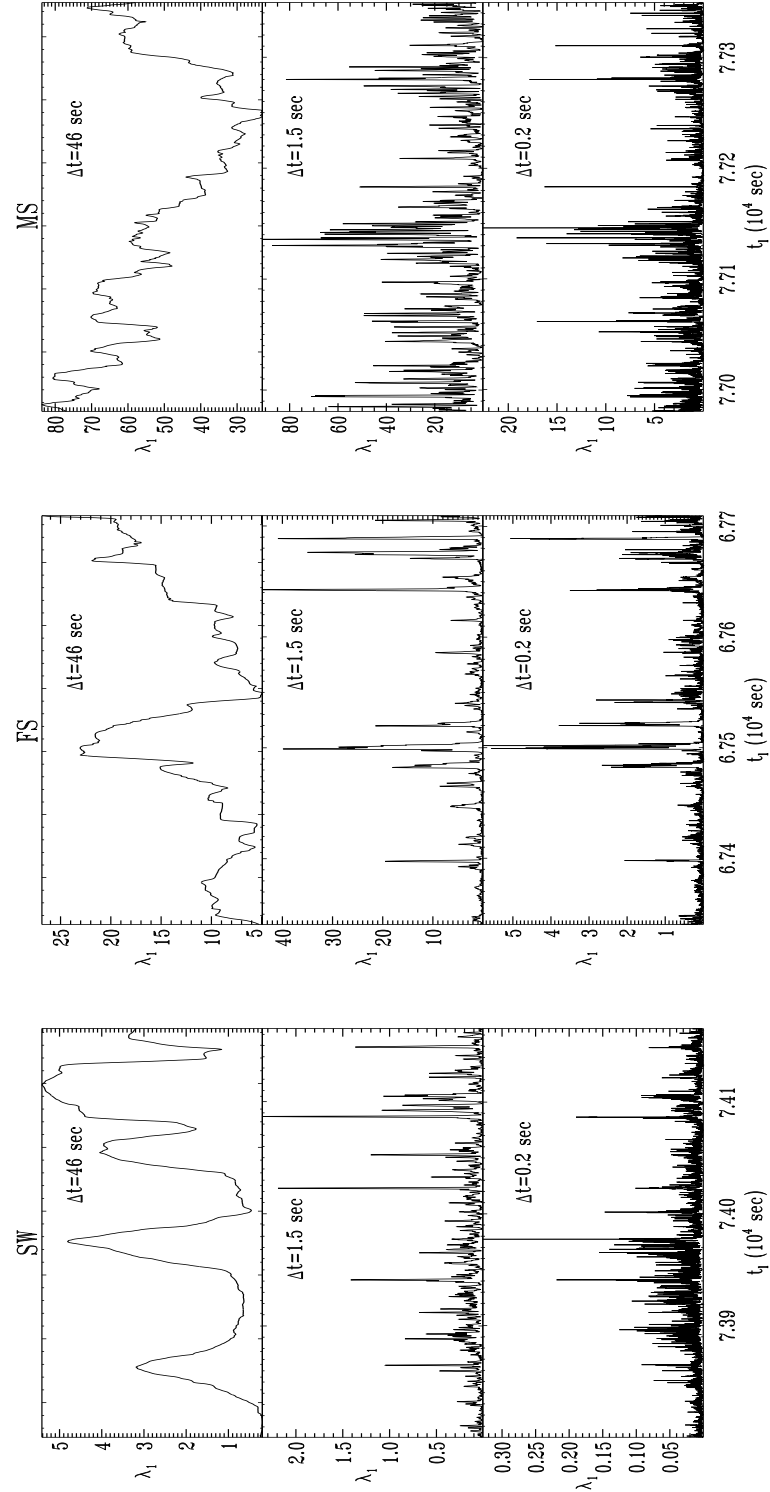
Figure 4.3: Amplitude of the eigenvalue along the maximum variance direction as a function of time at three scales in the SW (on the left), in the FS (in the middle) and in the MS (on the right). It is interesting to notice the burst-like behavior at the smallest scales, implying an high level of dispersion in the λ_1 values. Note that in the MS the level of magnetic fluctuations is higher than in the other two regions of the heliosphere.
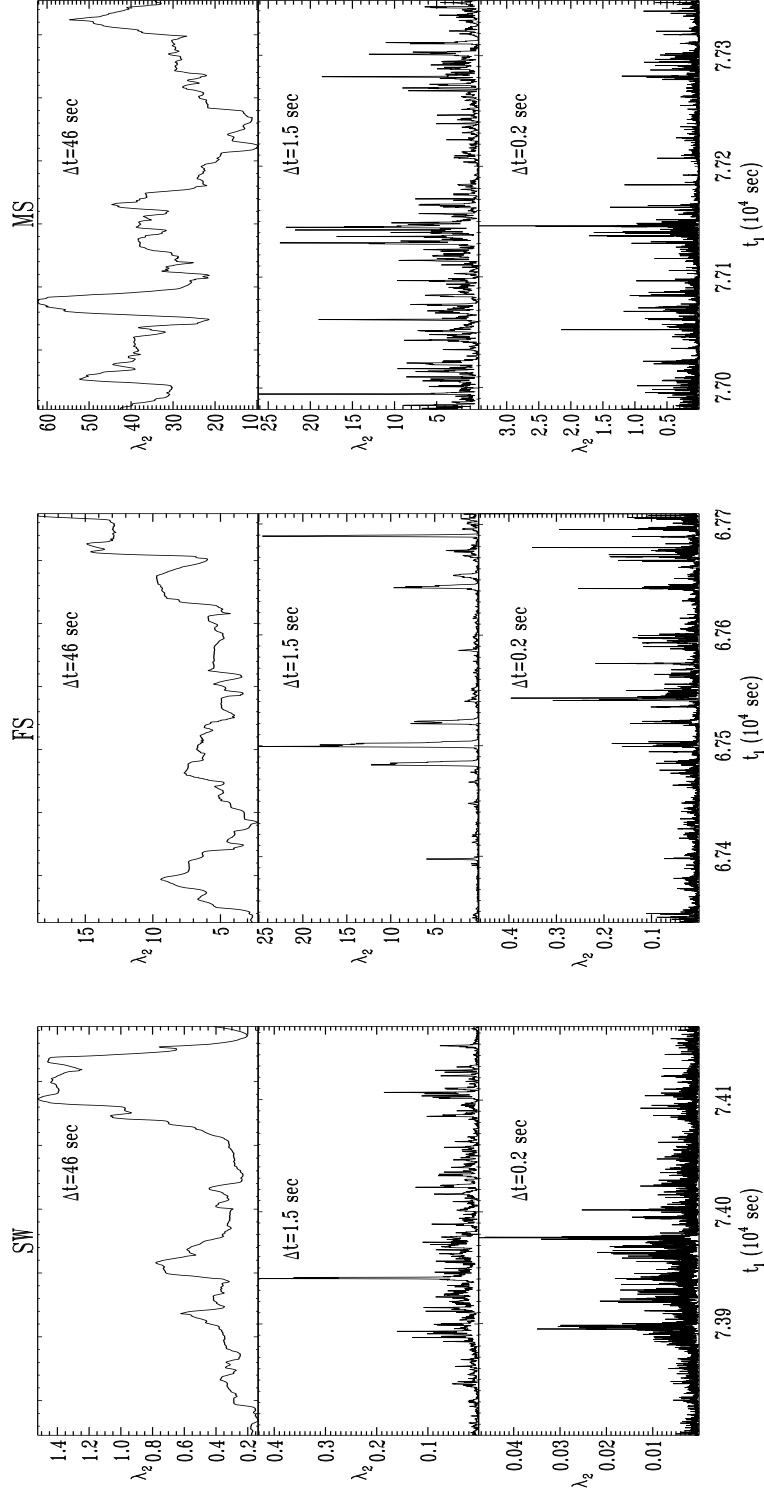
Figure 4.4: Same as Fig. 4.3 but for the eigenvalue of medium variance.
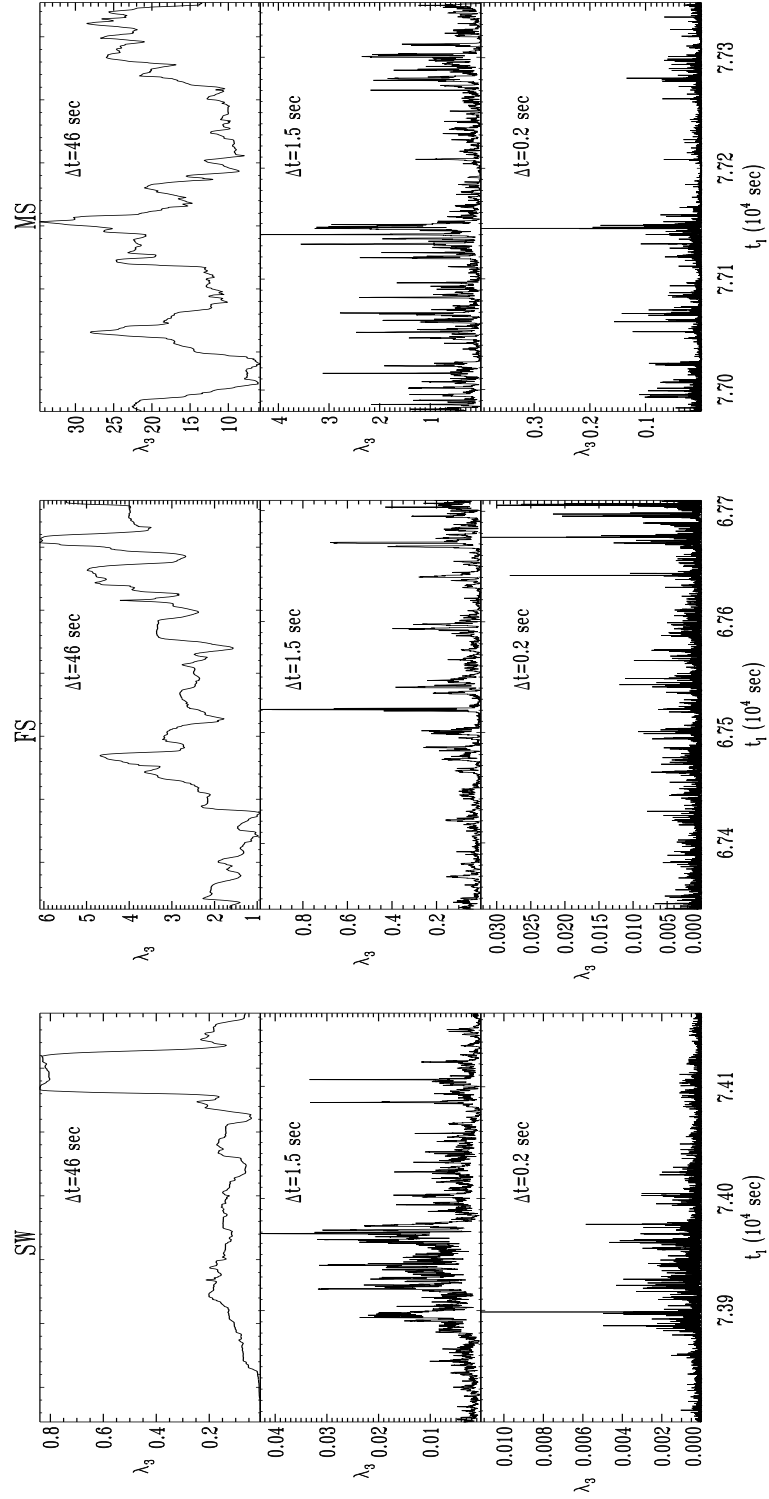
Figure 4.5: Same as Fig. 4.3 but for the eigenvalue of minimum variance.

as our analysis is concerned. Therefore, in the following a combined dataset, obtained joining together the four Cluster satellites datasets, will be used for investigating variations in statistical properties of anisotropy as a function of frequency.

In Fig. 4.7 the PDFs $p(\lambda_i)$ of the eigenvalues of the variance matrix $\lambda_i(\Delta t_n, t_l)$ in the three different zones of the heliosphere are compared. A variation with the scale, already visible for Cluster-1 data in the SW (see Fig. 4.6), is observed for all zones, that is, while at large-scales PDFs are roughly peaked around a given value, as the scales cross the ion-cyclotron frequency, the PDFs evolve toward a broader, power law behavior. To our knowledge this scale-dependence has never been evidenced. In addition, note that in the Earth's MS the eigenvalues are larger in amplitude by more than one order of magnitude than in the SW. This is consistent with the presence of an high level of magnetic fluctuations in this region of the near Earth's space. The important point here is that below the ion-cyclotron scale the burst-like temporal behavior of the eigenvalues is reflected in the power law distribution of λ_i, which implies the absence of a given characteristic value. In this frequency range it is not possible to compute an average value for the eigenvalues of the variance matrix because the presence of a power law distribution indicates a sort of multi-scale dynamics.

In order to characterize the degree of anisotropy of magnetic fluctuations, a statistical study of the ratios λ_3/λ_1 and λ_2/λ_1 is performed. In Fig. 4.8, the time behavior of the ratios in the SW at scale $\Delta t = 46$ sec is displayed. We used, as an example, the Cluster-1 data. The nature of anisotropy seems to be noticeable variable in time, for example, in the period from 73820 sec to 73860 sec a well defined minimum variance direction is observed, while the maximum variance and the medium variance directions are comparable (their ratio is close to 1). This is the standard situation in which magnetic fluctuations are confined in a plane roughly perpendicular to the minimum variance direction and the geometry is quasi bidimensional. Such a situation is often associated in literature to Alfvèn waves propagating away from the sun [118]. On the other hand, just after this temporal interval both ratios become almost zero, indicating that magnetic fluctuations exhibit large amplitude values along the maximum variance direction (quasi 1D geometry), and so on. Thus, the degree of anisotropy strongly depends on the presence of specific structures at each time interval.

The PDFs of the ratios between the minimum and the maximum eigenvalue, and between the intermediate and the maximum eigenvalue, calculated
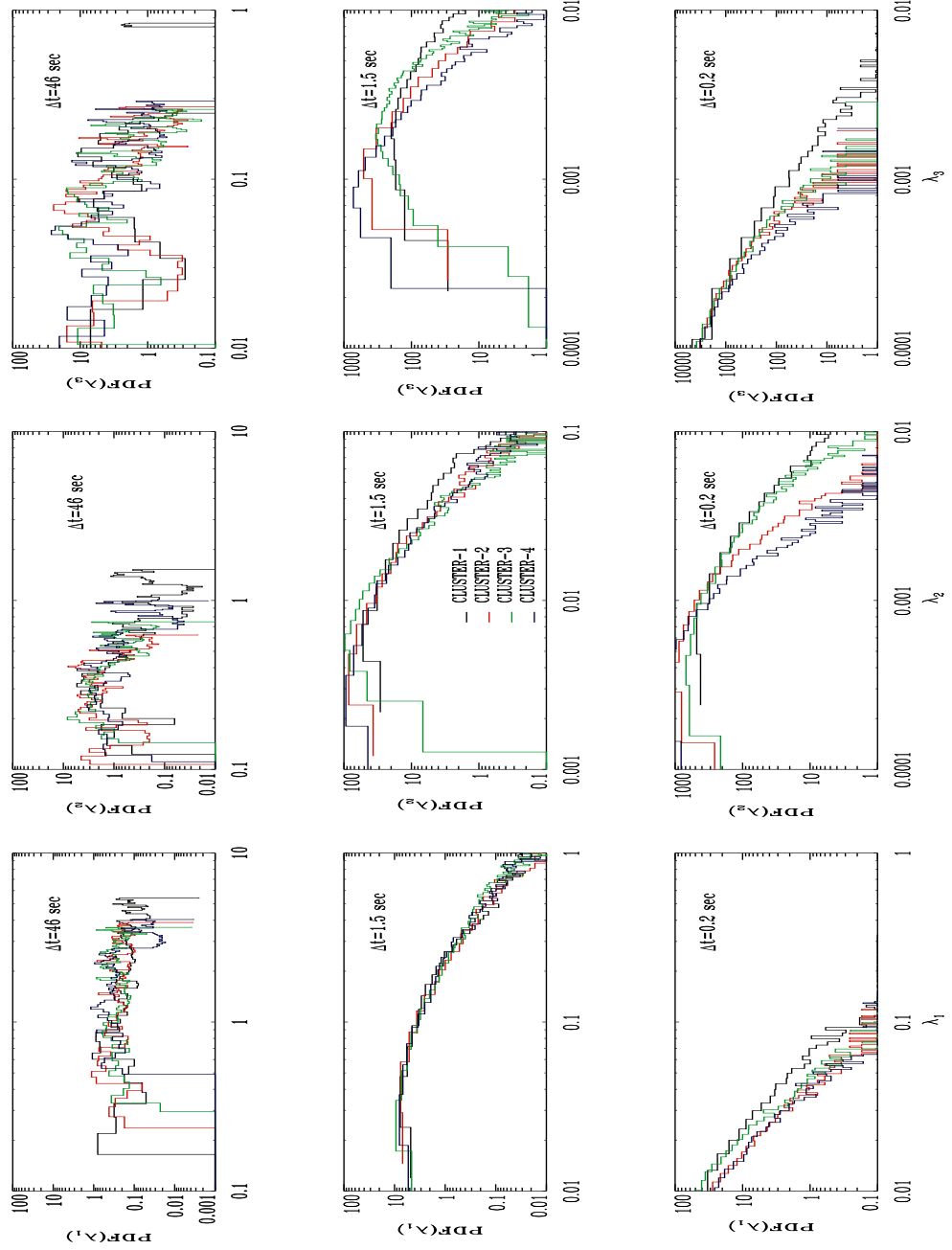
Figure 4.6: Probability density functions of the eigenvalues along the maximum (on the left), the medium (in the middle) and the minimum (on the right) variance directions at three scales in the SW. Different colors refer to the four spacecraft, Cluster-1 (black line), Cluster-2 (red line), Cluster-3 (green line), Cluster-4 (blue line). A change in the shape of the distribution is clear when crossing the ion-cyclotron frequency.
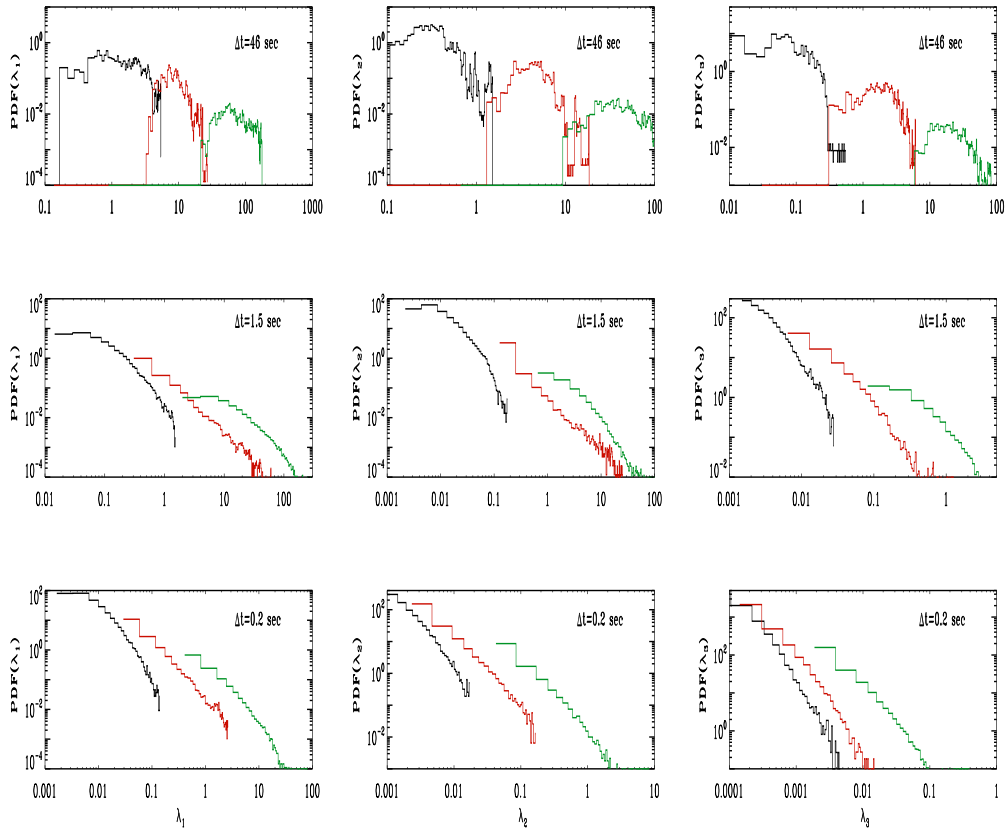
Figure 4.7: Probability density functions of the eigenvalue along the maximum (on the left), the medium (in the middle), and the minimum (on the right) variance directions, at three scales (reported in the panels) in the SW (black curve), in the FS (red curve) and in the MS (green curve).
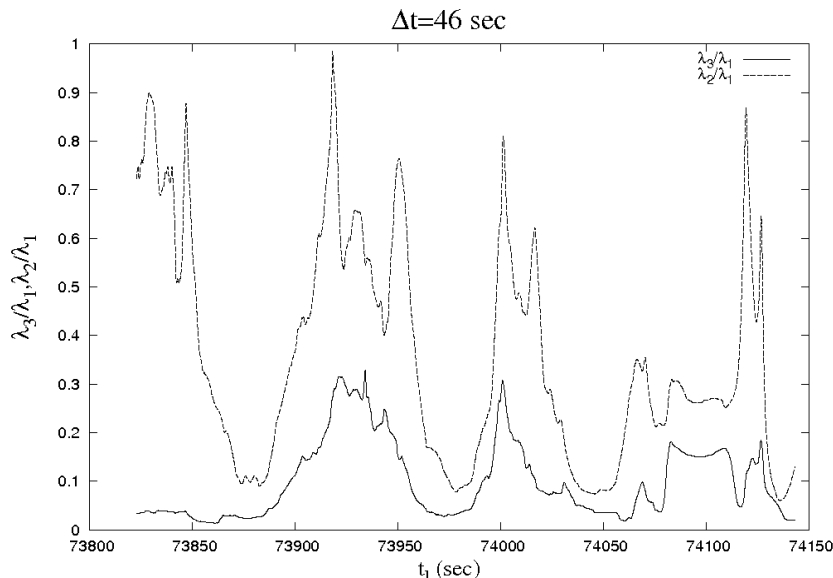
Figure 4.8: Time behavior of ratios $\lambda_3/\lambda1$ (solid line) and λ_2/λ_1 (dashed line) at scale $\Delta t = 46$sec in the SW. Only Cluster-1 data are used.

at three different scales in the three regions, are plotted in Fig. 4.9. These PDFs give information about the change in the degree of anisotropy with the scale. Two main features can be noticed: first of all large-scale values of the ratios are different for the SW with respect to both the MS and the FS. In particular, values of both $\lambda_3/\lambda_1 \leq 0.1$ and $\lambda_2/\lambda_1 \leq 0.1$ are dominant at large-scales for the SW data. On the contrary, the FS and the MS seem to be more isotropic, since values for these cases are confined to $\lambda_2/\lambda_1 \geq 0.1$. Thus, turbulence in the SW is anisotropic already at large-scales [4]. The weak anisotropy found at large-scales for both the MS and the FS, could be due to some mechanisms of energy injection at these scales, owing to the close presence of the bow shock, which yields a partial isotropization of turbulence [133]. Values of $\lambda_2/\lambda_1 \leq 0.1$ have a great probability of occurrence in all the three regions below the ion-cyclotron scale, therefore, fluctuations are statistically confined along the maximum variance direction. This suggests that anisotropy evolves towards a quasi-1D situation and, because of distributions are nearly overlapped, is similar in all the three regions in these frequency ranges.
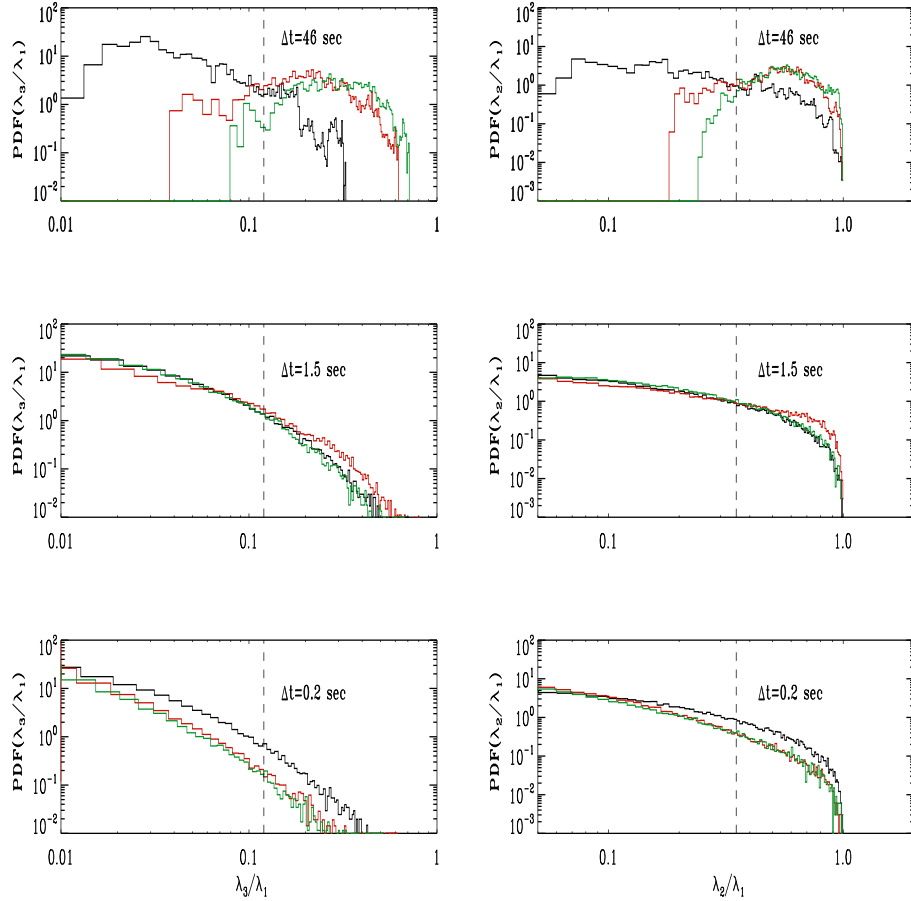
Figure 4.9: Probability density functions of the ratios λ_3/λ_1 (on the left) and λ_2/λ_1 (on the right) at three scales (reported in the panels) in the SW (black line), in the FS (red line) and in the MS (green line). Vertical dashed lines indicate the typical values of the ratios reported in previous works.

4.4 Parameterization of scale-dependence

The scale-dependence effect described above, visible through the scaling evolution of PDFs of eigenvalues, can be quantitatively characterized through the analysis of statistical properties of the eigenvalues. Indeed, by computing the surviving functions of eigenvalues λ_i, namely

$$P(\Lambda_i) = \int_{\Lambda_i}^{\infty} p(\lambda_i)d\lambda_i, \tag{4.4}$$

which represents the number of eigenvalues $\lambda_i \geq \Lambda_i$ normalized to the total number of events within each dataset, a scale-dependence, if any, can be easily detected in changes of the distribution shape. Values of $P(\Lambda_i)$ vs. $\Lambda_i/\langle\Lambda_i^2\rangle^{1/2}$ are reported in Fig. 4.10. It is clear that the shape of such curves changes considerably with the scale, mainly for high values of Λ_i.

The description of the scale-dependence of the surviving functions can be done through a single function, which depends on two free parameters, whose scaling evolution will eventually characterize scale-dependence effects. Let us conjecture that, when Λ are changed by an amount $d\Lambda$, the surviving function varies according to a power law with a given exponent k, namely

$$\frac{dP(\Lambda)}{d\Lambda} = -\left[\frac{P(\Lambda)}{\ell}\right]^k,$$

where ℓ is a free parameter. This expression, once integrated, allows to immediately recover the heuristic probability distribution

$$P(\Lambda) = \left[1 - (1-k)\left(\frac{\Lambda}{\ell}\right)\right]^{1/(1-k)}. \tag{4.5}$$

This expression is able to fit the surviving functions of different phenomena in different regimes [134]. The parameter k is directly related to the functional form of the curve. Indeed, in the limit $k = 1$, the distribution has the exponential shape $P(\Lambda) = \exp(-\Lambda/\ell)$, meaning that the stochastic process, underlying the generation of intense values for the eigenvalues of the variance matrix, is without memory [135]. The value $k = 2$ gives rise to a hyperbolic decrease $P(\Lambda) = 1/[1+(\Lambda/\ell)]$. For intermediate values of k, that is $1 < k < 2$, the curve decays asymptotically as a power law, suggesting the presence of memory effects in the process. A fit of Eq. (4.5) on the data allows to recover the scaling behavior of both $k(\Delta t_n)$ and $\ell(\Delta t_n)$.
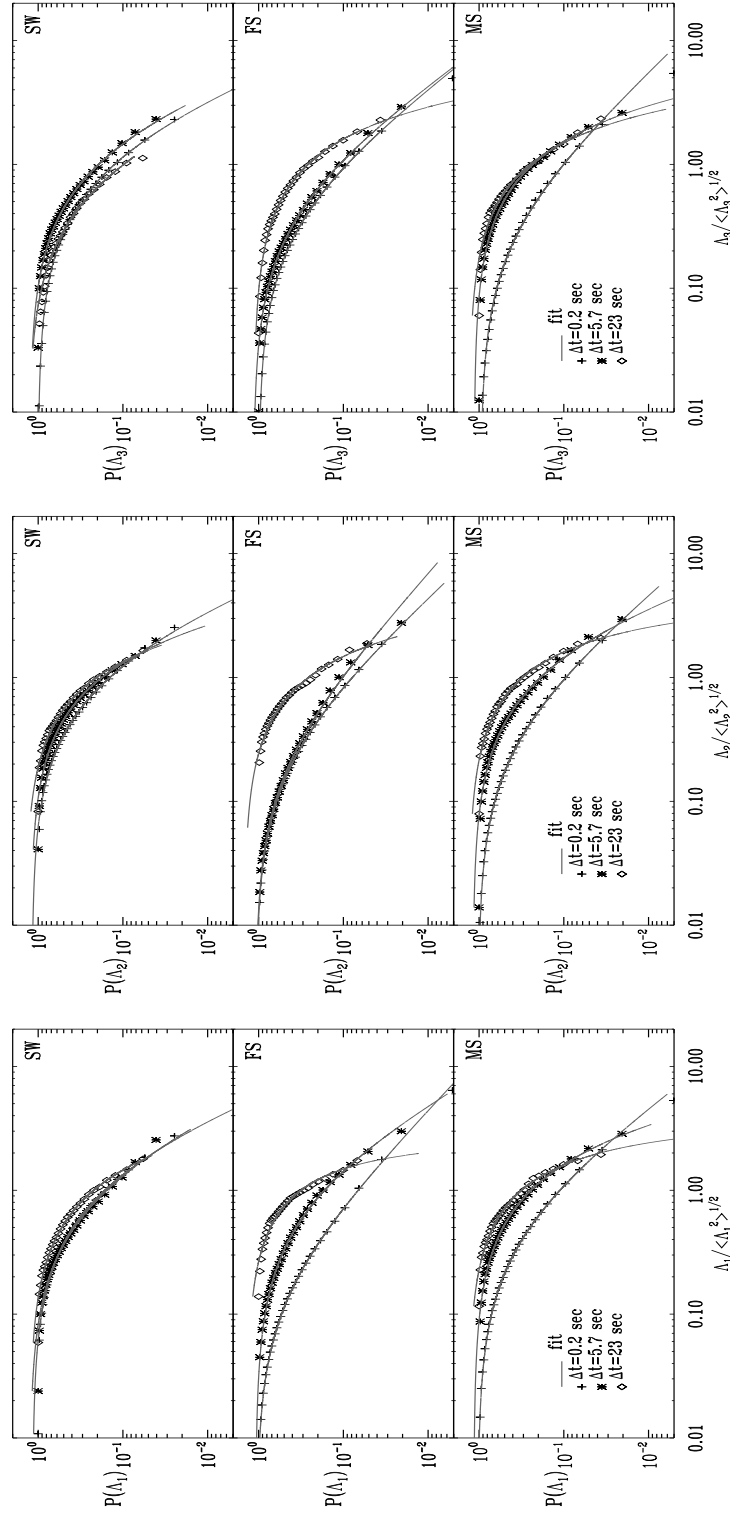
Figure 4.10: Cumulative distribution $P(\Lambda_i)$ as a function of $\Lambda_i/\langle\Lambda_i^2\rangle^{1/2}$ for the SW (upper panel), the FS (middle panel) and the MS (lower panel), at three different scales, namely $\Delta t = 0.2$ sec. (crosses), $\Delta t = 5.7$ sec. (stars), and $\Delta t = 23$ sec. (diamonds). Solid lines represent the best fits.

In Fig.s 4.11 and 4.12 the scaling behaviors of parameters $k(\Delta t_n)$ and $\ell(\Delta t_n)$ respectively are displayed. The first result is that the parameter k changes with scales, describing the shape changes in the surviving functions. In particular, the parameter increases from values $k < 1$ (indicating decorrelations at large scales) to $k > 1$ (indicating correlations at small scales). Indeed, if for $k = 1$ the distribution in Eq. (4.5) becomes a simple exponential, for values $k < 1$ the tails of the distribution decay faster than an exponential, indicating the absence of correlations in the stochastic process. The critical value $k = 1$ is found around the ion-cyclotron scale. The values of the parameter, namely the degree of correlation of the process, and its scaling behavior depend on the case at hand. In particular, in the SW and in the FS k is roughly constant after the rapid increase at the ion-cyclotron scale, and is higher in the FS than in the SW, indicating a higher level of correlations among magnetic fluctuations. In the MS, the parameter increases regularly going toward small scales, and values comparable to those in the FS case are reached at the smallest scales. The scale-dependence effect at the ion-cyclotron frequency is less sharp in this case.

Concerning the parameter ℓ, Fig. 4.12 shows that it is roughly constant in all cases, with a very slow decrease going toward small-scales, mainly in the MS. This parameter seems to play no role in the description of the curves.

4.5 The minimum variance direction

A different characterization of anisotropy can be performed by using values of the angle $\theta^{(s)}(\Delta t_n, t_l)$ between the minimum variance direction and the local mean magnetic field computed at different scales Δt_n for the four Cluster satellites. This analysis gives more detailed information about the geometrical properties of the anisotropy. In Fig. 4.13 time evolutions of the angle $\theta^{(s)}(\Delta t_n, t_l)$ in the three regions and at three different scales, by using the Cluster-1 data, are displayed. Mainly at small scales, $\theta^{(s)}(\Delta t_n, t_l)$ is strongly variable, and it can assume all values in the range $[0, \pi/2]$, apparently in a random way. To evidence scale-dependence effects we calculate the probability of occurrence $P_m(\theta^{(s)})$ of the angle $\theta^{(s)}(\Delta t_n, t_l)$ within the m-th bin, as already done for the eigenvalues of the variance matrix. Even in this case no characteristic trends for each satellite are observed, so we use the four samples to define statistical average values $\bar{\theta}(\Delta t_n)$, weighted with discrete PDFs, at each scale Δt_n. In order to have an estimate of the statistical
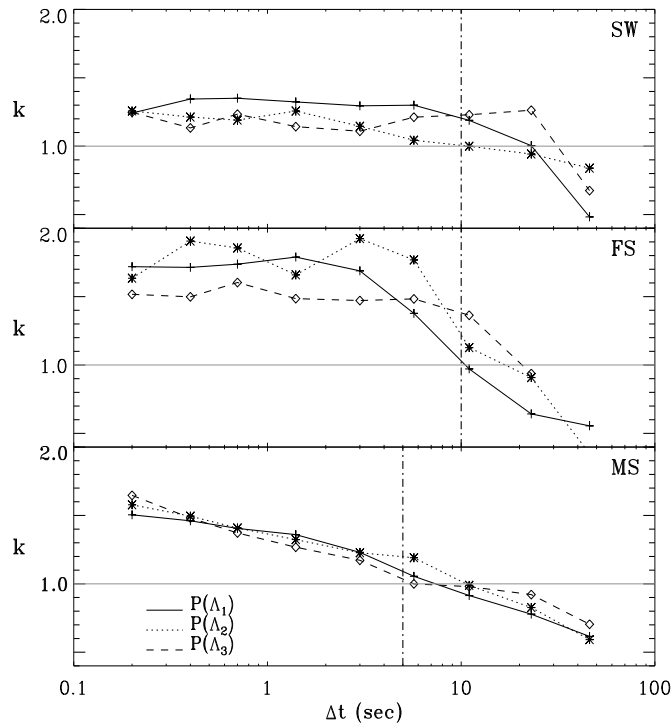
Figure 4.11: Parameter k vs scale Δt for the SW (upper panel), the FS (middle panel) and the MS (lower panel), calculated by fitting the surviving functions with the heuristic probability in Eq. (4.5). The three different lines refer to the three surviving functions fitted, i.e., $P(\Lambda_1)$ (solid line), $P(\Lambda_2)$ (dotted line) and $P(\Lambda_3)$ (dashed line). The vertical dotted-dashed line indicates the ion-cyclotron scale, while the horizontal grey line refers to the critical value $k = 1$.
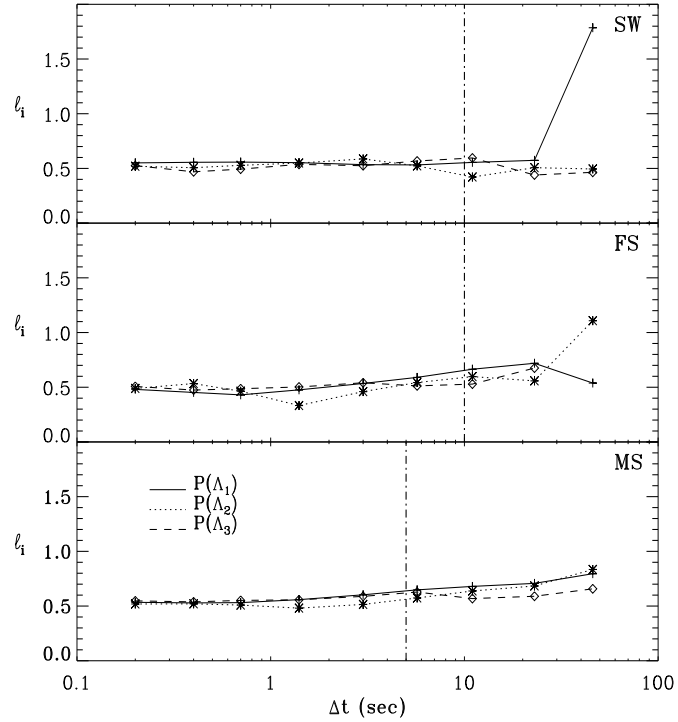
Figure 4.12: Same as Fig. 4.11 but for the parameter ℓ.

dispersion of the values, the standard deviation $\sigma(\theta, \Delta t_n)$ has also been computed. In Fig.s 4.14, 4.15, and 4.16 the $P_m(\theta^{(s)})$ of the angles at different scales Δt_n are displayed. A scale-dependence effect is evident even from this analysis (see also Table 4.1). At scales of minute, PDFs are roughly peaked around small angles, especially in the SW and in the FS, thus indicating that the direction of minimum variance is close to the local background magnetic field B_0, even if a perfect alignment is never recovered. At small-scales the probability of occurrence for small θ decreases and a broadening at values of $\theta > 45°$ is observed. In the MS region (see Fig. 4.16) PDFs at all scales indicate a small probability of occurrence for values of $\theta < 40°$, but below the ion-cyclotron scale there is a tendency for the minimum variance direction

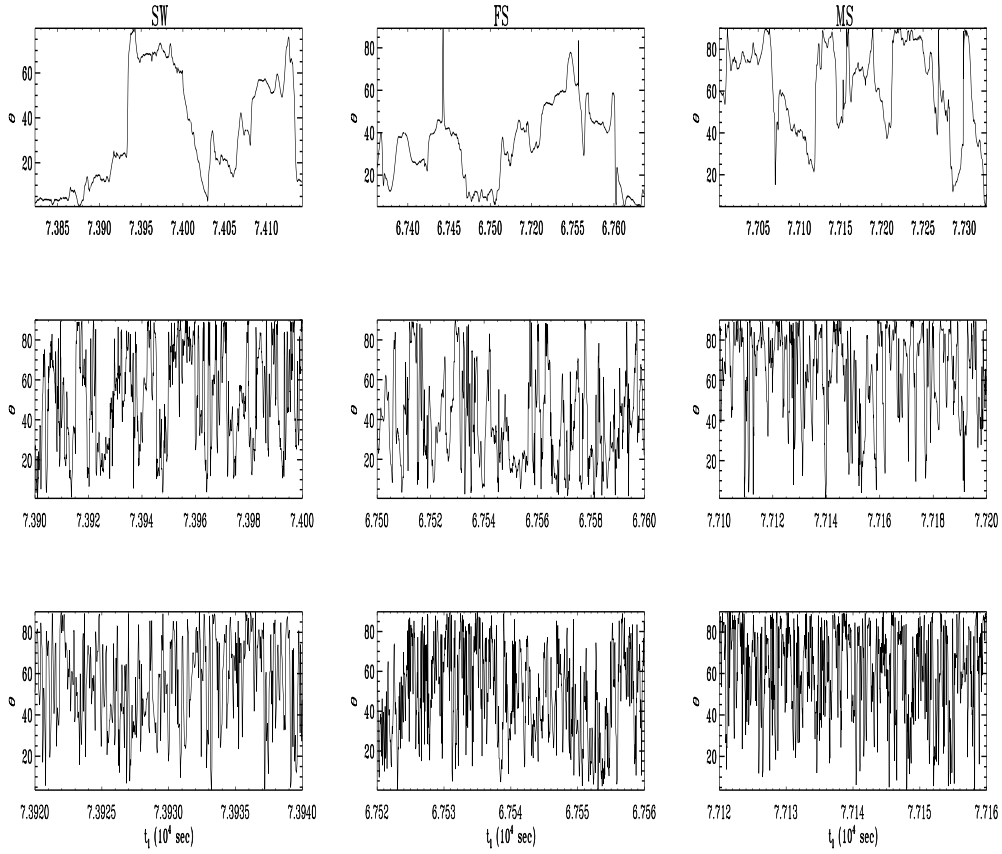Figure 4.13: The angle between the direction of minimum variance and the direction of the mean magnetic field as a function of time at three different scale in the pure SW (on the left), in the FS (in the middle) and in the MS (on the right). At scale of the order of the minute, the two directions seem to be nearly aligned in the SW and in the FS, while at small-scales the angle can assume several values in the interval $[0, \pi/2]$.
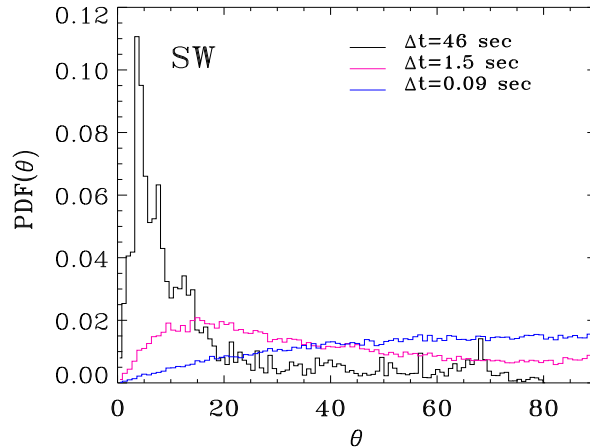
Figure 4.14: PDF of the angle θ at three scales in the SW. The probability of finding a minimum variance direction roughly parallel to the local mean magnetic field increases at large-scales.

to be nearly perpendicular to the mean magnetic field. For summarizing, magnetic fluctuations, localized in the plane perpendicular to the local background magnetic field at scales of minute, become less transverse to B_0 at small-scales, in agreement with the results reported in Ref. [131].

4.6 Remarks

The scaling behavior of anisotropy of magnetic turbulence, as measured by Cluster spacecraft in three different regions of the near Earth space, has been characterized through the analysis of the eigenvalues and eigenvectors of the magnetic field variance matrix calculated at different scales.

Some important results highlighted in previous works by using measurements of various spacecraft in the SW have been confirmed in this study. Indeed, one of the three eigenvalues of the variance matrix is smaller than the other ones in all regions considered. This indicates that a well defined direction, along which magnetic fluctuations have a very low amplitude, exists. Then, magnetic field fluctuations lie in a plane perpendicular to the this direction, named minimum variance direction. In addition, eigenvalues
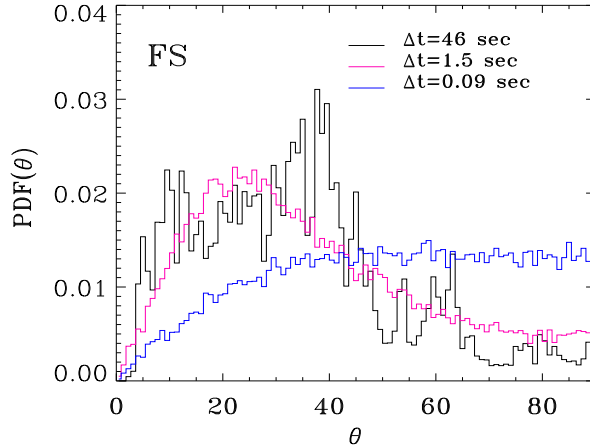
Figure 4.15: The same as Fig. 4.14 but for the FS region.

assume higher values in the MS and in the FS regions than in the SW, indicating that the amplitude of turbulent fluctuations increases near the bow shock.

By looking at the time evolution of the eigenvalues above and below the ion-cyclotron scale, it has been underlined that the behavior passes from being smooth to burst-like. This stochastic process, characterized by the presence of very high amplitude spikes below the ion-cyclotron scale, leads to wide power law PDFs of the eigenvalues in all three regions. As a consequence it is not possible to define a characteristic value (as the average value) for the eigenvalues of the variance matrix at those scales and, therefore, to obtain unambiguous information about the anisotropic power spectrum. A more detailed study of anisotropy, by using statistical properties of both eigenvalues and eigenvectors of the variance matrix, is required. The presence of a scale-dependence can be characterized through a parameterization of the scaling behavior of the PDFs of the eigenvalues. This has been performed here by fitting the surviving probabilities at different scales with a function depending on two free parameters. Results show that the cross-scale is around the ion-cyclotron frequency, that separates scales at which the surviving functions decay faster than an exponential (large-scales), indicating that the process involved is uncorrelated, from those scales in which the
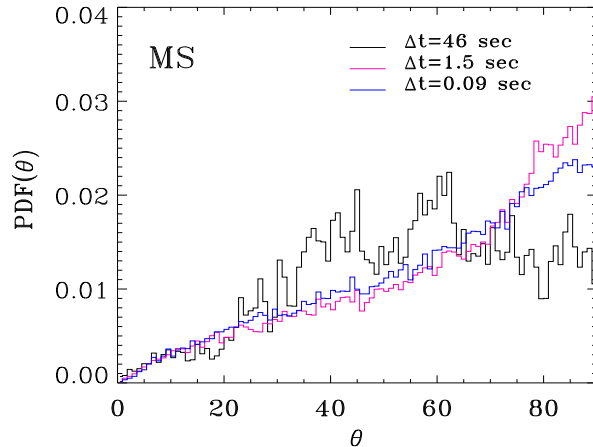
Figure 4.16: The same as Fig. 4.14 but for the MS region. At all scales the minimum variance direction has not negligible probability of being at angles $\theta > 45°$.

tails of the distribution functions decrease slower than an exponential decay (small-scales), that is as a power law, indicating the presence of correlations in the stochastic process.

In all regions examined, the probability of occurrence for small values of the ratios between the minimum and the maximum eigenvalue, and between the intermediate and the maximum eigenvalue, increases going toward small-scales, so that the degree of anisotropy becomes higher below the ion-cyclotron scale. From Fig. 4.9 a strong level of anisotropy can be observed in the SW at scale of minute, while in the FS and in the MS turbulence seems to be more isotropic. The three curves shown become overlapped below the ion-cyclotron scale, increasing the level of anisotropy in all the regions analyzed. This means that at large-scales the mechanisms of energy injection or energy transfer are very different in the three regions; this might be due to the presence of the bow shock which acts as a source of isotropic fluctuations at large-scales. On the other hand, at small scales either energy dissipation processes or energy transfer become roughly similar. In addition, by investigating the temporal behavior of the ratios, it has been found that anisotropy evolves continuously, depending on the type of structures present

Table 4.1: Mean values of the angle θ

Δt (sec)	SW	FS	MS
0.09	54 ± 23	52 ± 23	60 ± 22
0.2	52 ± 23	49 ± 23	61 ± 22
0.4	49 ± 23	45 ± 23	62 ± 22
0.7	44 ± 24	41 ± 22	63 ± 22
1.4	38 ± 24	37 ± 21	62 ± 22
3	31 ± 24	35 ± 21	62 ± 22
6	24 ± 23	35 ± 20	61 ± 22
11	21 ± 21	35 ± 20	61 ± 21
23	19 ± 21	35 ± 20	58 ± 21
46	18 ± 19	34 ± 19	55 ± 21
91	20 ± 16	32 ± 17	59 ± 19
180	11 ± 11	26 ± 8	52 ± 20
360	8 ± 4	25 ± 5	33 ± 17

in the medium at that time. Another step could be the study of the nature of these structure in each temporal interval.

A scale-dependence is evident also when investigating the geometrical properties of turbulence anisotropy through the angle between the minimum variance direction and the local background magnetic field. This quantity varies in the range $[0, \pi/2]$. In the SW and in the FS the minimum variance direction is typically aligned with the background magnetic field at scale of minute. However, below the ion-cyclotron scale the distribution of the angles becomes broader and also values of the angle $\theta > 45°$ have not negligible probability. In the MS a tendency of $\theta(\Delta t)$ to assume a wide range of values is found. Indeed, also at large-scales the distribution is much broader than in the SW. The scaling behavior of $\theta(\Delta t)$ in the SW and in the FS might be due to a change in the nature of magnetic fluctuations, in particular to an increase of compressibility in the high frequency range [125], while the MS region exhibits a turbulence that is much more compressible even at large-scales.

Chapter 5

Conclusions

This thesis addresses some different topics in the framework of the study of complexity in astrophysical systems. We have focused both on the problem of transport and acceleration of particles in the interplanetary medium (via numerical studies and data analysis) and on the characterization of small-scale magnetic turbulence in different regions of the heliospheric environment. Below we summarize the main findings:

1. We numerically investigated the transport properties of an ensemble of non relativistic charged particles interacting with stochastic time-dependent electromagnetic fields. The field is generated by oscillating magnetic clouds. When the oscillating frequency increases, we found that the diffusion in real space goes from a Brownian-like regime to a superdiffusive one. Correspondingly, a change in the diffusion properties in velocity space is also observed, owing to the presence of a stochastic acceleration. The relationship found between scaling exponents of the mean square displacement in real and in velocity spaces is not universal but depends on the time correlations introduced in the model at hand.

2. The numerical model described above has been applied to the problem of particle acceleration in the current sheet of the Earth's magnetotail in order to reproduce a range of particle energy values coming from satellite observations. Besides stochastic time-dependent electromagnetic fields located in the x-y plane, the dawn-dusk constant electric field component along the y direction has been added. Realistic values of this constant electric field component can explain particle energies

of the order of ~ 30 keV, that is the maximum energy allowed by the potential drop, while particles exceeding 100 keV are also observed. Considering the stochastic, Fermi-like, acceleration process, due to the time-dependent fields, as an additional acceleration mechanism, particles can reach energies around 100 keV, in agreement with spacecraft observations. Therefore, we propose that, as well as the steady acceleration coming from the constant dawn-dusk electric field, another source of acceleration of particles in the current sheet can be the stochastic interaction between particles and electromagnetic field fluctuations present in the Earth's magnetosphere.

3. Collimated beams of accelerated particles are frequently observed in space plasmas, as for example in the plasma sheet boundary layer of the Earth's magnetosphere. The Fermi-Ulam model for stochastic acceleration applied to an ensemble of particles results in an energization of the bulk, namely the probability density function at different times can be rescaled to the initial one. We introduced a one-dimensional modified Fermi-Ulam model, where particles are allowed to penetrate the oscillating clouds and are reflected by the magnetic field inside the clouds. The penetration depth is a parameter of the system and, as it increases, a particle energy confinement is observed. Indeed, after a transient time, particle energy remains nearly constant and the usual Fermi acceleration mechanism is broken. Particles start 'resonating' with the clouds, leading to beams formation in the distribution functions. Energetic beams observed in this model have velocities roughly 3–50 times the initial particle thermal speed, in agreement with beams observations in the plasma sheet boundary layer of the terrestrial magnetosphere. Oscillations of accelerating magnetic structures in space plasmas could be driven by instability mechanisms.

4. The analysis of time profiles of particles accelerated at interplanetary shocks and at the solar wind termination shock showed that the propagation of energetic particles in the turbulent environment of the solar wind can be superdiffusive, both for electrons and for ions. By computing particle time profiles with the propagator for Lévy random walks, a power law decay with a characteristic index was obtained instead of an exponential decay, expected in the case of normal diffusion. The analysis of data of particles accelerated at corotating interaction re-

gion shocks, at nearly 6 AU, indicates that time profiles of electrons are power law at some distance from the shock front, therefore, these particles propagate in a superdiffusive way. On the contrary, protons exhibit a normal diffusion. This difference between electrons and protons has been interpreted in terms of their different interaction with magnetic turbulence due to their Larmor radii values. However, by studying the particle time profiles close to the termination shock front, a superdiffusion was found also for ions. This could be due to the low level of turbulence present at this distance from the Sun (~ 100 AU), which leads to a weaker particle pitch-angle scattering. These results indicate that current models of cosmic rays acceleration processes, involving normal diffusion, need to be revisited, as well as models for particles propagation through the heliosphere.

5. The scaling behavior of anisotropy of magnetic turbulence in three different regions of the near Earth space has been investigated by using high-resolution Cluster data. Anisotropy is characterized through the analysis of the eigenvalues and eigenvectors of the magnetic field variance matrix, calculated at different scales. One of the three eigenvalues is found smaller than the other ones in all regions considered. This indicates that turbulent fluctuations are roughly confined in a plane perpendicular to the direction along which magnetic fluctuations exhibit a small variation. A very interesting result is the time intermittency of eigenvalues of the variance matrix at small-scales. This behavior generates a cross-scale effect in magnetic turbulence. Indeed, PDFs of eigenvalues evolve with the scale, that is they become power laws at scales smaller than the ion-cyclotron scale. As a consequence we cannot define a characteristic value for the eigenvalues of the variance matrix at those scales. Therefore, because the variance matrix is related to the magnetic field power spectra, it is not possible to obtain unambiguous information about them above the ion-cyclotron frequency, at least by using single-spacecraft measurements. A scale dependent effect is evident also when investigating the geometrical properties of turbulence anisotropy through the angle between the minimum variance direction and the background magnetic field. In the solar wind and in the foreshock the minimum variance direction is typically aligned with the mean magnetic field above the ion-cyclotron scale. At small-scales PDFs become very broad, increasing the probability of occurrence for

values of the angle greater than 45°. In the magnetosheath the tendency of having a minimum variance direction nearly perpendicular to the mean magnetic field is highly evident at small-scales. This scaling behavior might be due to a change in the nature of magnetic field fluctuations, which become more compressive at high frequencies. Further analysis are required in order to clarify the nature of small-scale magnetic field fluctuations and the processes involved in the formation of the high-frequency range of the magnetic turbulence power spectrum.

Acknowledgments

Bibliography

[1] J. A. Simpson, Ann. Rev. Nucl. Part. Sci. **33**, 330 (1983).

[2] A. M. Hillas, Ann. Rev. Astr. Astrophys. **22**, 425 (1984).

[3] C. Y. Tu and E. Marsch, Space Sci. Rev. **73**, 1 (1995).

[4] R. Bruno and V. Carbone, Living Rev. Solar Phys. **2**, 4 (2005).

[5] U. Frisch, *Turbulence: The Legacy of A. N. Kolmogorov*, Cambridge Univ. Press (1995).

[6] A. N. Kolmogorov, Dokl. Akad. Nauk. SSSR **30**, 301 (1941).

[7] R. J. Leamon, W. H. Matthaeus, C. W. Smith and H. K. Wong, Astrophys. J. Lett. **507**, L181 (1998).

[8] E. Fermi, Phys. Rev. **75**, 1169 (1949).

[9] T. K. Geisser, *Cosmic rays and particle physics*, Cambridge University Press (1990).

[10] R. D. Blandford and J. P. Ostriker, Astrophys. J. Lett. **221**, L29 (1978).

[11] M. A. Lee and L. A. Fisk, Space Sci. Rev. **32**, 205 (1982).

[12] A. R. Bell, Mont. Not. R. Astron. Soc. **182**, 147 (1978).

[13] B. Coppi, G. Laval and R. Pellat, Phys. Rev. Lett. **16**, 1207 (1966).

[14] A. T. Y. Lui et al., Space Sci. Rev. **116**, 497 (2005).

[15] W. H. Matthaeus et al., Space Sci. Rev. **87**, 269 (1999).

BIBLIOGRAPHY

[16] J. M. Dawson et al., Phys. Rev. Lett. **50**, 1455 (1983).

[17] T. Katsouleas and J. M. Dawson, Phys. Rev. Lett. **51**, 392 (1983).

[18] D. Ucer and V. D. Shapiro, Phys. Rev. Lett. **87**, 075001 (2001).

[19] D. del-Castillo-Negrete, B. A. Carreras and V. E. Lynch, Phys. Plasmas **11**, 3854 (2004).

[20] J. R. Jokipii, Astrophys. J. **146**, 480 (1966).

[21] W. H. Matthaeus, G. Quin, J. W. Bieber and G. P. Zank, Astrophys. J. Lett. **590**, L53 (2003).

[22] G. Boffetta, G. Lacorata and A. Vulpiani, Introduction to Chaos and Diffusion, *Chaos in Geophysical Flows*, ISSAOS (2001).

[23] T. H. Solomon, E. R. Weeks and H. L. Swinney, Phys. Rev. Lett. **71**, 3975 (1993).

[24] S. Ratynskaia et al., Phys. Rev. Lett. **96**, 105010 (2006).

[25] B. A. Carreras, V. E. Lynch and G. M. Zaslavsky, Phys. Plasmas **8**, 5096 (2001).

[26] G. Qin, W. H. Matthaeus and J. W. Bieber, Geophys. Res. Lett. **29(4)**, 1048 (2002).

[27] G. Zimbardo, P. Pommois and P. Veltri, Astrophys. J. Lett. **639**, L91 (2006).

[28] J. Klafter, A. Blumen and M. F. Shlesinger, Phys. Rev. A **35**, 3081 (1987).

[29] G. M. Zaslavsky et al., Soviet Phys.–JETP, **68**, 995 (1989).

[30] J. Klafter, M. F. Shlesinger and G. Zumofen, Phys. Today **49**, 33 (1996).

[31] I. M. Sokolov, J. Klafter and A. Blumen, Phys. Today **55**, 48 (2002).

[32] G. M. Zaslavsky, Phys. Rep., **371**, 461 (2002).

[33] F. Bouchet, F. Cecconi and A. Vulpiani, Phys. Rev. Lett. **92**, 040601 (2004).

[34] L. Vlahos, H. Isliker and F. Lepreti, Astrophys. J. **608**, 540 (2004).

[35] O. Stawicki, Astrophys. J. **631**, 597 (2005).

[36] S. Perri, F. Lepreti, V. Carbone and A. Vulpiani, Europhys. Lett. **78**, 40003 (2007).

[37] D. Alonso, R. Artuso, G. Casati and I. Guarneri, Phys. Rev. Lett. **82**, 1859 (1999).

[38] S. Perri, F. Lepreti, V. Carbone and A. Vulpiani, Comm. Nonlin. Sc. Numer. Simul., doi:10.1016/j.cnsns.2008.06.023,(2008).

[39] R. J. Decoster and L. A. Frank, J. Geophys. Res. **84**, 5099 (1979).

[40] K. Takahashi and E. W. Jr Hones, J. Geophys. Res. **93**, 8558 (1988).

[41] M. Nakamura, G. Paschmann, W. Baumjohann and N. Sckopke, J. Geophys. Res. **96**, 5631 (1991).

[42] L. M. Zelenyi, E. E. Grigorenko, J.-A. Sauvaud and R. Maggiolo, Geophys. Res. Lett. **33**, L06105 (2006).

[43] E. E. Grigorenko, J.-A. Sauvaud and L. M. Zelenyi, J. Geophys. Res. **112**, A05218 (2007).

[44] J. Buchner and L. M. Zelenyi, Geophys. Res. Lett. **17**, 127 (1990).

[45] M. Ashour-Abdalla, J. P. Berchem, J. Buchner and L. M. Zelenyi, J. Geophys. Res. **98**, 5651 (1993).

[46] A. Keiling et al., Geophys. Res. Lett. **31**, L12804 (2004).

[47] E. E. Grigorenko, M. Hirai, M. Hoshino, T. Mukai and L. M. Zelenyi, J. Geophys. Res. *submitted* (2008).

[48] J. F. Drake, M. Swisdak, H. Che and M. A. Shay, Nature **443**, 553 (2006).

[49] O. Verkhoglyadova et al., Ann. Geophys. **17**, 1145 (1999).

[50] Z. Voros et al., Nonlin. Proc. Geophys., **14**, 535 (2007).

BIBLIOGRAPHY

[51] O. Alexandrova, Nonlin. Processes Geophys. **15**, 95 (2008).

[52] M. Hoshino, A. Nishida, T. Yamamoto and S. Kokubun, Geophys. Res. Lett., **21**, 2935 (1994).

[53] A. Brahic, Astron. Astrophys. **12**, 89 (1971).

[54] S.V. Vladimirov, S.A. Maiorov, M.Y. Yu and L. Stenflo, Phys. Rev. E **63**, 067401 (2001).

[55] A. Veltri and V. Carbone, Phys. Rev. Lett. **92**, 143901 (2004).

[56] R. De Marco, V. Carbone and P. Veltri, Phys. Rev. Lett. **96**, 125003 (2006).

[57] S. Ulam, in *Proceedings of the Fourth Berkley Symposium on Mathematics, Statistics, and Probability* (California University Press, Berkley, 1961), Vol. 3, p. 315.

[58] M.A. Lieberman and A.J. Lichtenberg, Phys. Rev. A **5**, 1852 (1972), and references therein.

[59] A.J. Lichtenberg and M.A. Lieberman, *Regular and Chaotic Dynamics*, Applied Mathematical Sciences, Vol. 38 (Springer–Verlag, New York, 1992).

[60] E.D. Leonel, P.V.E. McClintock and J. Kamphorst Leal da Silva, Phys. Rev. Lett. **93**, 014101 (2004).

[61] A.K. Karlis, P.K. Papachristou, F.K. Diakonos, V. Constantoudis and P. Schmelcher3, Phys. Rev. Lett. **97**, 194102 (2006).

[62] J.K. L. da Silva, D.G. Ladeira, E.D. Leonel, P.V.E. McClintock, and S.O. Kamphorst, Braz. J. Phys. **36**, 700 (2006).

[63] E.D. Leonel, J. K. L. da Silva and S. O. Kamphorst, Phys. A **331**, 435 (2004).

[64] D. G. Ladeira and J. K. L. da Silva, Phys. Rev. E **73**, 026201 (2006).

[65] M. Onofri, H. Isliker and L. Vlahos, Phys. Rev. Lett. **96**, 151102 (2006).

[66] E. Priest, Solar Flare Magnetohydrodynamics, Gordon and Breach, New York (1981).

[67] J.A. Miller et al., J. Geophys. Res. **102**, 14631 (1997).

[68] W. Kob and R. Schilling, J. Phys. A:Math. Gen. **22**, L633 (1989).

[69] S. Perri and V. Carbone, Geophys. Res. Lett., *submitted* (2008).

[70] S. Chandrasekhar, *Hydrodynamic and Hydromagnetic Stability*, Dover Pub., INC. New York (1970).

[71] E. Hildner, Solar Phys. **35**, 123 (1974).

[72] M. Dobrowolny, P. Veltri and A. Mangeney, J. Plasma Phys. **29**, 393 (1983).

[73] V. Carbone, P. Veltri and A. Mangeney, Phys. Fluids **2**, 1487 (1990).

[74] M. V. Medvedev and A. L. Melott, Astrophys. J. **664**, 879 (2007).

[75] J. Giacalone and J. R. Jokipii, Astrophys. J. **520**, 204 (1999).

[76] P. Pommois, G. Zimbardo and P. Veltri, Phys. Plasmas **14**, 012311 (2007).

[77] G. P. Zank, W. K. M. Rice and C. C. Wu, J. Geophys. Res. **105**, 25079 (2000).

[78] M. A. Lee, Astrophys. J. Suppl. Ser. **158**, 38 (2005).

[79] A. M. Hillas, J. Phys. G: Nucl. Part. Phys. **31**, R95 (2005).

[80] M. A. Lee, G. Skadron and L. A. Fisk, Geophys. Res. Lett. **8**, 401 (1981).

[81] L. A. Fisk and M. A. Lee, Astrophys. J. **237**, 620 (1980).

[82] M. E. Pesses, J. R. Jokipii and D. Eichler, Astrophys. J. Lett. **246**, L85 (1981).

[83] E. N. Parker, Planet. and Space Sci. **13**, 9 (1965).

[84] M. Neugebauer, J. Giacalone, E. Chollet and D. Lario, J. Geophys. Res. **111**, A12107 (2006).

BIBLIOGRAPHY

[85] D. Lario et al., in *Connecting Sun and Heliosphere:Proceedings of Solar Wind 11/SOHO 16*, edited by B. Fleck and T. H. Zurbuchen, Eur. Space Agency Spec. Publ., ESA SP-592,81 (2005).

[86] M. B. Kallenrode and G. Wibberenz, J. Geophys. Res. **102**, 22 (1997).

[87] W. Dröge, Astrophys. J. **589**, 1027 (2003).

[88] R. P. Lin, Adv. Space Res. **35**, 1857 (2005).

[89] J. W. Bieber et al., Astrophys. J. **420**, 294 (1994).

[90] D. V. Reames, Space Sci. rev **90**, 413 (1999).

[91] T. Geisel, J. Nierwetberg and A. Zacherl, Phys. Rev. Lett. **54**, 616 (1985).

[92] M. F. Shlesinger, B. West and J. Klafter, Phys. Rev. Lett. **58**, 1100 (1987).

[93] R. Metzler and J. Klafter, Phys. Rep. **339**, 1 (2000).

[94] S. Perri and G. Zimbardo, Astrophys. J. Lett. **671**, L177 (2007).

[95] S. Perri and G. Zimbardo, J. Geophys. Res. **113**, A03107 (2008).

[96] L. D. Landau and E. M. Lifshitz, *Fluid Mechanics*, Course of theoretical physics, Oxford: Pergamon Press (1959).

[97] G. M. Webb et al., Astrophys. J. **651**, 211 (2006).

[98] M. A. Lee, J. Geophys. Res. **88**, 6109 (1983).

[99] S. Perri and G. Zimbardo, in *Chaos, Complexity and Transport: theory and apllications*,edited by C. Chandre, X. Leoncini and G. Zaslavsky, World Scientific, 309 (2008).

[100] G. Zumofen and J. Klafter, Phys. Rev. E **47**, 851 (1993).

[101] R. Metzler and J. Klafter, J. Phys. A Math. Gen. **37**, R161 (2004).

[102] S. Perri and G. Zimbardo, Astrophys. Space Sci. Trans. **4**, 27 (2008).

[103] A. Balogh et al., Space Sci. Rev. **72**, 171 (1995).

[104] M. I. Desai et al., *Proc. Int. Conf. Cosmic Rays 25th* **1**, 365 (1997).

[105] W. H. Matthaeus and M. L. Goldstein,Phys. Rev. lett. **57**, 495 (1986).

[106] T. S. Horbury, A. Balogh, R. J. Forsyth and E. J. Smith, Astron. Astrophys. **316**, 333 (1996).

[107] D. Ruffolo, Astrophys. J. **442**, 861 (1995).

[108] P. R. Gazis, J. Geophys. Res. **105**, 19 (2000).

[109] R. B. Decker et al., Nature **454**, 67 (2008).

[110] M. Zhang, Adv. Space Res. **35**, 562 (2005).

[111] E. C. Stone et al., Nature **454**, 71 (2008).

[112] H. Washimi et al., Astrophys. J. Lett. **670**, L139 (2007).

[113] P. Duffy. J. G. Kirk, Y. A. Gallant and R. O. Dendy, Astron. Astrophys. **302**, L21 (1995).

[114] A. A. Lagutin and V. V. Uchaikin, Nucl. Instrum. Methods Phys. Res. Sect. B **201**, 212 (2002).

[115] J. Lintunen and R. Vainio, Astron. Astrophys. **420**, 343 (2004).

[116] R. B. Decker et al., Science **309**, 2020 (2005).

[117] E. C. Stone et al., Science **309**, 2017 (2005).

[118] J. W. Belcher and L. Davis Jr, J. Geophys. Res. **76**, 3534 (1971).

[119] C. W. Smith, W. H. Matthaeus and N. F. Ness, *Proc. 21st Int. Cosmic Ray Conf.* **5**, 280 (1990).

[120] M. L. Goldstein, D. A. Roberts and C. A. Fitch, J. Geophys. Res. **99**, 11,519 (1994).

[121] R. J. Leamon, C. W. Smith, N. F. Ness, W. H. Matthaeus and H. K. Wong, J. Geophys. Res. **103**, 4775 (1998).

[122] R. J. Leamon, C. W. Smith, N. F. Ness and H. K. Wong, J. Geophys. Res. **104**, 22,331 (1999).

BIBLIOGRAPHY

[123] D. Biskamp, E. Schwarz and J. F. Drake, Phys. Rev. Lett. **76**, 1264 (1996).

[124] O. Stawicki, S. P. Gary and H. Li, J. Geophys. Res. **106**, 8273 (2001).

[125] O. Alexandrova, V. Carbone, P. Veltri and L. Sorriso-Valvo, Astrophys. J. **674**, 1153 (2008).

[126] B. U. Ö Sonnerup and L. J. Cahill, J. Geophys. Res. **72**, 171 (1967).

[127] S. C. Chang and A. Nishida, Astrophys. Space Sci. **23**, 301 (1973).

[128] J. W. Belcher and C. V. Solodyna, J. Geophys. Res. **80**, 181 (1975).

[129] B. Bavassano, M. Dobrowolny, G. Fanfoni, F. Mariani and N. F. Ness, Sol. Phys. **78**, 373 (1982).

[130] V. Carbone, F. Malara and P. Veltri, J. Geophys. res. **100**, 1763 (1995).

[131] K. Hamilton, C. W. Smith, B. J. Vasquez and R. J. Leamon, J. Geophys. Res. **113**, A01106 (2008).

[132] A. Balogh et al., Space Sci. Rev. **79**, 65 (1997).

[133] E. Yordanova, A. Vaivads, M. André, S. C. Buchert and Z. Voros, Phys. Rev. Lett. **100**, 205003 (2008).

[134] S. Abe and N. Suzuki, Phys. A **350**, 588 (2005).

[135] W. Feller, *An introduction to probability theory and its application*, **1** Wiley, New York, 3rd edition.